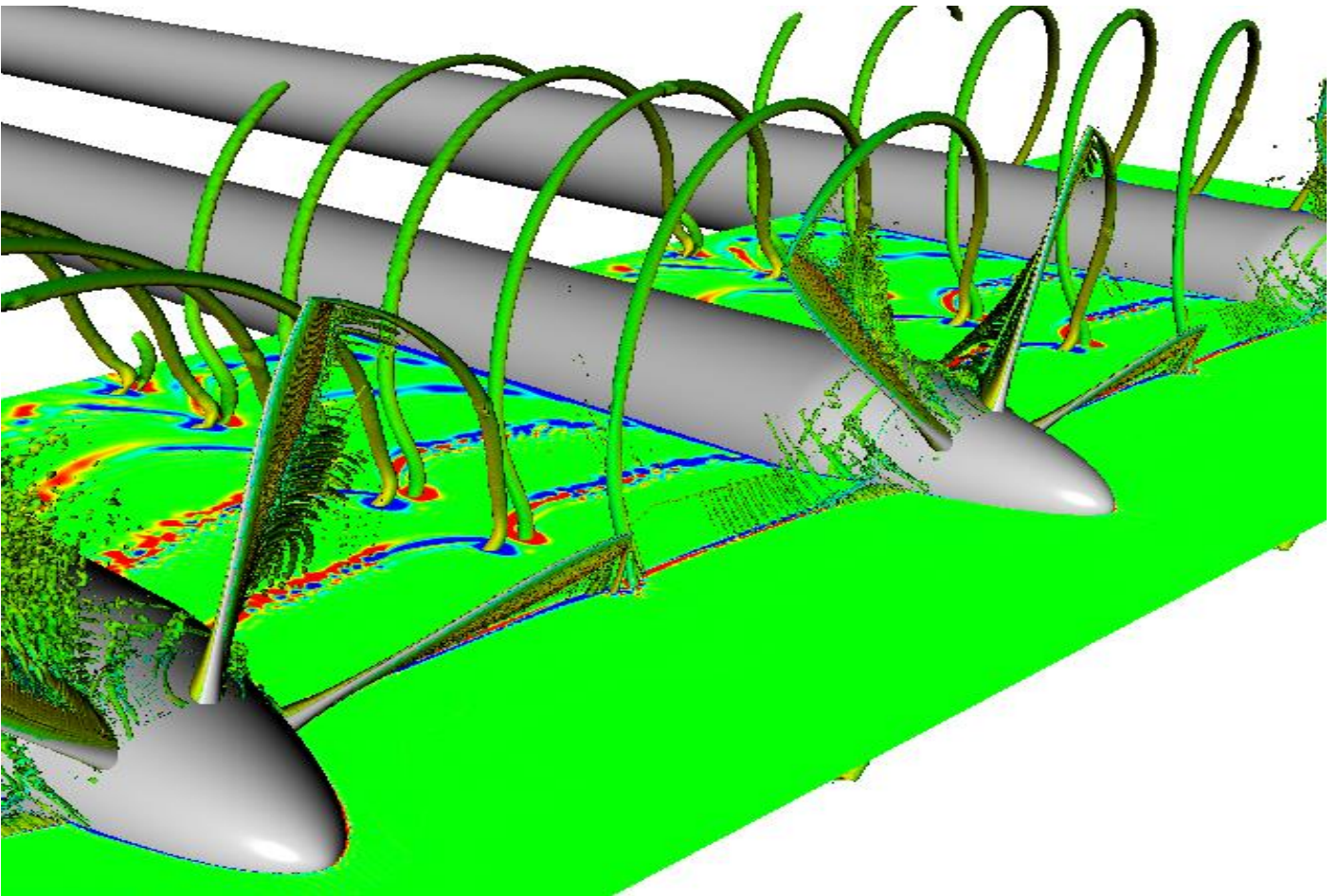


P. Alexandros Koutsoukos

Aerodynamic and Aeroacoustic Interaction Effects of a Distributed-Propeller Configuration in Forward Flight

A Computational Investigation



Aerodynamic and Aeroacoustic Interaction Effects of a Distributed-Propeller Configuration in Forward Flight

A Computational Investigation

By

Panagiotis Alexandros Koutsoukos

in partial fulfilment of the requirements for the degree of

Master of Science
in Aerospace Engineering

at the Delft University of Technology,
to be defended publicly on Thursday January 20, 2022 at 02:00 PM.

Thesis committee: Dr. D. Ragni, TU Delft, Chair
 Dr. F. Avallone, TU Delft, Supervisor
 R. de Vries, TU Delft, Supervisor
 Dr. T. Sinnige, TU Delft, Examiner

An electronic version of this thesis is available at <http://repository.tudelft.nl/>.

Summary.....	vii
List of Abbreviations.....	ix
List of Symbols.....	x
Table of Figures.....	xii
List of Tables.....	xvi
1 Introduction.....	2
1.1 Research objective.....	3
1.2 Research questions.....	3
2 Theoretical Background and Literature Review.....	5
2.1 Propeller aerodynamics.....	5
2.1.1 Actuator disk theory.....	5
2.1.2 Blade element momentum analysis.....	6
2.1.3 Slipstream tube model.....	7
2.1.4 Propeller's performance coefficients.....	8
2.2 Distributed-propeller aerodynamics.....	9
2.2.1 Aerodynamic performance.....	10
2.2.2 Flow physics.....	12
2.3 Propeller's aeroacoustics.....	14
2.3.1 Fundamentals of sound.....	15
2.3.2 Propeller noise sources.....	16
2.3.3 Aeroacoustic analogies.....	17
2.3.4 Aeroacoustic signature in multi-rotor systems.....	18
3 Methodology.....	22
3.1 Flow solver.....	22
3.1.1 Lattice Boltzmann method.....	22
3.1.2 Computational aeroacoustics.....	27
3.2 Computational setup.....	28
3.2.1 Propeller geometry.....	28
3.2.2 Isolated-propeller case setup.....	29
3.2.3 Distributed-propeller case setup.....	31
3.3 Acoustic measurements.....	33
3.4 Flow Conditions.....	34
3.4.1 Boundary conditions.....	34
3.5 Time convergence-Measurements sampling.....	35
3.6 Experimental setup.....	36
4 Resolution and Validation Study.....	38
4.1 Isolated-propeller case.....	38
4.1.1 Effect of blades azimuthal position with respect to the Cartesian axis.....	44
4.2 Aeroacoustic resolution study.....	48
4.2.1 Comparison between solid and permeable surfaces formulation.....	50
4.3 Distributed-propeller model: Comparison with experimental data.....	52
5 Aerodynamic Analysis.....	55
5.1 Aerodynamic performance of the baseline configuration.....	55
5.1.1 Mean flow field analysis.....	56
5.1.2 Vortex field.....	63
5.1.3 Unsteady loading.....	68
5.2 Effects of relative phase angle.....	70
5.2.1 Flow field comparison with the baseline model.....	71
5.2.2 Effect on unsteady loading.....	75

6	Aeroacoustic Analysis.....	77
6.1	Noise emission of the baseline model.....	77
6.1.1	Near-field acoustics evolution.....	79
6.1.2	Spectral analysis.....	81
6.2	Relative phase angle effect.....	83
6.2.1	Noise directivity comparison.....	83
6.2.2	Near-field acoustics alteration.....	85
6.2.3	Spectral analysis comparison.....	85
7	Conclusions and Recommendations.....	88
7.1	Recommendation.....	91
	Bibliography.....	92

Summary

The Advisory Council of Aviation Research has set the future goals of sustainable development in aviation by reducing pollutant emissions of CO₂ by 75% and 90% in NO_x emissions per passenger kilometre and noise emission by 65% of the perceived noise level compared with the measurements in 2000. This demand has led to the development of new aircraft concepts with alternative propulsive systems. The development of the all-electric and hybrid-electric aircraft concepts has regenerated the interest in distributed propulsion systems with propellers. Distributed-propeller systems are propulsive configurations with multiple propellers located along the wing or/and aircraft's airframe. Among the benefits of these systems is their electrical connectivity with the power generating sources or energy sources, like batteries, that make them attractive for vehicles performing electrical vertical take-off and landing (eVTOL) for urban air mobility.

Previous studies' investigation of multi-rotor systems has been primarily focused on the aerodynamic performance changes in hover conditions. The thrust decrease of these propellers during their operation at a close distance is accompanied by oscillations associated with the flow structures interactions. This results in a noise emission increase attributed to the thrust fluctuations. The investigation, therefore, of the distributed-propeller system in forward flight will contribute to the in-depth analysis of the performance of these systems and illustrate the root of potential changes, assessing the changes in thrust as well as the unsteady loading of the blades. Also, the present analysis will study the mechanisms that lead to noise emission increase and the potential benefits of the relative phase angle variation between adjacent propellers. The effect of the relative phase angle has shown a positive impact on noise emission of multiple-propeller systems without considering the interference between adjacent propellers. Thus, the aim of the present computational study is to investigate the aerodynamic interference and aeroacoustic signature of a distributed-propeller configuration in forward flight, including the effects of the relative phase angle.

The comparison of the distributed-propeller model with the isolated propeller case showed minor differences in the time-averaged performance. The mean thrust coefficient increases slightly by 0.0004, whereas the time evolution plot reveals the thrust oscillation with amplitude equal to 5.3% of the mean value. The trailing vortex systems of adjacent propellers induce velocity components that alter the propellers' flow field upstream and downstream. These induced velocities result in axial velocity increase upstream of the propeller and in non-zero values of the tangential velocity, resulting in thrust oscillations. This results in a change of thrust as the propeller rotates. During the motion of a blade, its thrust is reduced when it approaches the adjacent propeller and subsequently increases during its retreat, resulting in an unsteady loading on the blades. The slipstream of the systems also presents differences from the respective one of an isolated propeller. The symmetric and circular shape of the wake flow behind the isolated propeller is broken and turned into a deformed wake flow behind the distributed-propeller system, as a result of the interference of the tip vortices. The tip vortices emitted by adjacent blades stay close with each other during their downstream motion, with their interaction results in change of trajectory, shape deformation and fast dissipation.

The noise emission of the distributed-propeller system shows a noise level increase in front of the propellers while along the propeller plane, this increase is smaller. The comparison of the middle propeller of the system with the isolated one reveals an increase of 13.5 dB along the propellers axis, while the increase along the plane of rotation is 1.8 dB. The increase along the propeller axis is associated with enhanced tonal components at frequencies up to the 5th blade passing frequency. The directivity of the noise emission and the augmentation of tonal components imply that the unsteady loading is the reason for the noise levels increase. The increase of the broadband component (3.2 dB) at oblique angles with respect to the propeller axis is attributed to the interaction of adjacent flow structures.

The variation of the relative phase angle between adjacent propellers results in blades passing from the region between adjacent propellers at different times. This has positively impacted the unsteady loading as it is decreased compared to the case without relative phase angle variation. The oscillatory behaviour of the thrust is reduced as the standard deviation of the thrust coefficient drops from 0.001 to 4.5e-04. On the contrary, the time-averaged performance of the propellers remains unaffected. The reduction of the unsteady loading results in noise emission reduction in the upstream direction by 5 dB, while at oblique angles in the

downstream direction, there is a 1.8 dB increase. This increase is attributed to a different tonal component distribution than in the case without relative phase angle variation. Thus, the impact of the relative phase angle variation could be beneficial on noise emission angles normal to rotor plane due to the reduced unsteady loading.

List of Abbreviations

ACARE	Advisory Council of Aviation Research
BGK	Bhatnagar-Gross-Krook
BPF	Blade passing frequency
CFD	Computational Fluid Dynamics
DP	Distributed-propeller model
DP($\Delta\phi=0^\circ$)	Distributed-propeller model with 0° relative phase angle
eVTOL	electrical vertical take-off and landing
FHP	Frisch, Hasslacher, and Pomeau model
FWH	Ffowcs-Williams and Hawkings
LBM	Lattice Boltzmann method
LES	Large-eddy simulation
LTT	Low-turbulence tunnel
NS-CFD	Navier Stokes Computational Fluid Dynamics
<i>OSPL</i>	Overall sound pressure level
PGE-WM	Pressure gradient wall model
PSD	Power spectral density
PIV	Particle-image velocimetry
Res	Resolution
<i>SPL</i>	Sound pressure level
UAVs	Unmanned Aerial Vehicles
VLES	Very Large-eddy simulation
VR	Variable resolutions

List of Symbols

A_p	Propeller disc [m ²]	T_c	Thrust coefficient [-]
B	Number of blades[-]	T_{ij}	Lighthill stress tensor
c, c_∞	Speed of sound [m/s]	T_s	Duration of signal [s]
c_i	Discrete velocity of particle in a node [m/s]	U_∞	Free-stream velocity [m/s]
$C_{p,total}$	Total pressure coefficient [-]	U	Incoming velocity in airfoil [m/s]
c_r	Propeller root chord [m]	u^+	Velocity [-]
D	Propeller diameter [m]	u_τ	Friction velocity [m/s]
dD	Drag of an airfoil [N]	U_{axial}, V_a	Axial velocity [m/s]
df	Frequency Band width [Hz]	ν	Kinematic Viscosity [m ² /s]
dL	Lift of an airfoil [N]	$V_{ind,r}$	Induced radial velocity component [m/s]
dp/dt	Time pressure derivative [Pa/s]	$V_{ind,x}$	Induced axial velocity component [m/s]
dQ	Torque of an airfoil [Nm]	$V_{ind,\theta}$	Induced velocity out-of-plane [m/s]
dR	Resulting force of an airfoil [N]	V_∞	Free-stream velocity [m/s]
dT	Thrust of an airfoil [N]	V_t	Tangential velocity [m/s]
f	Frequency [Hz]	V_3	Downstream velocity [m/s]
f^*	Post-collision distribution of particles	w_i	Weighting factor of velocity set of particle distribution
$f(x,t)$	Particle distribution function [-]	y^+	Wall distance [-]
f_i^{eq}	Equilibrium distribution [-]	$[L,W,H]$	Length, Width, Height
H_s	Heaviside function	α	Angle of attack [°]
J	Advance Ratio [-]	β	Azimuthal angles[°]
k	Turbulent kinetic energy [J/kg]	γ	Distributed vorticity [m/s]
k_{mB}	Wavenumber	$\gamma(r)$	Force angle with the normal axis
\dot{m}	Mass flow rate [kg/s]	Γ_{bound}	Bound vorticity [m ² /s]
M_r	Mach number at the direction r	Γ_{root}	Root vortex [m ² /s]
n, N	Rotational velocity [rps]	Γ_{Tip_vortex}	Tip Vorticity [m ² /s]
N_{rot}	Number of propeller's rotation [-]	Γ_x	Axial vorticity component [m ² /s]
p	Pressure [Pa]	Γ_z	Vorticity component along Z-axis [m ² /s]
P	Power [W]	Γ_θ	Tangential vorticity component [m ² /s]
$P(f)$	Power spectral density [Pa ² /Hz]	δ_{ij}	Dirac function
p_{rms}	Pressure root mean square [Pa]	Δt	Time step [s]
p'	Pressure perturbation [Pa]	δT_c	Thrust coefficient distribution difference [-]
Q	Torque [Nm]	Δx	Spatial discretization [m]
Q_c	Torque coefficient [-]	$\Delta\phi$	Relative phase angle [°]
R	Propeller radius [m]	ε	Turbulent dissipation rate [J/kgs]
r	Radial positions of cross section [m]	η	Propeller efficiency [-]
r/R	Non-dimensional radial coordinate [-]	θ	Emission angle [°]
T	Thrust [N]	λ	Wavelength [m]
t	Time [s]		

ζ	Velocity density particles [m/s]	τ_w	Wall shear stress [Pa]
ρ	Density [kg/m ³]	Φ	Inflow angle [°]
ρ'	Density perturbation [kg/m ³]	Φ	Azimuthal angle [°]
σ_{ij}	Viscous effects	Ω	Rotational velocity [rps]
τ^*	Retarded time [s]	$\Omega_i(x, t)$	Collision operator [-]
τ_{eff}	Turbulent relaxation time		

Table of Figures

Figure 1. Actuator disc model with fluid stream tube defining the domain to implement momentum theory [15].	5
Figure 2. Propeller vortex sheets trailed in helicoidal motion [14].	6
Figure 3. Velocity and force vectors in a cross-section of a propeller's blade element.	7
Figure 4. Sketch of the vortex tube model with light blue colour and the vortex filament emitted by a blade. The red arrows show the bound and free circulation.	8
Figure 5. Simplified sketch of the semi-infinite vortex ring wake model [14].	8
Figure 6. Efficiency curves at different advance ratios and blade angles [17].	9
Figure 7. Thrust coefficient (a) and standard deviation (b) variation with respect to the separation distance of twin rotors compared with the single one [9]. The increase of standard deviation implies the unsteadiness of the thrust.	10
Figure 8. Normalized thrust coefficient of a quadcopter with respect to separation distance variation [10]. The increase in the range of thrust values shows enhanced oscillations.	11
Figure 9. Thrust coefficient variation in time as a function of azimuthal positions [10].	11
Figure 10. Thrust, torque and efficiency coefficients evolution for different advance ratios for the isolated propeller and the middle propeller of the distributed-propeller system by [11].	12
Figure 11. Vorticity evolution for single rotor (a) and twin rotors (b) [9].	12
Figure 12. Vorticity distribution for twin-rotor case with separation distance 2.1R (a) and 2.4R (b) [19].	13
Figure 13. Normalized turbulent kinetic energy contours for single rotor (a) and twin rotors(b). Enhanced turbulence occurs in the area of the two blades close to each other [9].	13
Figure 14. Velocity contours for single rotor (a) and twin rotors (b) in a cross-plane 0.1D behind the rotor plane [9]. The flow separation region is shown inside the circled area attributed to the induced upwash flow by the adjacent propeller.	14
Figure 15. Aerodynamic noise sources [22].	16
Figure 16. Harmonic noise in time spectrum (a) and frequency domain (b). Acoustic energy is distinctively distributed in specific frequencies [23].	16
Figure 17. Theoretical noise patterns for noise sources [23].	17
Figure 18. Broadband noise in time spectrum (a) and frequency domain (b). Acoustic energy is distributed in a range of frequencies [23].	17
Figure 19. Measured noised level emitted around the twin-rotor system [9].	19
Figure 20. Sound pressure level spectrum for different separation distances at azimuthal positions of 180° (a) and 120° (b) [9].	20
Figure 21. Overall sound pressure level emitted around the rotor plane of the quadcopter for different separation distances [10].	20
Figure 22. D1Q3 (a) and D2Q9 (b) velocity sets. Velocities with length $ c_i =1$ and $\sqrt{2}$ are shown in black and grey, respectively. Rest velocity vectors $c_{i=0}=0$ are not shown [28].	23
Figure 23. D3Q19 velocity set with 19 discrete velocities to neighbouring nodes [28]. Properties of the velocity set are given in Table 1.	23
Figure 24. Overview of one cycle of the LBM algorithm [28].	25
Figure 25. Simulated and modelled turbulence scales, including energy flow [35].	26
Figure 26. Lattice elements in 2D view in PowerFLOW [38].	27
Figure 27. Propeller model (a) with its chord length and blade pitch angle distributions (b).	29
Figure 28. Distributed-propeller system (a) with the separation distance between blade tips equal to 2%D (0.004m). The red arrows show the direction of rotation. The DP case with a relative phase angle $\Delta\phi=20^\circ$ is shown in figure (b).	29
Figure 29. Flow domain and variable resolutions (VR) regions in the far-field (a). The acoustic sponge is indicated with red notation. Visualization of the VR regions around the propeller's surface (b). The rotating volume is indicated with blue colour around the blades and the spinner.	30

Figure 30. Visualization of VR11 and VR12 areas around a blade of the propeller.	31
Figure 31. Visualization of the VR regions in the near-field of the three-propeller model (front view).	32
Figure 32. Visualization of the VR regions in the far-field (a) and near-field (b) of the three-propeller model (side view). “Box1” is indicated alongside the near-field of the slipstream (VR11-red coloured) and the outer discretized rectangular areas, i.e. VR10, VR9 and VR8.	32
Figure 33. Zoom in view in the area of blades. Rotating volume (VR12) is indicated with purple colour, while region VR13 is denoted around blade surface.	32
Figure 34. Grid view with different VR areas including all three propellers (a); zoom in view of the separation distance between the propellers (b).	33
Figure 35. Sketch of propeller with the acoustic pressure measurement points at distance 10D, where Point 1 and Point 26 are located at the front and parallel to the rotor plane.	33
Figure 36. Permeable surface locations around the isolated-propeller (a) and distributed-propeller case (b).	34
Figure 37. Time evolution plot of thrust coefficient for Propeller#1 of the baseline model. The light-blue-shadowed area denotes the transient period before convergence.	35
Figure 38. Front view (a) and top view(b) of the experimental setup indicating the main dimensions, reference system and configuration layout [11].	37
Figure 39. Time-averaged thrust coefficient of isolated propeller for different number of fine equivalent voxels. Experimental results are also visible for comparison, with the light yellow colour denoting the uncertainty range.	39
Figure 40. Distributions of time-averaged thrust coefficient per segment of Blade1 at different resolution levels.	39
Figure 41. Time-averaged axial velocity distribution measured upstream of the propeller at 10%D for different resolution levels. The experimental data is plotted for comparison.	40
Figure 42. Time-averaged axial velocity distribution measured downstream of the propeller at 60%D for different resolution levels. The experimental curve is plotted for comparison.	41
Figure 43. Time-averaged thrust coefficient distributions for the three blades of the isolated propeller.	42
Figure 44. Illustration highlighting conventional airfoil separation characteristics at different Reynolds number regimes below 10^6 [43].	43
Figure 45. Pressure coefficient (C_p) curves for the three blades at radial position $r/R=0.5$ (a) and 0.8 (b). ...	43
Figure 46. Phase-locked normalized axial velocity flow contours for Blades 1 (a) and 2 (b) at radial position $r/R=0.5$	44
Figure 47. Grid view of the voxels distributions inside the rotating volume (YZ plane). Zoom in views shows the difference in voxels around Blade1 and Blade2.	44
Figure 48. Case1: Blade 1 is aligned with the Y-axis, while Blades 2 and 3 are oblique by 30° with the Z-axis. The red arrow shows the direction of rotation.	45
Figure 49. Case2 (a): Blade 1 is rotated by 15° wrt Y-axis, and Case3 (b): Blade 1 is rotated by 30° and Blade 2 is aligned with Z-axis. The red arrow shows the direction of rotation.	45
Figure 50. Evolution of thrust coefficient per blade for the different cases of initial azimuthal positions. Case 1 corresponds to a 0° angle for Blade 1 with respect to Y-axis, Case2 corresponds to 15° and Case3 to 30°	46
Figure 51. Grid view of the voxels distributions inside the rotating volume (YZ plane) for Case2: Rotated by 15° wrt to Y-axis. . Zoom in views shows the difference in voxels around Blade1 and Blade2.	46
Figure 52. Pressure coefficient (C_p) values of Blade 1 (a) and 2 (b) at radial position $r/R=0.5$ for all three cases.	47
Figure 53. Phase-locked normalized axial velocity contour for Blades 1 (a) and 2 (b) corresponding to Case 3 at radial position $r/R=0.5$	47
Figure 54. Variation of Overall Sound Pressure Level ($OSPL$) values along the propeller plane ($\theta=90^\circ$) for different resolution levels (a). $OSPL$ values of the 1 st BPF and up to the 5 th BPF [0-4460Hz] for different resolution levels (b).	48
Figure 55. Variation in spectrum level of the acoustic signal along the propeller plane ($\theta=90^\circ$) for different resolution levels.	49
Figure 56. SPL frequency distribution between Case1 and Case2 along the propeller plane ($\theta=90^\circ$). Case 1 corresponds to a 0° angle for Blade 1 with respect to Y-axis, and Case2 corresponds to 15° , as shown in Figure 49.	50

Figure 57. Noise emission angles along the XY plane in the far-field for different resolution levels. *OSPL* values correspond to the frequency range [0-4460Hz] (up to 5th BPF). 50

Figure 58. Difference of *OSPL* noise emission values between solid and permeable surface formulations for low-frequencies [0-4460Hz] (a) and high-frequencies [4460-8920Hz] (b) along the XY plane. 51

Figure 59. Spectrum analysis between solid and permeable surface formulations at azimuthal angles $\theta=100^\circ$ (a) and $\theta=150^\circ$ (b) based on Figure 58. 52

Figure 60. Measurement locations upstream and downstream from the propeller (a). The orientation angles used to measure the velocity distributions in the upstream direction are shown in the right figure(b). 53

Figure 61. Normalized time-averaged axial (a) and tangential (b) velocity distributions of the distributed propellers comparing the numerical and experimental data in the upstream direction ($X/D=-0.1$). 53

Figure 62. Normalized time-averaged axial (a) and tangential (b) velocity distributions of the distributed-propeller case comparing the numerical and experimental data of the wake in the downstream direction ($X/D=0.6$). 54

Figure 63. Time-evolution of thrust coefficient (T_c) for both the isolated-propeller and the baseline case 56

Figure 64. Time-evolution of thrust coefficients for each blade. Propeller's thrust coefficient is also shown on the right vertical axis. 56

Figure 65. Axial velocity contour of the mean flow field for the isolated-propeller case (a) and the distributed-propeller configuration (b). The normalized values are relative to the free-stream velocity. The slipstream extension is annotated with red colour. 57

Figure 66. Comparison of normalized time-averaged axial (a) and tangential (b) velocities between the isolated-propeller and the distributed-propeller case in the upstream direction ($X/D=-0.1$). Velocity components are measured in the three orientations, as shown in Figure 60. 58

Figure 67. Velocity contour based on the semi-infinite vorticity wake tube model(a). Induced axial velocity comparison between CFD analysis and the vorticity tube model (b) upstream of the propeller at $X/D=-0.1$. 58

Figure 68. Sketch of the induced velocities on a point P upstream of propellers. The induced velocities from Propeller#1 are shown with black colour and green the induced velocities from Propeller#2. 59

Figure 69. Induced velocities on a point P located above the Y-axis between the two propellers. The total induced velocity has a component normal to the radial direction that is directed downwards. 60

Figure 70. Thrust distribution difference (δT_c) at rotor disk plane between Propeller#1 of the baseline case and the isolated one. 61

Figure 71. Thrust distribution difference (δT_c) at rotor disk plane between Propeller#2 of the distributed-propeller model and the isolated one. 61

Figure 72. Total pressure coefficient distribution in the slipstream at $X/D=0.1$ of the distributed-propeller case. The red arrows show the direction of rotation. 62

Figure 73. Total pressure differences ($\Delta C_{p,total}/C_{p,total iso}$) between the isolated propeller and Propeller#1 (a) and Propeller#2(b) measured at $X/D=0.1$. The red arrows show the direction of rotation. 62

Figure 74. Comparison of normalized time-averaged axial (a) and tangential (b) velocity distributions between the distributed-propeller case and the isolated propeller. The measurement location is downstream of the propellers at $X/D=0.6$ 63

Figure 75. Out-of-plane vorticity contours for the isolated-propeller case (a) and the distributed-propeller configuration (b). Tip vortices are annotated in downstream locations. 64

Figure 76. Vortex core trajectory comparison for the isolated propeller and distributed propellers. The vortex cores has been tracked based on their location as shown in Figure 75. 64

Figure 77. Isosurface views of the λ_2 criterion ($\lambda_2=-3.5 \times 10^6 \text{ 1/s}^2$) visualising the vortex cores between the propellers (a). Zoom in view at the area between adjacent blades as they rotate in their nearest distance (b). 65

Figure 78. Sketch view of the induced velocities between adjacent vortex filaments. Zoom-in view (top right corner) shows the induced velocities between two points of adjacent vortices along the XY plane. The resulting induced velocities are in 3D space (see the sketch in the bottom left corner). 66

Figure 79. Front view sketch of the induced velocity along the Z-axis from the axial components of the free vorticity (a). The vorticity magnitude contour is shown in the right figure at location $X/D=0.3$ downstream. 67

Figure 80. Top view sketch of the induced velocities along the X-axis from the Z-axis components of the free vorticity (a). Isosurface 3D view of the vortex filament deformation along the X-axis denoted inside the red circle (b). 67

Figure 81. Variation of the thrust coefficient difference of Blade1 between the isolated propeller and Propeller#1 with respect to the azimuthal position during its rotation (a). Time variation of the same thrust coefficient difference of Blade1, indicating the unsteady thrust coefficient component (b). 68

Figure 82. Thrust coefficient distribution along Blade1 at different azimuthal positions (a). The standard deviation of the thrust coefficient distribution during the blade’s rotation (b). 69

Figure 83. Pressure coefficient (C_p) plots with the error-bars indicating the pressure range associated with the unsteady loading during a revolution. The distributions corresponds to different span locations across the blade: (a) at $Y/R=0.5$, (b) at $Y/R=0.7$, (c) at $Y/R=0.8$ and (d) at $Y/R=0.975$ 70

Figure 84. Front view of the distributed-propeller case with 20° relative phase angle between propellers. ... 70

Figure 85. Time evolution of the thrust coefficient of Propeller#1 for the distributed-propeller case with 20° relative phase angle ($DP(\Delta\phi=20^\circ)$). For comparison, the respective values for the isolated-propeller and distributed-propeller ($DP(\Delta\phi=0^\circ)$) case with 0° relative phase angle are shown. 71

Figure 86. Axial velocity contour of the mean flow field for distributed propellers with 20° (a) and 0° (b) relative phase angle. The normalized values are relative to the free-stream velocity. 72

Figure 87. Comparison of the normalized axial velocity distributions between the distributed-propeller cases with 0° ($DP(\Delta\phi=0^\circ)$) and 20° ($DP(\Delta\phi=20^\circ)$) relative phase angle. The measurement location is downstream of the propellers at $X/D=0.6$ 72

Figure 88. Comparison of the total pressure coefficient in the slipstream at $X/D=0.1$ for the distributed-propeller case with 20° (b) and 0° relative phase angle (a). Zoom in views between Propeller#1 and #2. Figure (c) shows the slipstream deformation observed experimentally with a 10° relative phase angle. 73

Figure 89. Phase-averaged isosurface comparison based on λ_2 criterion ($\lambda_2=-7 \times 10^6$) between the distributed-propeller model with 20° relative phase angle (a) and the baseline model (b). 74

Figure 90. Out-of-plane vorticity contours for the distributed-propeller configuration with 20° (a) and 0° relative phase angle (b). The evolution of the vortices E1 and F1 shows the differences between the two cases. 74

Figure 91. Comparison of the T_c evolution of Blade1 in time (a) and the standard deviation of the thrust coefficient distribution along the blade-span (b) between the distributed-propeller case with 20° ($DP(\Delta\phi=20^\circ)$) and 0° relative phase angle ($DP(\Delta\phi=0^\circ)$). 75

Figure 92. Pressure coefficient (C_p) distributions with the error-bars indicating the range of pressure values during a revolution for different span locations across the blade: at $Y/R=0.7$ (a) and $Y/R=0.975$ (b). 76

Figure 93. The *OSPL* emission in the far-field is compared between Propeller#1 of the baseline configuration (DP) and the isolated propeller. The *OSPL* values are computed based on solid surface formulation. 78

Figure 94. Comparison of the *OSPL* distributions of the three-propeller configuration between permeable surface formulation and solid one considering all three propellers. 79

Figure 95. Noise emission values along the XZ plane. Comparison of the *OSPL* values between the isolated propeller and Propeller#1 of the baseline configuration (DP:Propeller#1) based on the solid surface formulation. 79

Figure 96. Snapshots of pressure time-derivatives in the near-field along the XY plane for the isolated-propeller case (a) and the baseline model with three propellers at two different time-frames(b and c)..... 80

Figure 97. Spectral comparison between Propeller#1 of the distributed-propeller case (DP) and the isolated propeller. The comparison is based only on the solid surface formulation and corresponds to azimuthal positions along the XY plane: at propeller plane- $\theta=90^\circ$ (a), at $\theta=130^\circ$ (b) and normal to rotor plane- $\theta=180^\circ$ (c). 82

Figure 98. Spectral comparison between the distributed-propeller case (DP) and the isolated propeller along the XY plane. The comparison is based on the permeable surface formulation and corresponds to azimuthal positions: along propeller plane- $\theta=90^\circ$ (a), at $\theta=130^\circ$ (b) and normal to rotor plane- $\theta=180^\circ$ (c). 83

Figure 99. Comparison of the *OSPL* noise emission along the XY plane between the baseline configuration ($DP(\Delta\phi=0^\circ)$) and the case with 20° relative phase angle($DP(\Delta\phi=20^\circ)$). The *OSPL* values are computed based on permeable (a) surface formulation and the solid one for Propeller#1(b). 84

Figure 100. Comparison of the *OSPL* noise emission along the XZ plane between the baseline configuration (DP($\Delta\phi=0^\circ$)) and the case with 20° relative phase angle(DP($\Delta\phi=20^\circ$)). The *OSPL* values are computed based on permeable (a) surface formulation and the solid one for Propeller#1(b). 84

Figure 101. Snapshots of the pressure time-derivatives in the near-field along the XY plane at two frames of the distributed-propeller model with 20° relative phase angle. The region of high- and low-pressure fluctuations is indicated with black in front of Propeller#1 and between the propellers with red circles. 85

Figure 102. Spectrum comparison between Propeller#1 for the case with 20° (DP($\Delta\phi=20^\circ$)) and 0° (DP($\Delta\phi=0^\circ$)) relative phase angle. The comparison is based on the solid surface formulation and corresponds to azimuthal positions: normal to rotor plane- $\theta=180^\circ$ (a) and along propeller plane- $\theta=90^\circ$ (b) along the XY plane..... 86

Figure 103. Spectrum comparison between the distributed-propeller models with 20° (DP($\Delta\phi=20^\circ$)) and 0° (DP($\Delta\phi=0^\circ$)) relative phase angle. The comparison is based on the permeable surface formulation and corresponds at $\theta=75^\circ$ along the XY plane..... 86

Figure 104. Points' location around the distributed-propeller system along the XY and XZ planes..... 87

Figure 105. Comparison of the *OSPL* values between the isolated propeller and the distributed-propeller model with 0° and 20° relative phase angles at different azimuthal positions..... 87

List of Tables

Table 1. Properties of the D3Q19 velocity sets. The speed of sound for all of these velocity sets is c_s 24

Table 2. Flow parameters of the model. 34

Table 3. Thermodynamic parameters of the air..... 34

Table 4. Boundary conditions parameters..... 35

Table 5. Measurement data with sampling frequencies..... 36

Table 6. Time-averaged thrust coefficient values at different resolution levels. 39

Table 7. Thrust and thrust coefficients of the propeller's blades. 41

Table 8. Time-averaged thrust coefficients (T_c) of isolated- and three-propeller cases computed numerically in PowerFLOW and experimentally. 52

Table 9. Time-averaged thrust coefficient (T_c) values comparison between the isolated-propeller and distributed-propeller models..... 56

Table 10. Time-averaged thrust coefficients and standard deviation comparison between the baseline model (DP($\Delta\phi=0^\circ$)) and the case with 20° relative phase angle (DP($\Delta\phi=20^\circ$)). 71

1

Introduction

The development of new aircraft concepts with innovative propulsion systems follows the demand for sustainable development in aviation to achieve future goals for low noise and pollutant emissions [1]. The Advisory Council of Aviation Research (ACARE) has set the emission goals to be reduced by 75% in CO₂ emissions per passenger kilometre, 90% in NO_x emissions and 65% of the perceived noise level emissions compared with the measurements in 2000. The development of new propulsion systems and the further investigation of already developed propulsive configurations could broaden the design space and accomplish these goals. The concept of distributed propulsion systems belongs to the second category, as similar concepts have been developed in the past. Although it has been developed since the early 1920s [2], it was until the development of the all-electric and hybrid-electric aircraft concepts that this propulsive configuration was considered feasible. The implementation of these systems in electric aircraft could result in the electrical vertical take-off and landing (eVTOL) for urban air mobility [3]. Among the benefits of distributed propulsion are the spanwise lift augmentation [4], high lift operation [5] and noise shielding if parts of the systems are integrated into the airframe structure [4]. New designs incorporate distributed-propeller (DP) systems, where multiple propellers are used to produce thrust. Such designs are the X-57 Maxwell [6] aircraft with two main propulsors positioned at the wing-tip and twelve smaller propellers distributed in the spanwise direction at the leading edge. Joby S2 vehicle [7] is another aircraft design with 12 tilted propellers, each one of them are connected with their respective motor. Other applications of distributed propulsion systems with propellers are the Unmanned Aerial Vehicles (UAVs), with many designs under development, such as the NASAs' GL-10 UAV [8] with ten tilt-rotor propulsors. In such designs, the propellers are closely-placed, operating at high thrust setting and hover conditions, making the in-depth understanding of their aerodynamic behaviour and the potential changes in their performance a necessity.

In literature, the study of aerodynamic interactions has been examined in systems with two or more rotors focusing primarily on hover conditions. When multiple propellers operate at a close distance, their aerodynamic performance is affected. The thrust diminishes as a result of the interaction between propellers when the separation distance is small, i.e. the distance between propellers blades. In the study of a twin-rotor system in hover, Zhou, et al. [9] noticed a small drop of the thrust coefficient (up to 2%) and a drastic increase of force fluctuations when the separation distance of the two rotors decreased. Other studies found thrust reduction up to 7.93% [10] with simultaneous enhancement of thrust oscillations for small separation distances. The reason for this performance drop has been associated with the induced flow by the adjacent propellers, which results in a region of flow recirculation downstream of the rotors [9]. However, a recent study of a distributed-propeller system in forward flight [11] suggested that the thrust drop should be attributed to the blockage effect due to the nacelle. Another aspect of these studies for the distributed-propeller systems refers to the evolution of the slipstream. When the rotors operate in close proximity, the slipstream deforms in a way that approaches adjacent wake flows. The tip vortices interact with the corresponding vortices of the nearby rotors, distorting their trajectory, causing fast merging and dissipation. This behaviour of the tip vortices has been associated with the occurring thrust fluctuation ([8, 10]). Since

most of the studies refer to hover conditions, it is interesting to examine the behaviour of distributed-propeller systems in forward flight. In forward flight, the dominance of inertia forces compared to the viscous ones would result in less intense viscous interactions than the respective ones in hover for the same distributed-propeller system. Thus, it is expected that the impact on aerodynamic behaviour to be less significant than in hover without large deformation of the slipstream. In addition, the interaction between adjacent propellers remains unexplored at these conditions. The unsteady effect due to the propellers interference needs to be investigated to understand the mechanism that affect the oscillatory behaviour of the thrust, but also the effect on the acoustic signature.

The aeroacoustic behaviour of a distributed-propeller system has been associated with the aerodynamic phenomena observed in this system. In the literature, the aeroacoustic signature of the multi-rotors system was associated with the intensified flow interactions due to the small distance between adjacent propellers. When the separation distance in this system decreases (i.e. propellers are close to each other), there is a noise level increase in both tonal and broadband components. The increase in tonal noise level is attributed to the unsteady loading of the blades due to the thrust fluctuations that occur in small separation distances. The increase of tonal noise for the case of four-rotors is 3-8 dB at almost all harmonics [12]. In parallel, broadband noise increase was related to the turbulent interactions, i.e. the mixing of tip vortices and dissipation that cause turbulence increase and thrust fluctuations in the region between the rotors[9]. The noise increase is noticed in a direction normal to the rotational plane, while the impact of the DP system along the plane of rotation is minor. Although it is generally mentioned that there is a noise level increase of a multi-rotor system forming a dipole pattern, the association of the mechanisms in the aerodynamics performance with the acoustic signature is not clearly stated. So, it is required to explore further how the noise emission of the system is affected by the propeller loading and the interference of the acoustic waves emitted by the propellers in forward flight conditions.

A technique to achieve noise level reduction, namely phase angle control, is based on the control of the azimuthal location position of the blades of a propeller. The azimuthal position of blades in distributed-propeller configurations affects the noise emission by changing “the noise patterns due to constructive and destructive interference”[13]. Pascioni, et al. [37] examined the potential benefit of phase control in distributed electric propulsion systems for noise reduction and showed that a reduction is possible up to 20 dB decrease at specific emission angles, with possible degradation of the benefit when other noise sources are considered. However, the aerodynamic interaction between the propellers was not considered in this study, and the flow field changes as a result of the relative phase angle remain unexplored. Thus, the relative phase angle effects require further investigation, considering the aerodynamic interference between adjacent propellers.

1.1 Research objective

The research objective is the investigation of the aerodynamic interactions and aeroacoustic behaviour of distributed-propeller configuration, including the effects of phase angle variation by performing high fidelity numerical simulations in a multi-propeller configuration in forward flight.

1.2 Research questions

- What are the physical mechanisms associated with the differences in the aerodynamic and aeroacoustic performance of a distributed-propeller configuration compared with an isolated propeller?
 - How are the inflow conditions affected by multiple adjacent propellers?
 - How are the slipstream velocity and pressure distribution affected by the adjacent propellers?
 - What is the change in wake flow evolution of multiple adjacent propellers compared with an isolated propeller?
 - What are the reasons for the noise emission change due to multiple adjacent propellers?
- To what extent does the propeller’s relative phase angle affect a distributed-propeller model's aerodynamic and aeroacoustic performance?

- What are the reasons for the change in aerodynamic and aeroacoustic performance of a model with relative phase angle compared with a model without phase angle variation?
- What is the change in wake flow evolution of a model with phase angle variation compared with a model without it?
- How is the noise emission affected by the phase angle?

The outline of this research investigation structures the report such that the theoretical background with the literature review findings in Chapter 2. Chapter 3 presents the methodology of this numerical study, describing the flow solver and the numerical setup of the models. Subsequently, the validation and resolution study of the models are mentioned in Chapter 4. Then, Chapter 5 presents the DP system's aerodynamic analysis, including the effect of the relative phase angle. In Chapter 6, the aeroacoustic analysis follows before concluding with the main conclusions and recommendations for potential expansion of the research in Chapter 7.

2

Theoretical Background and Literature Review

2.1 Propeller aerodynamics

In this section, the propeller theory is briefly presented, describing the aerodynamic performance of a single propeller through the actuator disk theory, the blade element momentum analysis and the vortex flow analysis. The actuator disk theory examines the propeller's performance from the perspective of momentum change through a stream tube analysis of the flow. This simple concept is essential in understanding the upstream and downstream effects of the propeller. When the viscous phenomena in the propeller slipstream are considered, a complete model of the propeller is generated, incorporating the effects of the flow structures on the propeller and the slipstream evolution in the downstream direction. Therefore, understanding these concepts is the cornerstone in analysing the distributed-propeller system, as several concepts of these theories will be discussed later in the analysis.

2.1.1 Actuator disk theory

Propellers are thrust-generating devices that impart axial momentum to the flow. According to actuator disk theory [14], a propeller can be modelled via a thin circular disc with orientation perpendicular to the direction of motion. The flow is also considered incompressible, inviscid and uniform across the disc area, neglecting the viscous phenomena and slipstream rotation. A stream tube defines the flow domain that includes the moving fluid upstream and downstream of the propeller disc (Figure 1). The thin disc can sustain a pressure difference in the upstream and downstream sides while increasing the momentum of the passing fluid. This means that the thrust force and power are computed by implementing momentum theory for the stream tube, as given in Eq. (1.1). Due to the increase of momentum flow, there is a slipstream contraction, i.e. reduction of the cross-sectional area of the stream tube.

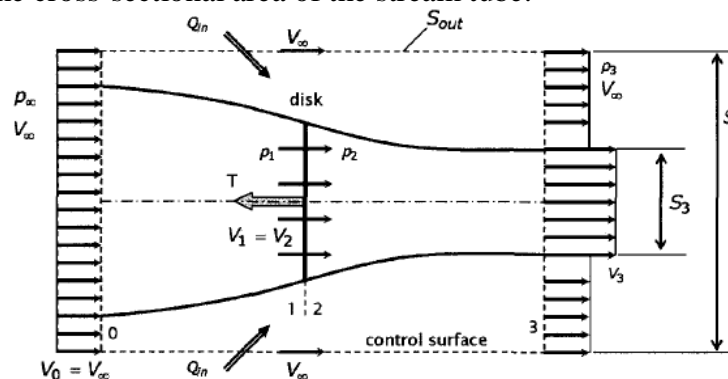


Figure 1. Actuator disk model with fluid stream tube defining the domain to implement momentum theory [15].

$$\begin{aligned}
T &= \dot{m}(V_3 - V_\infty) \\
P &= \frac{1}{2} \dot{m}(V_3^2 - V_\infty^2)
\end{aligned}
\tag{1.1}$$

Where \dot{m} is the mass flow rate through the rotor disc, V_3 is the downstream velocity, and V_∞ is the free-stream velocity, as shown in Figure 1.

However, a limitation of the actuator disc theory is that viscous phenomena and slipstream rotation are neglected. The idea behind the vortex analysis is that each finite element of the blade produces a trailing vortex sheet. The lift force component produced by a blade element is related to the bound circulation (Kutta–Joukowski Theorem [14]), leading to a circulation distribution across the blade. This circulation change across the blade results in the shedding of a vortex from the trailing edge of each blade element. Combining all these vortices from all blade elements forms the slipstream, which travels downstream in the form of helices (Figure 2). These vortex sheets, as they travel downstream, roll up into a vortex filament [15]. Slipstream thus consists of axial and tangential (swirl) velocity components that should be included in the propeller analysis. A direct effect of these vortex sheets is the induced velocities at the location of the blade. So, the shedding vorticity from the blades affects the bound circulation, which determines the blade loading and, as a result, propeller performance [14]. Therefore, the combination of the bound circulation and the trailing vorticity from the blades leads to induced velocity, which is a part of the resultant velocity vector of the blade element, as shown in Figure 3. The induced effects of the vortex sheets are of great importance in the distributed-propeller system. The fact that propellers operate in close proximity make these induced effects relevant, affecting the behaviour of adjacent propellers and the evolution of neighbouring slipstream flows.

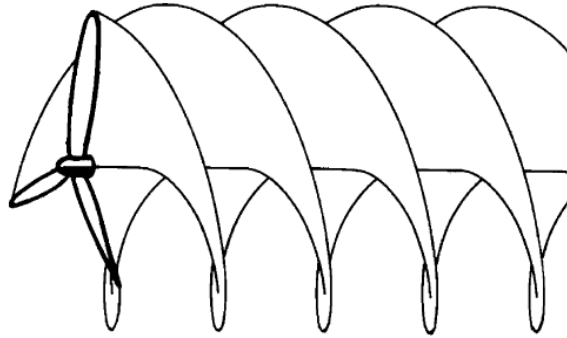


Figure 2. Propeller vortex sheets trailed in helicoidal motion [14].

2.1.2 Blade element momentum analysis

Blade element momentum analysis combines the previously presented momentum theory with the vortex effects on a blade element that determines its performance. Each blade of the propeller can be divided into blade element sections. The velocity and force vectors can be drawn on the blade section in a random radial position, as shown in Figure 3 (kinematic and dynamic analysis of the element). The cross-section view of a 2D element is shown in Figure 3, where Ω is the angular velocity, r the local radius of the blade element, U_∞ the free-stream velocity and U the inflow velocity, while the V_t and V_a are the tangential and axial induced velocities, respectively. Induced velocity is considered “the resultant velocity at a point due to the entire system of bound and free vorticity” ([14]), attributed to the disturbance of the fluid due to the blade motion. Finally, the inflow angle φ and the angle of attack α are shown in Figure 3.

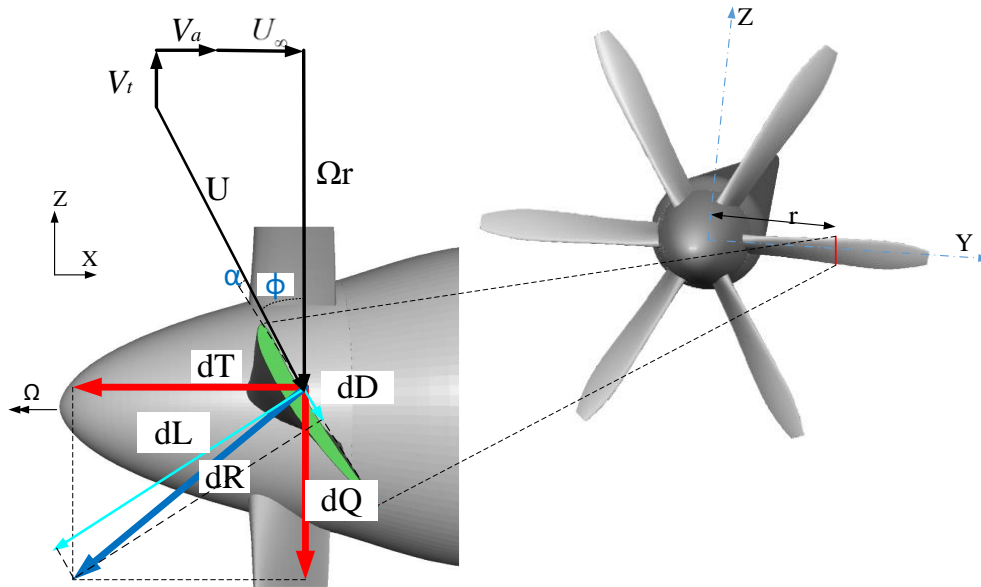


Figure 3. Velocity and force vectors in a cross-section of a propeller's blade element.

On each blade element, a resultant force dR is generated by the incoming flow U , which is decomposed into a component perpendicular and parallel to the inflow, the lift (dL) and drag (dD) force, respectively (see Figure 3). The decomposition of the resultant force into the axial and tangential direction leads to thrust (dT) and torque (dQ) forces. The two forces can be computed based on the lift and drag forces as:

$$\begin{aligned} dT &= dL \cos(\varphi) - dD \sin(\varphi) \\ dQ &= dL \sin(\varphi) + dD \cos(\varphi) \end{aligned} \quad (1.2)$$

Inflow angle (φ) is defined based on the axial flow velocity V_a and the tangential one V_t , as shown below:

$$\varphi = \tan^{-1} \left(\frac{V_t}{V_a} \right) \quad (1.3)$$

2.1.3 Slipstream tube model

Due to the helicoidal motion of the vortex sheets in the slipstream, the calculation of the velocity field induced by these sheets is quite complex. Therefore, a simplified model is used to analyse the induced velocity components, i.e. the vorticity tube model [16]. This model represents the main features of a propeller based on the vortex system. The vortex system emanates from a propeller and rolls up into a set of helical vortex filaments that travel downstream. It consists of the bound vorticity (Γ_{bound}) of the blade surface, the root vortex (Γ_{root}) due to the rotation of the propeller and the free vorticity trailed by the blade tip (Γ_{Tip_vortex}). Therefore, according to the vorticity tube model, the helicoidal vortex sheets are replaced by two superimposed continuous distributions of vorticity. One distribution consists of axial vorticity, i.e., parallel to the axis of rotation (see Figure 4). The other vorticity distribution consists of vortex rings located on cylindrical surfaces normal to the axis of rotation. Figure 4 illustrates the vorticity tube model where the vortex rings and axial vortices are denoted with light blue. The trailing vorticity related to tip vortex (Γ_{Tip_vortex}) is decomposed to Γ_x along the axial lines and Γ_θ along the circular rings.

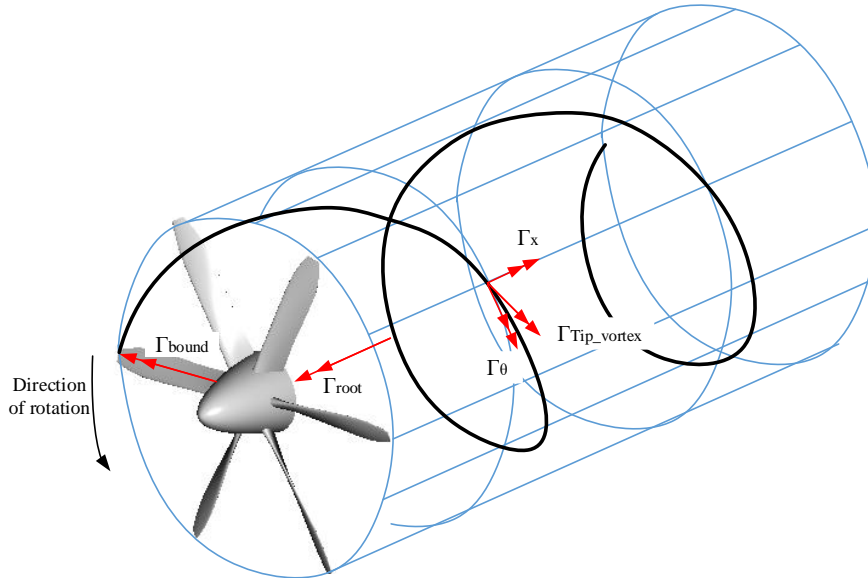


Figure 4. Sketch of the vortex tube model with light blue colour and the vortex filament emitted by a blade. The red arrows show the bound and free circulation.

To fully understand the induced effects of a distributed-propeller system, it is essential to present, at first, the induced effects based on the vorticity model. The root vorticity (Γ_{root}) and axial vorticity (Γ_x) contribute to slipstream rotation without any induced effect in the streamwise direction. The bound vorticity (Γ_{bound}) contributes only downstream of the propeller since its effect, in the upstream direction, is compensated by the free vorticity [15]. Thus, it is only the tangential vorticity Γ_θ that affects the flow upstream of the propeller disk.

So, in principle, the propeller model can be replaced by a cylindrical surface with uniformly distributed vorticity of strength γ per unit length. This vortex sheet may be considered as a uniform distribution of vortex rings. This cylinder extends indefinitely in one direction to model the slipstream properly (Figure 5). This stack of circular dipole sheets induces velocity components in axial and radial directions upstream and downstream of the propeller. This vorticity tube model will also be implemented to assess the distributed-propeller model and evaluate the induced velocities between the vortex sheets of adjacent propellers.

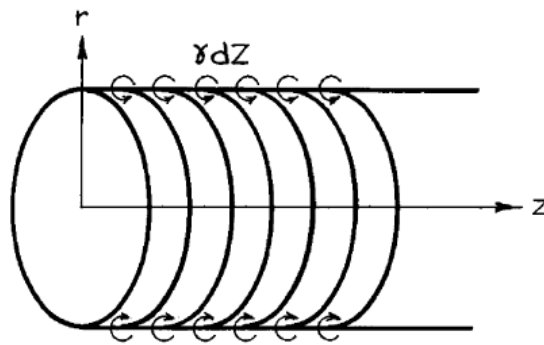


Figure 5. Simplified sketch of the semi-infinite vortex ring wake model [14].

2.1.4 Propeller's performance coefficients

Propeller's performance coefficients that will be discussed in the analysis are presented in this section. The thrust coefficient can be expressed in different forms relative to rotational and free-stream velocity. In the chapters below, the first expression of the thrust coefficient is used based on the inflow velocity.

$$T_C = \frac{T}{\frac{1}{2} \rho U_\infty^2 A_p} \tag{1.4}$$

$$C_T = \frac{T}{\rho n^2 D^4}$$

Where T is propeller thrust, U_∞ the free-stream velocity, A_p is the propeller disk area, D is the diameter, ρ is the density, and n is the rotational speed in rev/s. Similarly, torque coefficient (Q_c) is defined based on the free-stream velocity.

$$Q_c = \frac{Q}{\rho U_\infty^2 D^3} \quad (1.5)$$

Where Q is the propeller shaft torque. The propeller efficiency is defined as the ratio between the effective propulsive power and the shaft power(P):

$$\eta = \frac{TU_\infty}{P} \quad (1.6)$$

Advance ratio is another parameter related to the performance of a propeller, correlating the free-stream velocity with the rotational speed and blade diameter. This non-dimensional number expresses the forward motion of the propeller relatively to the rotational velocity (Eq. (1.7)), i.e. for small values of the advance ratio (near zero), the forward direction is negligible compared with the rotational speed (high blade loading). In contrast, for values near 1, the forward motion dominates (low blade loading).

$$J = \frac{U_\infty}{nD} \quad (1.7)$$

The advance ratio is a useful coefficient to determine the design condition of the propeller for optimum efficiency. Propellers are usually designed to operate optimally at a specific design point, for example, the aircraft's cruise conditions, while there are off-design flight conditions (take-off, steep climb) that the efficiency is reduced. So, a propeller with a fixed-pitch angle will have different efficiency values at different advance ratios. A fixed-pitch propeller that operates at flight speeds that are much lower than the cruise speeds, namely low advance ratios, suffers from a sharp drop in its efficiency, attributed to blade stall conditions. Thus, it is essential to examine the behaviour of a distributed-propeller system in a high advance ratio during cruise conditions, investigating the change in thrust production due to the aerodynamic interference that will result in an efficiency alteration. To avoid an operation at low efficiencies, propellers are often equipped with variable pitch mechanisms. This enables the proper selection of the blade angle that will allow for optimum efficiency depending on the flight phase, as shown in Figure 6. Since this mechanism will increase the system's complexity and overall weight, it has not been implemented in light aircrafts like UAVs.

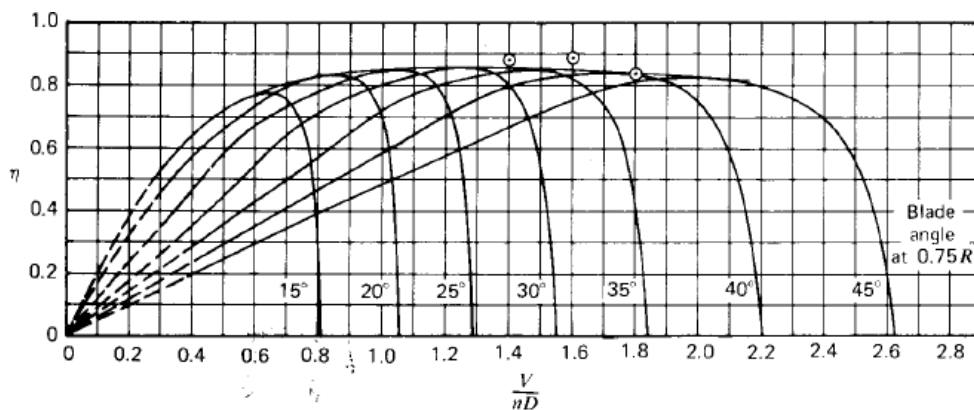


Figure 6. Efficiency curves at different advance ratios and blade angles [17].

2.2 Distributed-propeller aerodynamics

In the following sections, the aerodynamics of multiple-propeller systems is described focusing on performance and flow field changes according to the literature. Due to the existence of many rotors operating in close proximity, the aerodynamic performance is affected by the interference of adjacent rotors. The

aerodynamic performance of multiple propellers configurations is presented in the first section based on experimental and numerical studies, and subsequently, a description of the flow physics is mentioned.

2.2.1 Aerodynamic performance

The experimental investigation of the aerodynamic and aeroacoustic behaviour of a twin-rotor configuration performed by Zhou, et al. [9] showed that there is a small drop of the thrust coefficient (up to 2%) and a drastic increase of force fluctuations when the separation distance of two rotors decreases. Figure 7 illustrates this behaviour, where the change of both the normalized thrust coefficient and standard deviation of thrust for the twin-rotor case are compared with the single rotor case. For separation distances $L/D > 0.5$, the performance reduction and the thrust fluctuations are diminished as the propeller's behaviour approaches the corresponding one of the single rotor. Thus it can be conjectured that the twin-rotor performance is affected by the interactions between adjacent rotors at close distances. The normalization for Figure 7 is relative to the thrust coefficient of the single rotor 0.013 and the standard deviation of thrust 0.21 N.

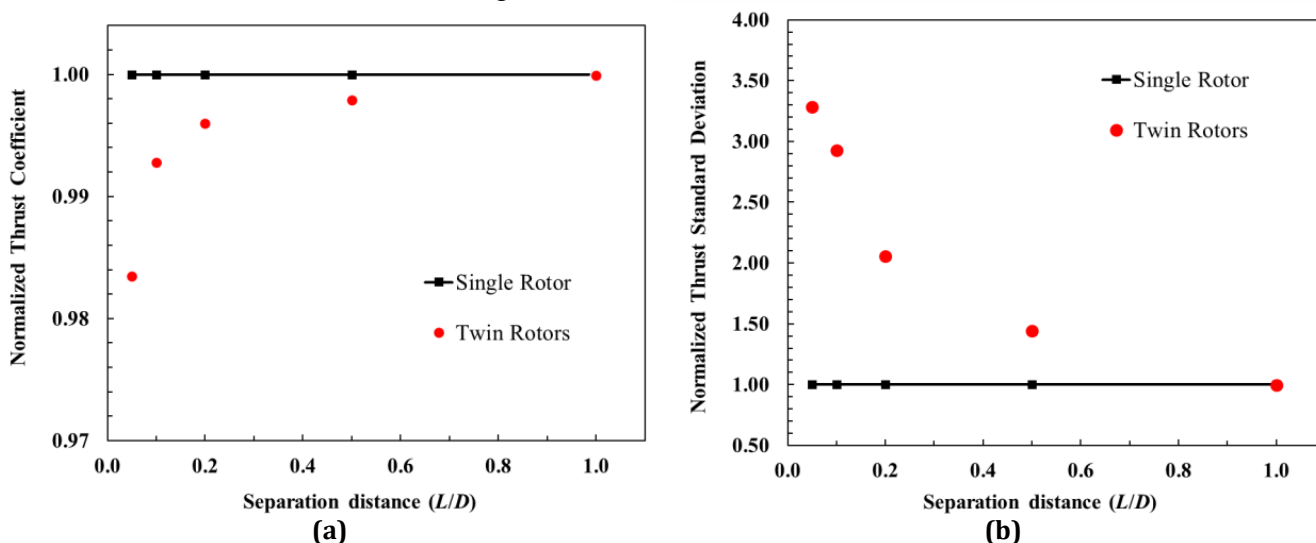


Figure 7. Thrust coefficient (a) and standard deviation (b) variation with respect to the separation distance of twin rotors compared with the single one [9]. The increase of standard deviation implies the unsteadiness of the thrust.

Similar trends in the performance of multirotor systems have also been observed in the numerical studies of Lee and Lee [10], Yoon, et al. [18]. The configurations that have been studied incorporated systems with four rotors examining the effect of the distance between propellers. In the analysis of Lee and Lee [10], there is a reduction in thrust coefficient output when the separation distance is small, as shown by the thick red line in Figure 8, which reaches a reduction up to 7.93% at 0.2D distance. It is also evident that the thrust standard deviation increases as the distance reduces, as denoted by the range of values for small distances. So, severe thrust fluctuations, associated with the thrust standard deviation, occur when the rotors separation distance gets small, indicating that the flow field around the quadcopter becomes unsteady. Although this analysis refers to a quadcopter, the aerodynamic performance presents common characteristics with the experimental data of the twin-rotor configuration of Zhou, et al. [9]. In all cases, it is observed that the thrust fluctuations start to develop for separation distances smaller than $0.4d/D$, while they get intensified for a distance smaller than $0.2d/D$, as shown by the increase of thrust standard deviation. In parallel, the performance drop and thrust oscillations are negligible for separation distances greater than $0.75d/D$, which denotes that the propeller would operate as isolated propellers without any interaction.

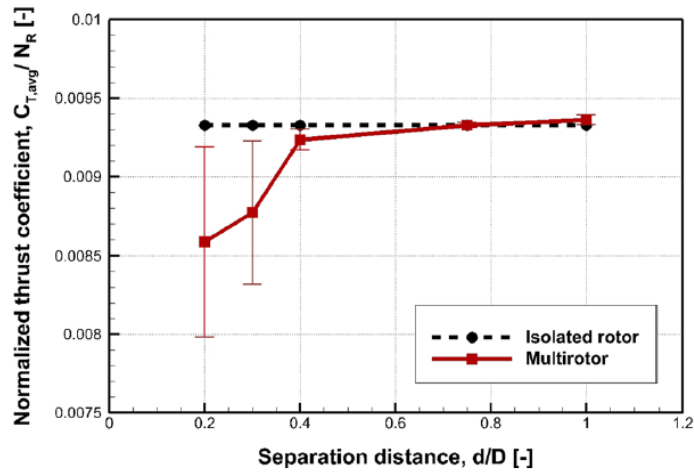


Figure 8. Normalized thrust coefficient of a quadcopter with respect to separation distance variation [10]. The increase in the range of thrust values shows enhanced oscillations.

Figure 9 depicts the thrust coefficient evolution in time for different values of the separation distance. In the cases where the separation distance is small ($d/D=0.2$) and the rotors are close to each other, the thrust curve presents severe fluctuations, as shown in Figure 9. Thrust fluctuations are more intense when the separation interval is $0.2d/D$ and $0.3d/D$, while oscillations disappear for distances greater than $0.75 d/D$. The oscillations are present periodically in every rotation of the rotor. So, these oscillations denote the unsteady character of the aerodynamic interaction.

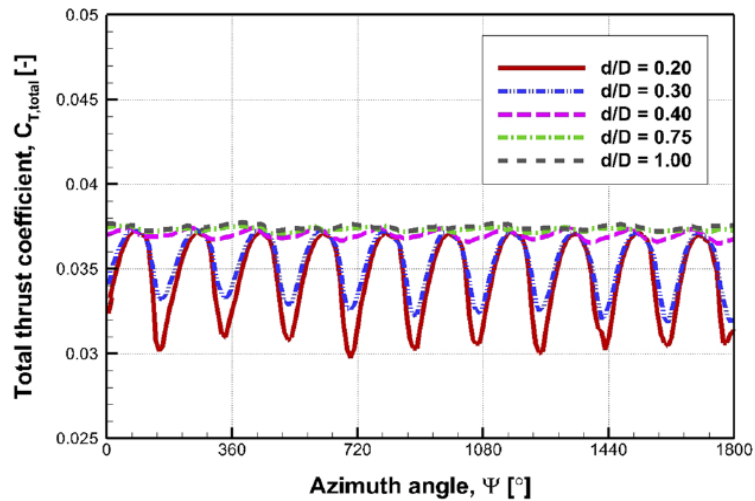


Figure 9. Thrust coefficient variation in time as a function of azimuthal positions [10].

A recent study by de Vries, et al. [11] has investigated the aerodynamic interactions of distributed propellers in forward flight, focusing on performance change and slipstream evolution. This study investigates the induced effects between adjacent rotors, considering the propellers' flow changes upstream and downstream. The results from this experimental study will be used to validate the numerical model developed in the present report. The propeller's performance was investigated for various advance ratios and compared with the isolated propeller. A slight decrease in the propeller's thrust was observed for all advance ratios, resulting in an efficiency loss of 1.5% (see Figure 10). The reduction in thrust for all advance ratios (J) outweighs the reduction in torque (Q_c), resulting in overall efficiency (η) drop. An insightful aspect of this study is the analysis of the induced effects upstream of the propellers and the description of the slipstream evolution. In the upstream direction, an axial velocity increase was noticed, accompanied by the tangential velocity variation. This behaviour was attributed to the induced effects of the trailing vorticity of the adjacent rotors, as will be discussed later. The slipstream analysis revealed a reduction in axial velocity combined with a deformation of the slipstream for the distributed-propeller system. A change in the disk loading was also observed, as there was a decrease in loading as the blade approached the adjacent propeller and an increase as it retreated. Among the design parameters that have been included in this study, it was

observed that the propeller’s performance is insensitive to the relative blade phase angle, with the variation of thrust being less than 0.5% of the mean propeller’s thrust. Although this investigation examined the effects of various parameters of the distributed-propeller system, the unsteady aerodynamic effects between adjacent blade tips and tip vortices were not studied, as intended to be examined in the present analysis.

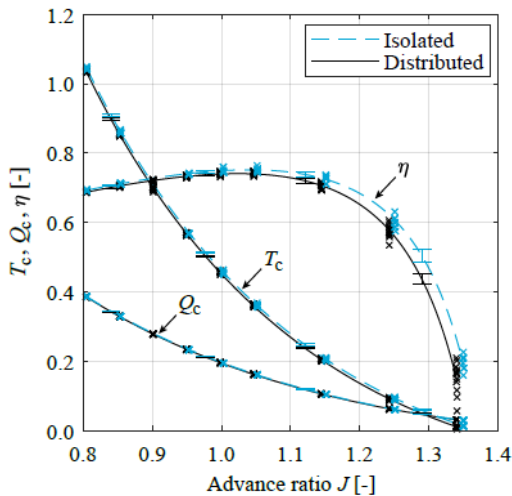


Figure 10. Thrust, torque and efficiency coefficients evolution for different advance ratios for the isolated propeller and the middle propeller of the distributed-propeller system by [11].

2.2.2 Flow physics

The quantification of the aerodynamic behaviour of the multi-rotor systems in both hover and forward flight showed degradation of performance attributed to the rotor-to-rotor interaction. Therefore, it is necessary to identify the origins of such effects by investigating the wake of the rotors and the interactional flow phenomena that take place.

Both experimental and numerical analyses have been performed to clarify the aerodynamic interactions between propellers in hover conditions. The experimental study performed by Zhou, et al. [9] investigated the interactions of the wakes of two adjacent rotors in hover conditions. Vorticity plots provide us with data on the motion of the tip vortices and shear layers shed by the blades, as shown in Figure 11. The tip vortices interaction in the twin-rotor case drives the vortices to merge and dissipate faster than the single rotor case. Another observation from Figure 11 is related to the direction of tip vortices. It is known that wake contraction occurs downstream of an isolated rotor. This is shown by the location of tip vortices 1 and 2 for the isolated rotor in Figure 11a, where their radial location is at $X/D \sim 0.4$. Although contraction is still observed in the twin-rotor case, it is also noticed that the tip vortices are “dragged” by the adjacent vortical structures. Tip vortices 1 and 2 in the twin-rotor configuration are located at $X/D \sim 0.5$.

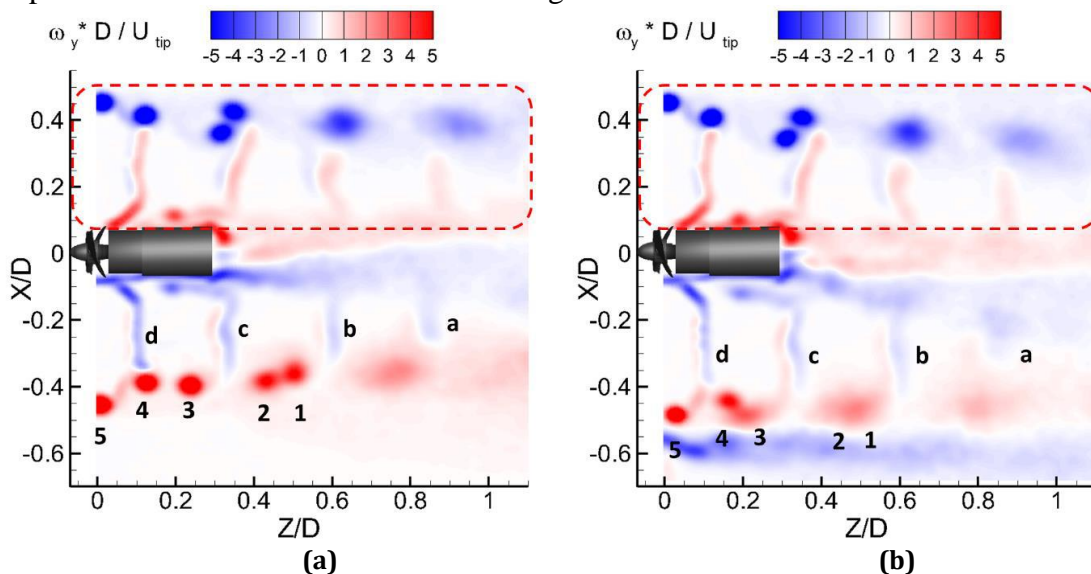


Figure 11. Vorticity evolution for single rotor (a) and twin rotors (b) [9].

Similar observations about the motion and the interference of tip vortices were drawn by Shukla and Komerath [19]. Their study referred to an experimental investigation of rotor-to-rotor interactions of two rotors in hover in a low Reynolds regime. The interaction of the tip vortices (Figure 12) intensifies at small separation distances as the wake flows of the two rotors lose their structures and deviate from their trajectory. As the flow moves downstream, tip vortices merge with the adjacent vortices and split into smaller vortices inducing turbulence production.

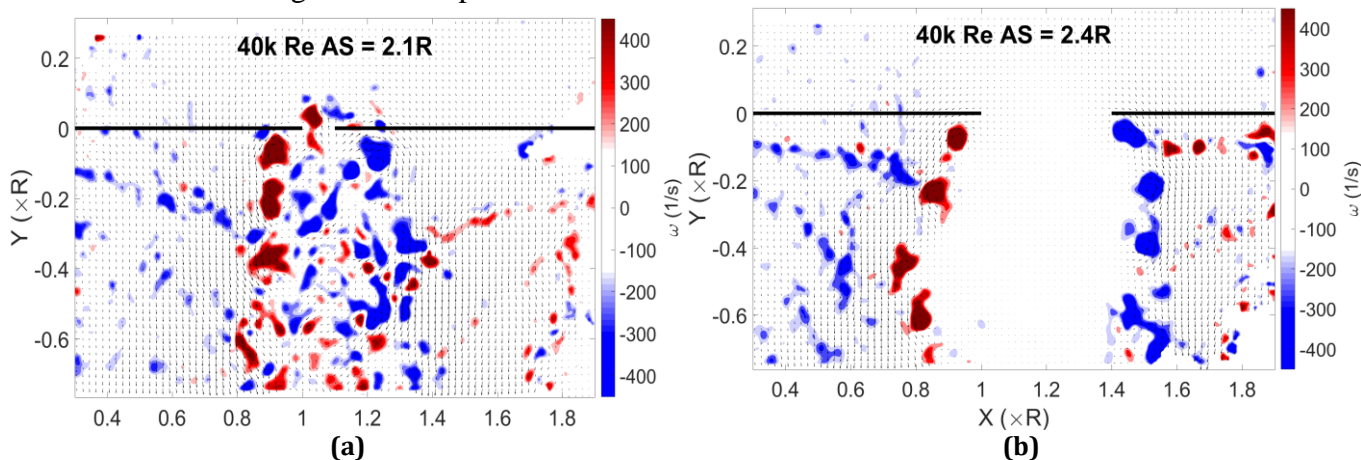


Figure 12. Vorticity distribution for twin-rotor case with separation distance 2.1R (a) and 2.4R (b) [19].

The interaction of tip vortices between adjacent propellers leads to the enhancement of turbulence, as shown in the turbulent kinetic energy distribution (Figure 13). Shedding vorticity is related to the turbulence produced by the blade during its periodic motion. So, the turbulent kinetic energy is also increased near the blade tip of an isolated propeller, as shown in Figure 13. This effect appears to intensify in the case of twin-rotor in the region where the two adjacent blades are close, as the area with high turbulence increases. The enhanced turbulent kinetic energy in the region between the adjacent blades is strongly connected with the thrust fluctuations as a result of the tip vortices interactions.

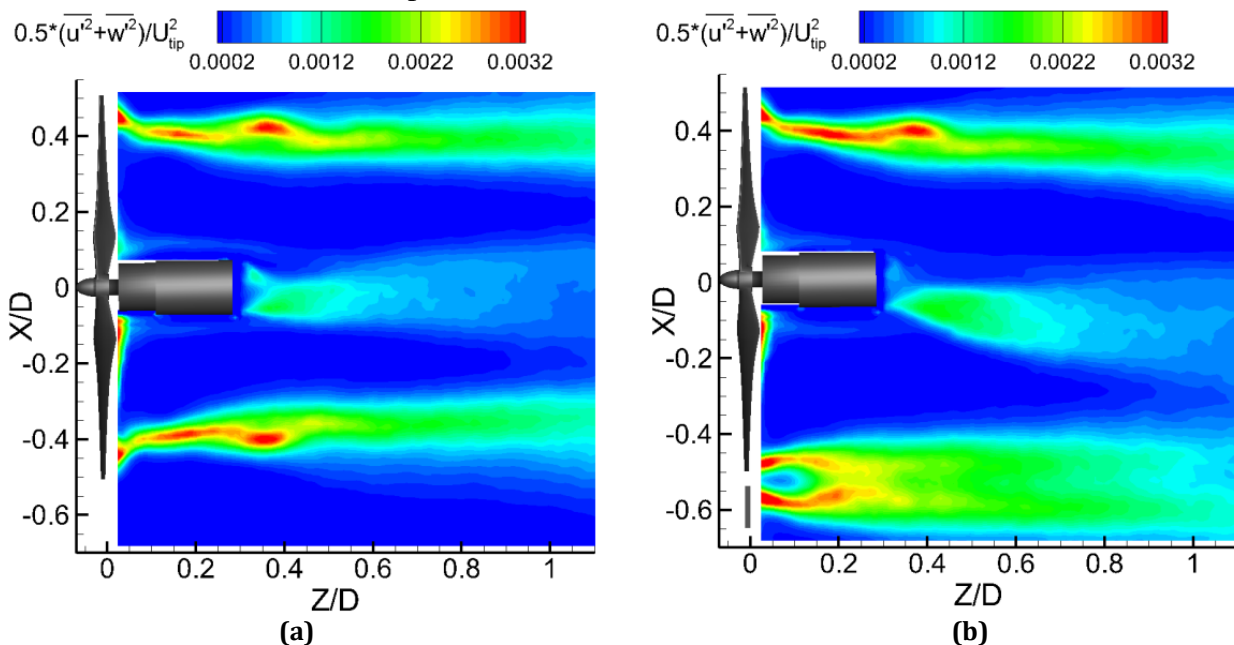


Figure 13. Normalized turbulent kinetic energy contours for single rotor (a) and twin rotors (b). Enhanced turbulence occurs in the area of the two blades close to each other [9].

The resulting flow due to the wake interactions is visible by observing the velocity contours right behind the twin-rotor configuration (Figure 14). A single rotor's fully symmetrical velocity contour has turned into a non-symmetrical contour due to the wake interference. The inspection of the velocity contour downstream of the twin-rotor reveals a region with flow separation at the top right corner of Figure 14 (b) inside the circled area. The flow separation area is denoted by the velocity vectors (small arrows) that create a circular shape (i.e. a recirculation region). The author attributes flow separation to the upwash flow from

the adjacent blade and the radial flow across the blade. The vertical arrow in Figure 14 depicts the induced flow by the adjacent propeller with an upwash direction that affects the adjacent rotor. It is also believed that this interaction has a periodic frequency, as it occurs every time the blades pass through that area. When the two rotors are approaching each other, the upwash flow interacts with the blade radial flow leading to separation. The flow separation is associated, as well, with the augmented turbulent energy and the fluctuations that occur in the same region.

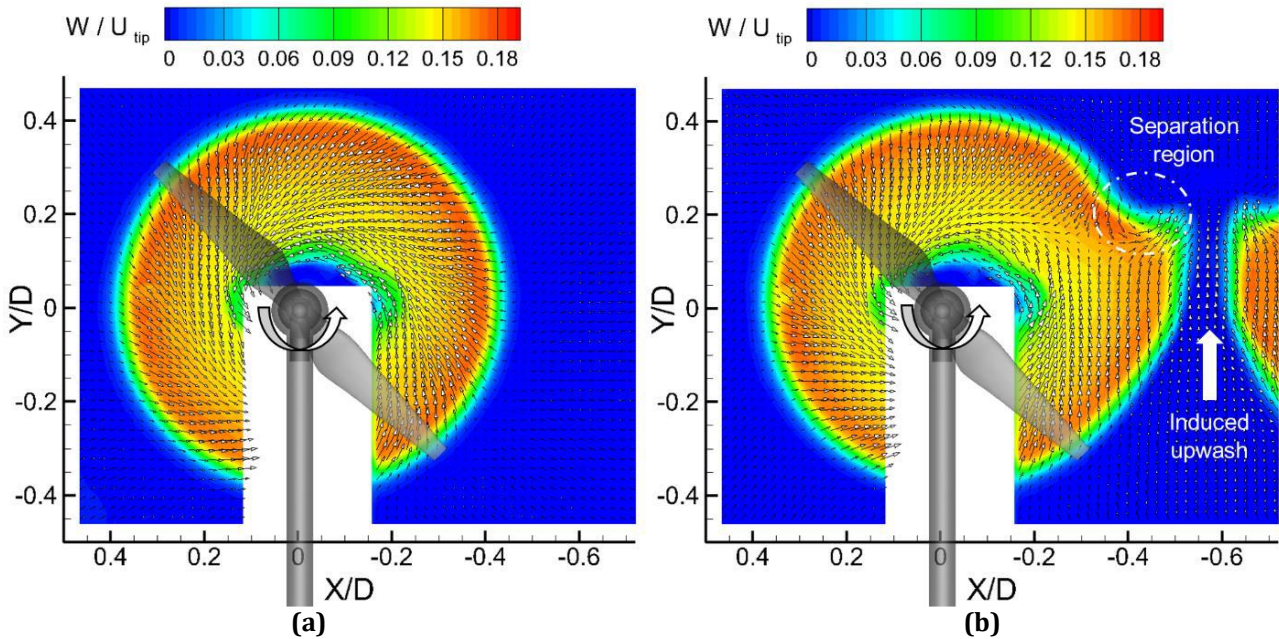


Figure 14. Velocity contours for single rotor (a) and twin rotors (b) in a cross-plane 0.1D behind the rotor plane [9]. The flow separation region is shown inside the circled area attributed to the induced upwash flow by the adjacent propeller.

The results from the numerical study of Alvarez and Ning [8] had been compared with the experimental data of Zhou, et al. [9]. Although the physical aspect of the interaction was nicely captured and the resulting performance is following the study performed by Zhou, et al. [9], this numerical approach failed to capture the recirculating region observed experimentally. The computed flow field has many similarities with the experimental results, including the tip vortices interactions, velocity contour and performance behaviour. Since the numerical results were close to the experimental ones, both in terms of performance and physical characteristics, it was concluded that the effect of the flow separation is negligible, and the origin of the performance drop is the upwash flow that interacts with the blade.

The previously presented analysis of the flow field in multi-rotor systems emphasizes the interactions occurring in hover conditions, without presenting the changes that occur during forward flight. The intensity of the flow phenomena will differ between hover and forward motion for a fixed-pitch propeller due to the different Reynolds number regimes. In forward flight, the impact in propeller performance is expected to be minor, as shown in [11], while the slipstream contraction is less than in hover. Due to the dominance of inertia forces compared to viscous ones, it is expected that the viscous phenomena due to the evolution of the tip vortices would be less severe, and thus, the subsequent interference between adjacent vortices will be less pronounced than in (near-)hover conditions.

2.3 Propeller's aeroacoustics

In this section, the fundamentals of sound are described first, presenting the formulas for the acoustic signal analysis and noise emission calculation performed in the following chapters. The principles of acoustic analogies are mentioned, subsequently presenting the Ffowcs-Williams and Hawking's equation used to calculate the noise signature in the far-field. In the last part, the aeroacoustic signature of the DP system is presented as found in the literature.

2.3.1 Fundamentals of sound

Sound is a pressure disturbance that travels through a medium as an acoustic wave, with speed c at a frequency f and wavelength λ . The wavelength and frequency of the sound wave are associated, as shown in Eq. (1.8). The speed of propagation, c , depends on the local properties of the medium but is typically about 343 m/s in the air at 20° C.

$$c = \lambda f \quad (1.8)$$

The pressure perturbation of a sound wave ($p'(t) = p(t) - p_{mean}$) follows the conservation of mass, momentum and energy equations. The sound propagation through a medium is given by the wave equation, which is formulated by coupling the conservation of mass and momentum equations [20]. In case the acoustic waves are the only source of pressure and velocity fluctuations, under isentropic flow conditions and using time-averaged flow quantities, Eq. (1.9) gives the linear formula of the acoustic wave equation.

$$\frac{1}{c^2} \frac{\partial^2 p'}{\partial t^2} - \nabla p' = 0 \quad (1.9)$$

The human ear has a wide dynamic range and can hear soundwaves within the range of 20 μ Pa to 200 Pa before encountering the threshold of pain. “The ear’s sensitivity is logarithmic, and thus the sound is measured using a decibel scale called the sound pressure level (*SPL*)” [20]. This is given in dB through the root mean square of the fluctuating pressure-time history p_{rms} and a reference pressure p_{ref} as:

$$SPL = 20 \log_{10} \left(\frac{p_{rms}}{p_{ref}} \right) \quad (1.10)$$

Where the hearing threshold of humans is $p_{ref} = 2 \times 10^{-5}$ Pa, and the root mean square of the fluctuating pressure is:

$$p_{rms} = \sqrt{\int_0^T \frac{1}{T} p'^2 dt} \quad (1.11)$$

Instead of the sound analysis into the time domain, the frequency-domain analysis shows how the signal’s energy is distributed over a range of frequencies. In order to express the acoustic pressure into the frequency domain, Fourier transformation is applied to the sound signal [21]:

$$\tilde{p}(f) = \int_{-\infty}^{\infty} p'(t) e^{-i2\pi ft} dt \quad (1.12)$$

The expression of pressure fluctuations in the frequency domain can be used to calculate the power spectral density ($P(f)$) as:

$$P(f) = \frac{|\tilde{p}(f)|^2}{T_s} \quad (1.13)$$

Where T_s is the duration of signal. Subsequently, the sound pressure value (*SPL*) within a specific band can be computed by multiplying the power spectral density with the size of the frequency band. It is expressed in dB as:

$$SPL(f) = 10 \log_{10} \left(\frac{P(f) \cdot df}{p_{ref}^2} \right) \quad (1.14)$$

Where df is the size of the specific frequency band. A frequency band is an interval in the frequency domain, delimited by a lower and upper frequency. Typical bands are the octave bands in which the frequency is doubled over the band such that the bandwidths increase with frequency. When reducing the bandwidth, 1/3rd or 1/12th octave bands are obtained. Finally, the overall sound pressure level (*OSPL*) in dB is computed by the summation of all *SPL* values at all frequencies and emission angles (θ):

$$OSPL(\theta) = 10 \log_{10} \left(\sum_i 10^{SPL(f_i, \theta)/10} \right) \quad (1.15)$$

2.3.2 Propeller noise sources

Propeller noise results from the interaction of the fluid with the rotating solid body [22]. The rotating blades emit two distinct acoustic signatures: harmonic and broadband noise (Figure 15).

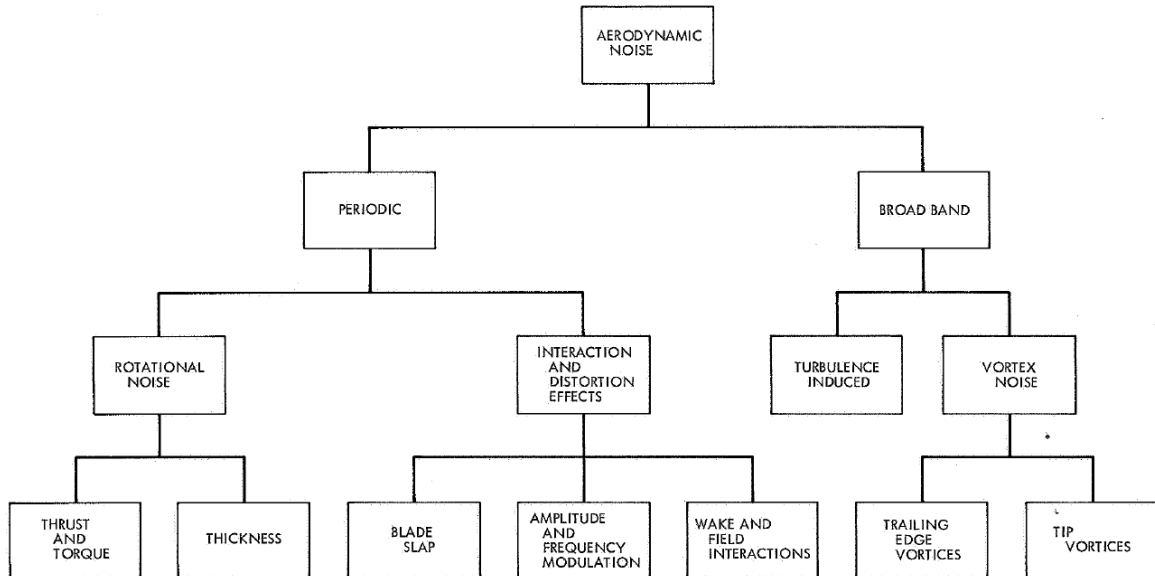


Figure 15. Aerodynamic noise sources [22].

Harmonic noise is attributed to noise sources that repeat themselves during each rotation. Such noise is the tonal noise of the propeller that is attributed to the rotational speed N of B number of blades. This pulse repeats itself in frequency BN (Figure 16). This value corresponds to the blade passing frequency (BPF), which is the first harmonic of the propeller. Typically the generated pulse is not a pure sinusoid so that many harmonics exist. These occur at integer multiples of the BPF , as shown in Figure 16b.

In the case of a uniform and non-turbulent flow, the harmonic noise in an isolated propeller is produced due to three categories of steady sources [22]: thickness, loading and quadrupole noise. Thickness noise is attributed to the periodic motion of air due to the rotation of the blade surface. Blade volume determines the amplitude of the noise, while its frequency is affected by the rotational speed [22]. Loading noise, in parallel, is a combination of thrust and torque of the propeller. Blade aerodynamics leads to a pressure distribution surrounding the blade surface that contributes to thrust and torque vectors. In flight conditions, the dominant noise component is due to loading until sonic conditions where thickness noise dominates [22]. The noise patterns of thickness and loading noise are shown in Figure 17.

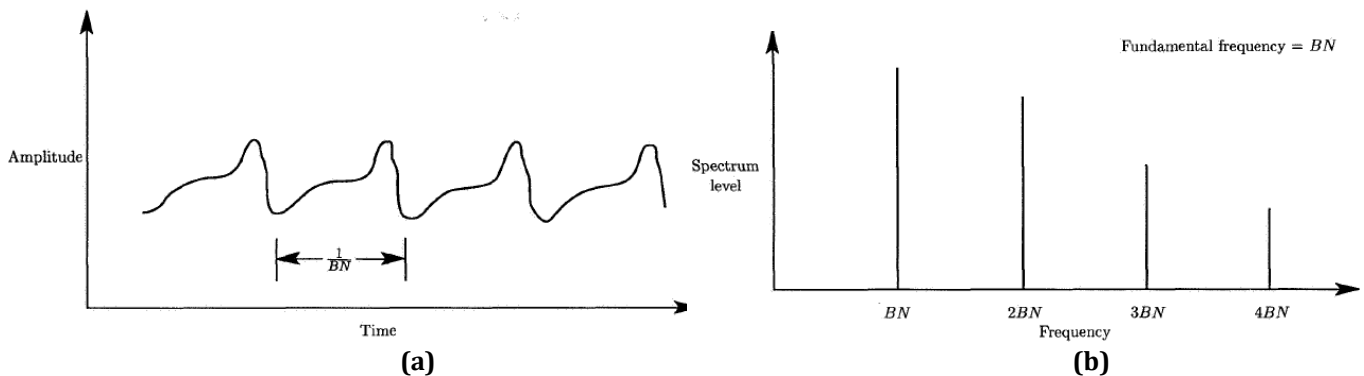


Figure 16. Harmonic noise in time spectrum (a) and frequency domain (b). Acoustic energy is distinctively distributed in specific frequencies [23].

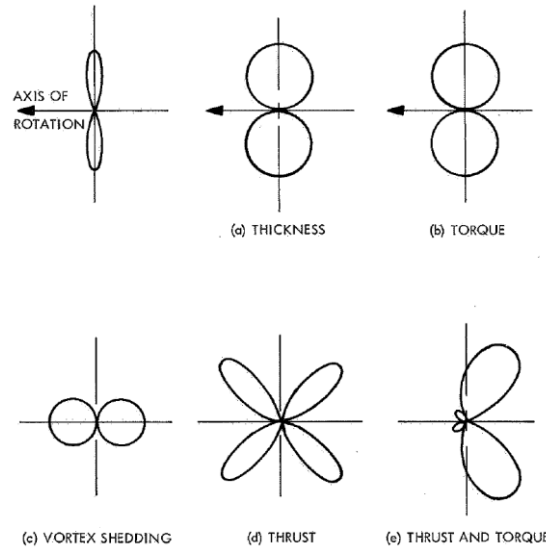


Figure 17. Theoretical noise patterns for noise sources [23].

Compared to harmonic noise, broadband noise is a random, non-periodic signal. As shown in Figure 18, the time variation plot depicts an aperiodic signal that results in a continuous line in the frequency spectrum containing pressure perturbations components at all frequencies. This type of noise is related to the vorticity shed by the blades and the turbulent phenomena that interact with the blades [23]. Vortex noise is the sound “generated by the formation and shedding of vortices in the flow past a blade” [23]. The vortex sheet shed from the propeller causes broadband noise with a direction upstream and downstream of the propeller (Figure 17). The noise level is generally lower than other noise sources, but the combination with pressure field could lead to a noticeable increase [23].

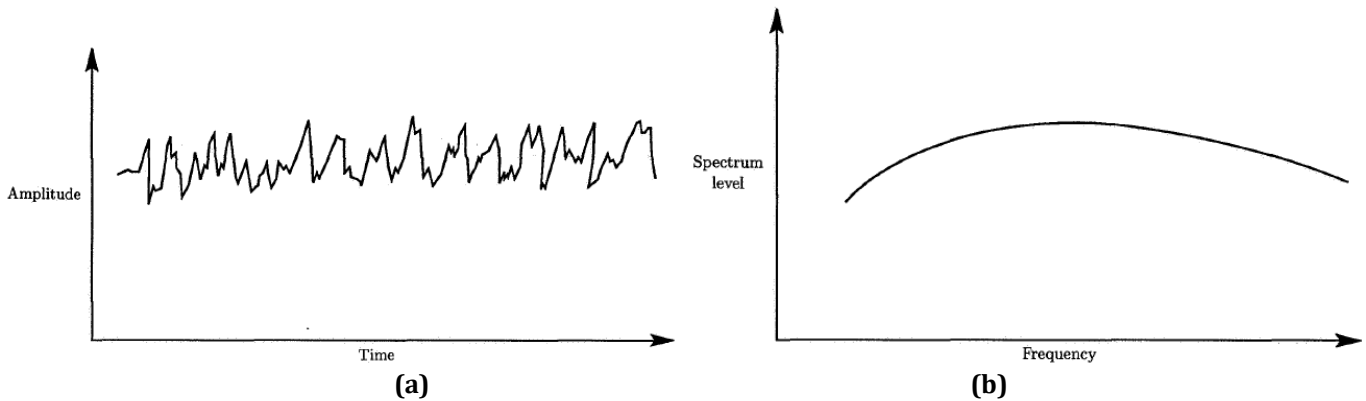


Figure 18. Broadband noise in time spectrum (a) and frequency domain (b). Acoustic energy is distributed in a range of frequencies [23].

2.3.3 Aeroacoustic analogies

Acoustic analogies aim to compute the acoustic signal in an area far away from the noise source without entirely computing the flow field in that area. They create a link between the elementary sources of sound and the sound perceived by an observer, decoupling the noise generation mechanism from its pure propagation. This is based on the accurate computation of the flow in an area, and by applying the analogy, the far-field acoustic signature can be computed. This results in a low computational cost for the simulation, as large computational domains can be avoided, and high-resolution grids can be created in the regions of interest. Acoustic analogies can be obtained by rearranging the Navier-Stokes equations and shaping the acoustic waveform, like Eq. (1.9). The most commonly used acoustic analogies are the Lighthill analogy and the Ffowcs Williams and Hawking’s analogy, which are presented below.

2.3.3.1 Lighthill analogy

In the 6th decade of the 20th century, the “Acoustic analogy” by Lighthill [24] was introduced to address the problem of sound generation by a region of high-speed turbulent flow in a quiescent flow, e.g. flow originated from a jet engine. Based on exact equations of fluid flow, Lighthill’s equations make no

assumptions relating to compressibility effects, and the equations are derived by subtracting the time derivative of the continuity equation and the divergence of the momentum equation to give:

$$\frac{\partial^2 \rho'}{\partial t^2} - c_\infty^2 \frac{\partial^2 \rho'}{\partial x_i^2} = \frac{\partial^2 T_{ij}}{\partial x_i \partial x_j} \quad (1.16)$$

$$T_{ij} = \rho V_i V_j + (p - p_\infty) - (\rho - \rho_\infty) c_\infty^2 \delta_{ij} - \sigma_{ij} \quad (1.17)$$

Where density perturbation is $\rho' = \rho - \rho_\infty = (p - p_\infty) / c_\infty^2$. The left-hand side of the Eq. (1.16) is the wave equation, and the right-hand side shows the sources terms, consisting of the Lighthill's stress tensor (T_{ij}). Lighthill stress tensor T_{ij} (Eq. (1.17)) includes terms related to momentum flux ($\rho V_i V_j$), nonlinear acoustic pressure $(p - p_\infty) - (\rho - \rho_\infty) c_\infty^2 \delta_{ij}$ and viscous effects (σ_{ij}). The significant restriction of the Lighthill analogy is that it describes the sound generation and propagation in a flow without any boundary or moving body. Curle's extension of the Lighthill analogy partially solved this issue by solving this analogy for a stationary surface. It was only until Ffowcs Williams and Hawkings in 1969 that the problem of the acoustic signature of a rotating propeller could be addressed.

2.3.3.2 Ffowcs-Williams and Hawkings analogy

The Ffowcs-Williams and Hawkings (FWH) analogy [25] further extends the analogy from Lighthill and Curle in an inhomogeneous wave equation that includes the effects of a moving body. The FWH equation is derived based on the generalised derivative concept using the Heaviside step function to rearrange the pressure and momentum terms in continuity and momentum equations. Applying similar operations with the Lighthill analogy, the FWH equation, expressed in the retarded-time τ^* (the computational time is the reception time), is given by Eq. (1.18) [25]. In the retarded-time solution of the FWH equation, the signal received by an observer consists of the summation of all disturbances that reach the observer simultaneously.

$$\begin{aligned} \rho(x, t) c_\infty^2 H_s = & \frac{\partial^2}{\partial x_i \partial x_j} \int_{V_0} \left[\frac{T_{ij}}{4\pi r (1 - M_r)} \right]_{\tau=\tau^*} dV(z) \\ & - \frac{\partial}{\partial x_i} \int_{S_0} \left[\frac{(\rho v_i (v_j - V_j) + p_{ij}) n_j}{4\pi r |1 - M_r|} \right]_{\tau=\tau^*} dS \\ & + \frac{\partial}{\partial t} \int_{S_0} \left[\frac{(\rho v_i - \rho' V_j) n_j}{4\pi r |1 - M_r|} \right]_{\tau=\tau^*} dS \end{aligned} \quad (1.18)$$

Three noise source terms are included in the FWH equation. The first term reflects the quadrupole term and depends on the Lighthill stress tensor T_{ij} , which is associated with sound radiation due to turbulent phenomena and flow distortions. The second term indicates the pressure distribution on the surface p_{ij} and the velocity differences between the flow velocity and surface velocity ($v_j - V_j$), which is represented by a dipole source. The last term is a volume displacement ρv_i source (monopole) and is dependent on the blade surface velocity $\rho' V_j$ and the density at the observer ρv_i . The numerical implementation of FWH is based on the Farassat Formulation 1A of the FWH equation [26], expressing the equation into integral form.

2.3.4 Aeroacoustic signature in multi-rotor systems

The flow interactions that occur due to the operation of propellers in close proximity affect not only the aerodynamic performance but also results in a change of the acoustic signature of the distributed-propeller system. The following section refers to the impact of the separation distance in noise emission of a multi-rotor system in hover conditions, as there is no extended analysis in the literature referring to forward flight conditions, according to the author's knowledge. The aerodynamic behaviour described above showed a change in the propeller's loading with the presence of thrust oscillations. As a result, a change in loading noise is expected, while the thrust oscillation implies a new noise source in the distributed-propeller system. In parallel, the interaction of viscous flow structure denotes a broadband noise enhancement. The loading noise is also expected to determine the noise level emission in forward-flight combined with the noise

originated by the thrust oscillations, while the contribution of the broadband component is expected to be minor due to the less pronounced viscous phenomena than in hover.

Zhou, et al. [9] examined a twin-rotor configuration's noise emission by varying the separation distance. In this study, it was observed that as the separation distance of a twin-rotor system decreases, all tonal components increase (up to 8 dB) as the noise level corresponding to the integer multiples of BPF increases. The noise level increase is evident in the area normal to the rotor plane (Figure 19). The noise emission pattern in Figure 19 is dependent on the azimuthal angle and separation distance, with a trend to increase the noise level in the direction normal to the rotor plane. As the separation distance decreases, there is a noise enhancement of 3 dB at an azimuthal position of $\beta=180^\circ$ (behind the rotor plane) for the case of separation distance $L=0.05D$ compared with the $L=1.0D$. At the same time, the noise level decreases as the azimuthal angle approach 90° , i.e. parallel to the rotor plane. The change in this angle is not as enhanced as along the propellers axis, implying that the effect of the twin-rotor system operating in close distance is minor.

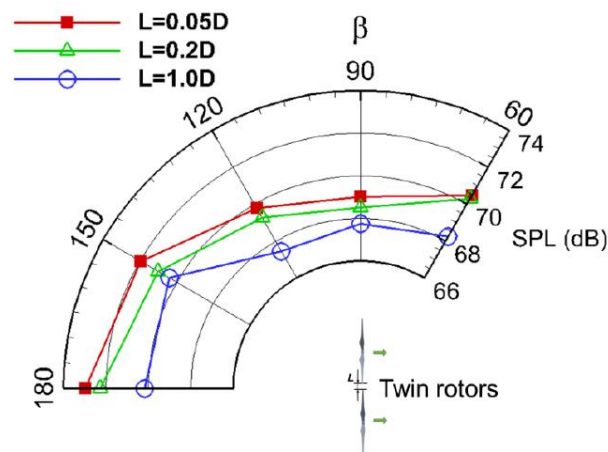


Figure 19. Measured noise level emitted around the twin-rotor system [9].

The determination of the type of noise that is the main contributor to the increase in noise level is performed using the noise spectrum in two different azimuthal positions, as shown in Figure 20. This figure depicts the sound pressure level spectrum at azimuthal angles $\beta = 180^\circ$ and $\beta = 120^\circ$ for different separation distances. Regarding the $\beta = 180^\circ$, it is observed that as the separation distance gets small, all tonal components increase. Since the tonal noise in the case of $\beta = 120^\circ$ does not present a similar increase, it is believed that the tonal noise increase, which is associated with the blade loading, is attributed to the augmentation of thrust fluctuations due to the small separation distance between the rotors. Regarding the broadband noise, it is observed that the increase of noise level for high frequencies in the case of $\beta = 120^\circ$ is more significant than the case of $\beta = 180^\circ$. This illustrates that broadband noise dominates the noise level close to the rotational plane. This behaviour is explained by the association of broadband noise with turbulent flow structures, like vortices and shear layers. The interaction of these phenomena is getting accentuated in small separation distances, and thus, their effect is significant at the sides of the rotor plane. So, the interactions of tip vortices in the twin-rotor case results in broadband noise level increase.

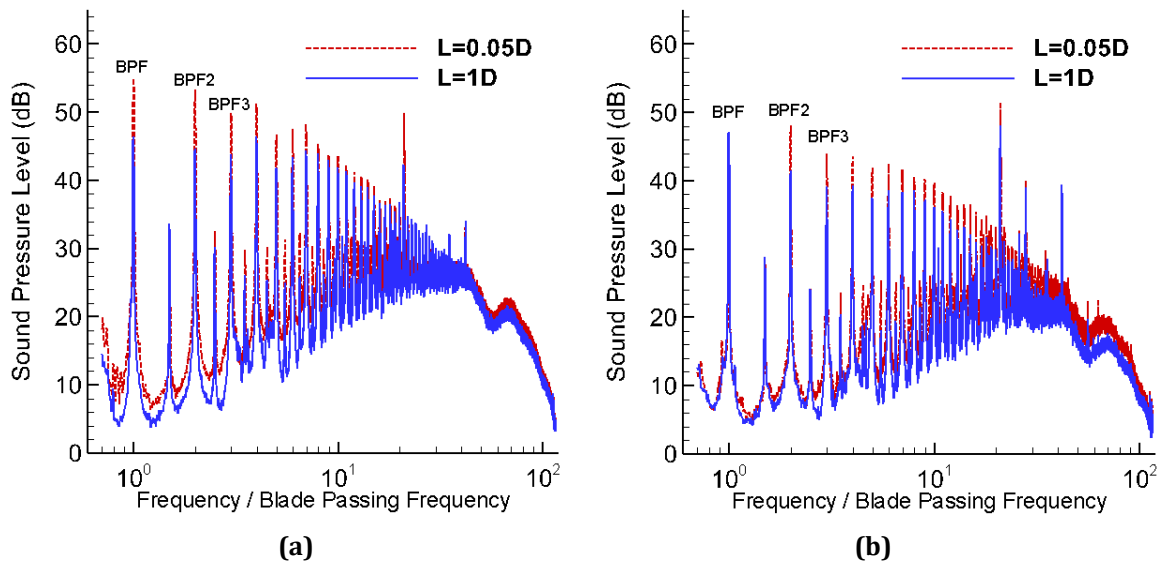


Figure 20. Sound pressure level spectrum for different separation distances at azimuthal positions of 180° (a) and 120° (b) [9].

In addition, the numerical analysis of a quadcopter UAV by Lee and Lee [10] led to similar results with Zhou, et al. [9]. In their study, there is a noise level increase in the direction normal to the rotor plane. Observing the noise emission pattern in Figure 21, it is clear that the noise pattern maintains the shape of a dipole as the separation distance between the rotors decreases. This behaviour is associated with the thrust fluctuations and, as a result, with tonal noise.

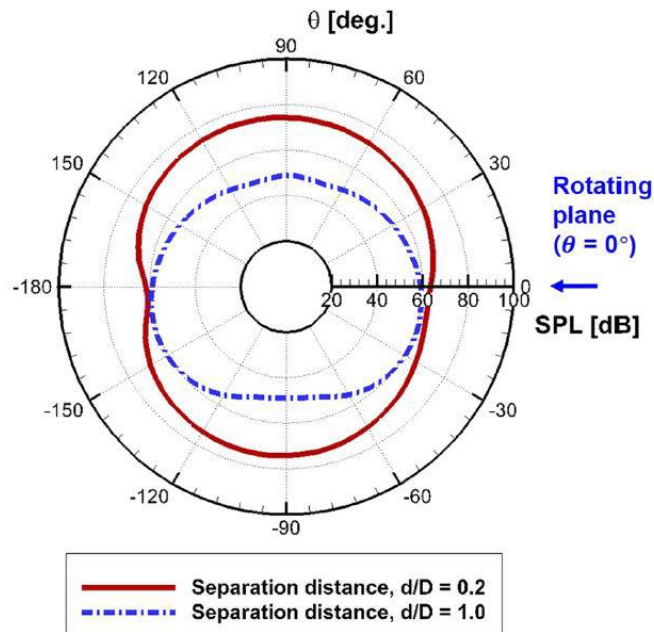


Figure 21. Overall sound pressure level emitted around the rotor plane of the quadcopter for different separation distances [10].

An attempt to positively impact the excess noise emission in a distributed-propeller system is the implementation of an active noise technique, namely phase angle control [27]. Active noise control techniques for noise level reduction are being employed to achieve noise reduction by taking advantage of the destructive interference between the noise sources. In other words, phase angle control can be used in distributed-propeller configurations where the relative angular position of a blade is controlled to achieve destructive interference. Pascioni, et al. [27] examined the potential benefit of phase control in distributed propulsion systems for noise reduction. In this study, several parameters, like propeller layout, number of propellers and rotational speed, were considered to evaluate the benefit of this technique and reduce the noise emission at specific desired regions. It was observed that the noise reduction is sensitive to the propeller layout, the number of propellers and rotational speed. The results showed that a specific propeller

layout could steer away most of the noise emission from a region of interest. Thus, the overall directivity of the blade passage frequency noise can be modified, steering these tonal components away from specific areas. The ideal benefit of phase control could reach up to 24 dB reduction of the BPF in a specific region on the ground in a layout with 4 propellers. However, limitations of this technique are related to the real operational conditions (non-uniform flow conditions, wind gusts etc) and could result into a reduction up to 6 dB of the BPF. Another limitation of this analysis is that sources of unsteady noise, like the interactional effects between the propellers operating at close distances, were neglected. Therefore, an in-depth analysis of the relative phase angle effects is required to assess the aerodynamic impact and examine a potential benefit in noise emission of a distributed-propeller system.

3

Methodology

This chapter presents the methodology that was adopted to perform the numerical simulation. The Lattice Boltzmann solver is presented at first, mentioning the algorithm that is followed to solve the lattice Boltzmann equation combined with the turbulence modelling, the wall functions and the aeroacoustics formulations. Subsequently, the computational setup of the numerical models is described, followed by the boundary and initial conditions. The final section of this chapter presents the measuring data during the simulation with their sampling rates.

3.1 Flow solver

The Lattice Boltzmann method (LBM) has been developed as an alternative to conventional Navier Stokes Computational Fluid Dynamics (NS-CFD) methods. The basis of conventional numerical schemes is the macroscopic continuum equations that can be solved using various differentiation schemes, like finite elements or finite volumes. On the contrary, the formulation of LBM is based on the averaged microscopic movement of particles. The theoretical foundation for using simplified kinetic models is based upon the observation that natural macroscopic phenomena are “insensitive to the underlying details of microscopic, or even mesoscopic, dynamics”[28]. Thus, the LBM determines the macroscopic flow variables based on the kinetic equations in the mesoscopic domain[28, 29].

An LBM is selected for the present study as it has already been validated in cases related to aerodynamic and aeroacoustics simulations of rotors [30-32]. In addition, an LBM is suitable for time-dependent cases and is amenable to high-performance computing on parallel architectures [28]. The commercial software package 3DS-Simulia PowerFLOW 6.0a is used in the present analysis.

3.1.1 Lattice Boltzmann method

The LBM, as an extension of the lattice gas models [28], tracks the distribution of gas particles located in a lattice. The LBM solves the discrete Lattice Boltzmann equation by introducing the particle distribution function $f(\mathbf{x}, t)$, representing the density of particles with velocity $\mathbf{c}_i = (c_{ix}, c_{iy}, c_{iz})$ at a position \mathbf{x} in time t . The points \mathbf{x} at which $f(\mathbf{x}, t)$ is defined are located as a lattice in space, with spacing Δx at specific times t , separated by a time step Δt . A lattice is used to determine the motion of the gas to discrete nodes with discrete velocities in specific directions.

The discretization of the velocities is such that it enables a set of particles to move exactly from one node to a neighbouring one within one-time step [28]. The discrete velocities combined with the weighting factors w_i form a velocity set $\{\mathbf{c}_i, w_i\}$. These velocity sets determine the number of the discrete velocity. The notation of these sets is DdQq, where d is the number of spatial dimensions the velocity set covers and q is the set's number of discrete velocities. A high number of discrete velocities generally results in high accuracy at a high computational cost. The velocity sets D1Q3 and D2Q9 are shown for 1D and 2D simulations in Figure 22. In the 1D simulation, the particles are allowed to move along the X-axis (left or right) or stay at rest (Figure 22a). Similarly, the particle for a 2D simulation (Figure 22b) has 8 different

directions of motion or remain at rest. In the present study, 19 discrete velocities are used in a 3D domain (D3Q19 –Figure 23). The discrete velocities are defined as $c_i(\mathbf{x}, t)$, with i ranging from 0 to 18. Note that one of the velocities is the resting velocity which is equal to $c_{i=0}=0$. The distribution function can now be discretised using the discrete velocities $c_i(\mathbf{x}, t)$ and becomes $f_i(\mathbf{x}, t)$.

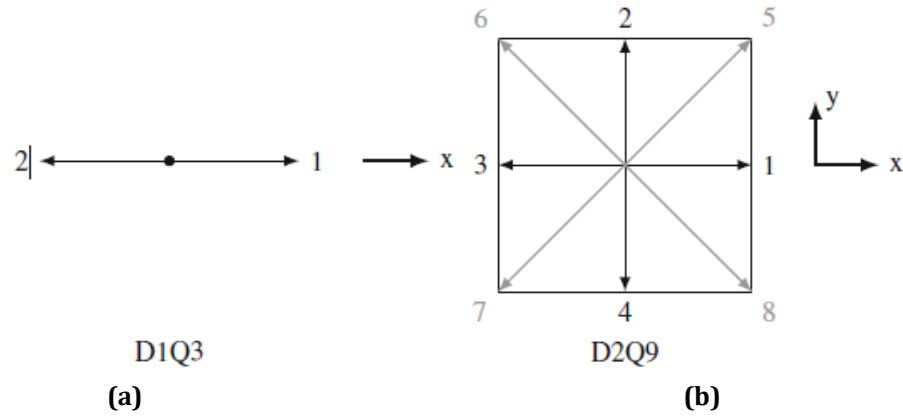


Figure 22. D1Q3 (a) and D2Q9 (b) velocity sets. Velocities with length $|c_i|=1$ and $\sqrt{2}$ are shown in black and grey, respectively. Rest velocity vectors $c_{i=0}=0$ are not shown [28].

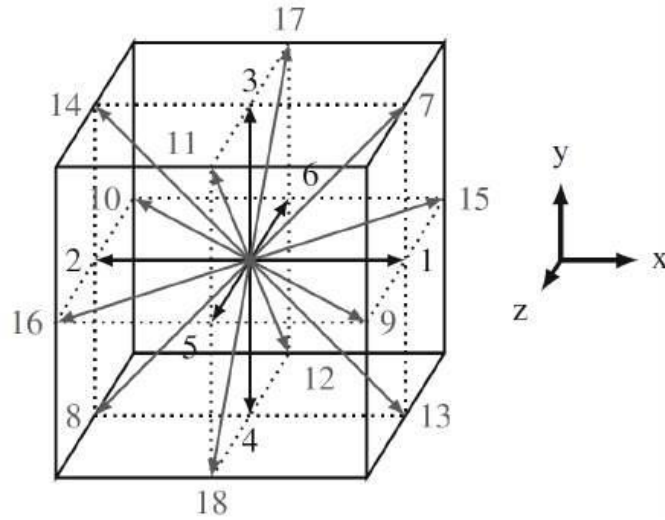


Figure 23. D3Q19 velocity set with 19 discrete velocities to neighbouring nodes [28]. Properties of the velocity set are given in Table 1.

The lattice Boltzmann equation is the discrete expression of the Boltzmann equation in space and time. Its formulation is given as:

$$f_i(x + c_i \Delta t, t + \Delta t) = f_i(x, t) + \Omega_i(x, t) \quad (1.19)$$

Where $f_i(\mathbf{x}, t)$ is the discrete velocity distribution function, c_i is the velocity that refers to the distribution function and $\Omega_i(\mathbf{x}, t)$ is the collision operator. This formulation illustrates the way that particles move with velocity c_i to an adjacent node (located in $\mathbf{x} + c_i \Delta t$) in the time step $t + \Delta t$. This operation represents the particles streaming from one node to a neighbouring one. Simultaneously, a collision operator $\Omega_i(\mathbf{x}, t)$ models the particle collisions by redistributing particles at each node. In the present analysis, the Bhatnagar-Gross-Krook (BGK) model is used due to its simplicity, as shown in Eq. (1.20).

$$\Omega_i = - \frac{f_i(x, t) - f_i^{eq}(x, t)}{\tau} \Delta t \quad (1.20)$$

The BGK model leads to the relaxation of the population in an equilibrium state f_i^{eq} at a rate determined by the relaxation time τ . The relaxation time directly affects the transport properties of the particles, like the viscosity ν . Regarding the equilibrium state, it is reached when a gas is not affected by any external force for a sufficiently long period. Therefore, in a force-free, homogeneous and steady

environment, the solution of the Boltzmann equation becomes the equilibrium distribution f_i^{eq} . In macroscopic quantities, the equilibrium state is expressed as:

$$f_i^{eq}(\rho, \mathbf{u}, T, \boldsymbol{\zeta}) = \frac{\rho}{(2\pi RT)^{d/2}} e^{-\frac{(\boldsymbol{\zeta}-\mathbf{u})^2}{2RT}} \quad (1.21)$$

Where ρ is the fluid density, \mathbf{u} is the fluid velocity, T is the temperature, $\boldsymbol{\zeta}$ is the velocity of density particles, d is the number of spatial dimensions, and R is the gas constant. A discrete approximation of equilibrium distribution f_i^{eq} is achieved by implementing a Hermite series expansion into a non-dimensionalized expression of equilibrium distribution. In order to reproduce the physics and satisfy the conservations law, the first three terms of the series expansion are sufficient to represent the hydrodynamics. This also serves the need for low numerical cost. So, for a low Mach number flow, the equilibrium distribution state can be approximated by:

$$f_i^{eq} = w_i \rho \left(1 + \frac{\mathbf{u} \cdot \mathbf{c}_i}{c_s} + \frac{(\mathbf{u} \cdot \mathbf{c}_i)^2}{2c_s^4} - \frac{\mathbf{u} \cdot \mathbf{u}}{2c_s^2} \right) \quad (1.22)$$

Where the weight coefficients w_i are specific to the chosen velocity set and are shown in Table 1. Fluid density is denoted as ρ , \mathbf{u} is the fluid velocity and \mathbf{c}_i is the discrete velocity that refers to the distribution function. The speed of sound for the various velocity sets is defined as:

$$c_s^2 = \frac{1}{3} \frac{\Delta x^2}{\Delta t^2} \quad (1.23)$$

Table 1. Properties of the D3Q19 velocity sets. The speed of sound for all of these velocity sets is c_s .

Velocities	Number	Length c_i	Weight w_i
$(0,0,0)$	1	0	1/3
$(1,0,0), (0,1,0), (0,0,1)$	6	1	1/18
$(1,1,0), (1,0,1), (0,1,1)$	12	$\sqrt{2}$	1/36

The macroscopic flow quantities of density and velocity are obtained by the discrete integration of the microscopic quantities weighted by the distribution function over the state space. The state of equilibrium determines that particles distributions f_i are equal to the respective equilibrium ones f_i^{eq} , as shown in Eq. (1.24) and (1.25).

Mass density:

$$\rho(\mathbf{x}, t) = \sum_i f_i(\mathbf{x}, t) = \sum_i f_i^{eq}(\mathbf{x}, t) \quad (1.24)$$

Momentum density:

$$\rho \mathbf{u}(\mathbf{x}, t) = \sum_i \mathbf{c}_i f_i(\mathbf{x}, t) = \sum_i \mathbf{c}_i f_i^{eq}(\mathbf{x}, t) \quad (1.25)$$

Where $f_i(\mathbf{x}, t)$ is the discrete-velocity distribution function, f_i^{eq} is the equilibrium distribution, and $\mathbf{c}_i(\mathbf{x}, t)$ is the discrete velocity at position \mathbf{x} and time t .

3.1.1.1 Algorithm

The algorithm of the LBM solver, as described in Figure 24, incorporates three main step: Initialization, Collision and Propagation.

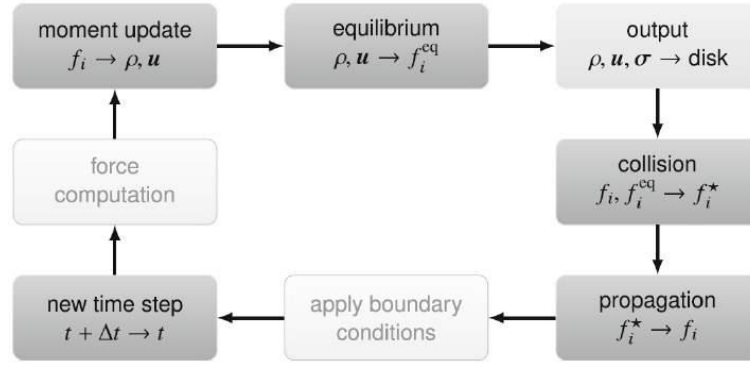


Figure 24. Overview of one cycle of the LBM algorithm [28].

The first process of the LBM algorithm is the initialisation that sets the equilibrium population, depending on whether it is a steady-state or an unsteady case. The algorithm is briefly presented below:

- Computation of fluid density (ρ) and velocity ($\mathbf{u}(\mathbf{x}, t)$) via Eq. (1.24) and (1.25).
- Computation of equilibrium distribution f_{eq} via Eq. (1.22) that can be used in the BGK operator.
- Subsequently, collision operation would result in post-collision distribution f^* . The post-collision distribution is given by:

$$f_i^* = f_i \left(1 - \frac{\Delta t}{\tau} \right) + f_i^{eq} \frac{\Delta t}{\tau} \quad (1.26)$$

- Then, propagation operation is performed to compute the distribution on neighbouring nodes via:

$$f_i(x + c_i \Delta t, t + \Delta t) = f_i^*(x, t) \quad (1.27)$$

- The propagation is applied on the boundaries.
- The final step before the return to step 1 is the increase of time step by Δt .

3.1.1.2 Turbulence modelling

Turbulence models are mathematical formulas that predict the effects of turbulence without calculating the exact flow field. In high Reynolds cases, the direct calculation of all flow scales would require excessive-resolution leading to a rapid increase in computational cost. Thus, turbulence models are implemented to approximate the unresolved scales of motion. The flow and energy cascade, in Figure 25, shows that the largest (integral) scales are transferred to medium-small scale vortices (inertial subrange) and, then, are dissipated in microscale vortices (dissipative scales). The large-scale vortices are induced by the geometry and boundary conditions of the flow, while the small scales obtain their energy from the large ones through an energy cascade [33]. The small scales are dissipative, contain low energy, and are easier to be modelled than the high energy scales. So, implementing a Large Eddy Simulation (LES) analysis will simulate the large eddies while modelling the effect of the small ones (Figure 25). Similarly, the LBM can compute the turbulence for various Reynolds number regimes [34], but for turbulent flows with high Reynolds number ($>100,000$), it is not feasible to resolve all scales. So, the method used in PowerFLOW is the very large eddy simulation (VLES).

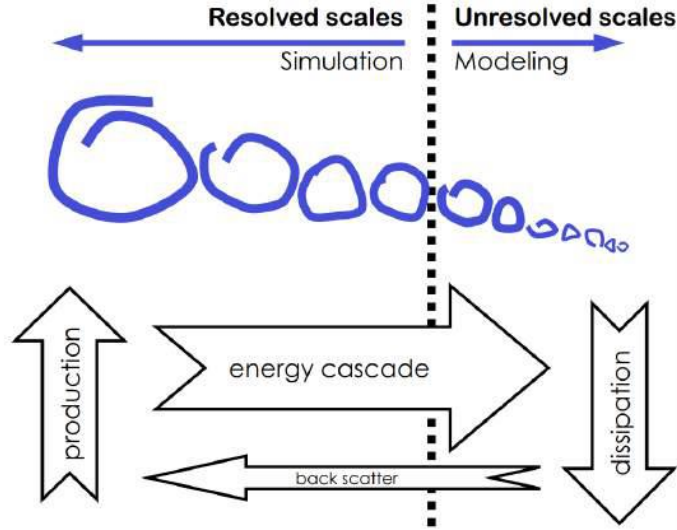


Figure 25. Simulated and modelled turbulence scales, including energy flow [35].

A very large eddy simulation (VLES) model is used to consider the effect of the sub-grid unresolved scales of turbulence. A two-equation $k-\varepsilon$ renormalization group is used to compute a turbulent relaxation time that is added to the viscous relaxation time [36]:

$$\tau_{eff} = \tau + C_{\mu} \frac{k^2 / \varepsilon}{(1 + \eta^2)^{1/2}} \quad (1.28)$$

With k the turbulent kinetic energy, ε the turbulent dissipation rate, $C_{\mu} = 0.09$ and η depending on factors such as the local strain and vorticity [30]. The term η is used to mitigate the sub-grid scale viscosity for resolving large vortical structures. The dimensionless kinematic viscosity ν is related to the relaxation time following:

$$\nu = c_s^2 \left(\tau - \frac{\Delta t}{2} \right) \quad (1.29)$$

3.1.1.3 Wall model

Wall models are implemented to represent the flow regions near walls and compute the pressure gradient effects. Instead of using an extremely fine mesh to resolve the flow in that areas accurately, coarse computational grids can be used, reducing at the same time the computational cost. The basis of the pressure gradient wall model (PGE-WM) is the generalized law-of-the-wall model [37]. The expression of the pressure gradient model is:

$$u^+ = \frac{1}{\kappa} \ln \left(\frac{y^+}{A} \right) + B \quad (1.30)$$

Where $B=5.0$ and $\kappa=0.41$ are constants and y^+ and u^+ are non-dimensional wall distances and velocity, respectively, given by the formulas:

$$\begin{aligned} y^+ &= \frac{u_{\tau} y}{\nu} \\ u^+ &= \frac{u}{u_{\tau}} \end{aligned} \quad (1.31)$$

Where u_{τ} is the friction velocity, y is the wall distance, and u is the flow velocity near the wall. Parameter A is a function of the streamwise pressure gradient given by the expression below. Due to the pressure gradient, the flow is slowing down and expanding.

$$A = 1 + \frac{f \left| \frac{dp}{ds} \right|}{\tau_w}, \hat{\mathbf{u}}_s \cdot \frac{dp}{ds} > 0 \quad (1.32)$$

$$A = 1, \text{ otherwise}$$

Where τ_w is the wall shear stress and dp/ds is the pressure gradient along the streamwise direction, $\hat{\mathbf{u}}_s$ is the unit vector of the local flow. Parameter f is the length scale of the unresolved scale near-wall region. There is an iterative process to solve these equations close to the wall surface based on the bounce-back scheme to compute the turbulence model's boundary conditions [34].

3.1.1.4 Grid discretization

Computational grid discretization is used to divide the continuous space into discrete topological and geometrical cells to be used by the flow solver. In PowerFLOW, the flow domain is discretized into lattice elements. The lattice is composed of voxels, which are 3D cells. Voxels are the basic volume elements on which the particles move from one voxel to another at each time step. The lattice also includes surfels, which are surface elements that occur where the surface of a body intersects the fluid. The view of a 2D lattice is shown in Figure 26.

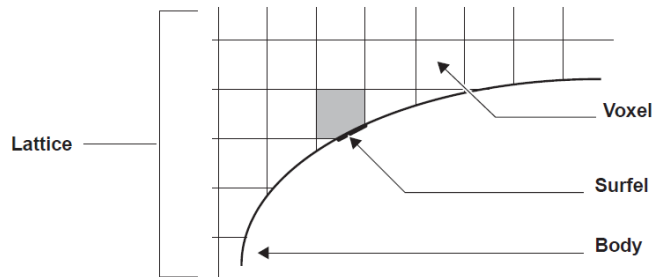


Figure 26. Lattice elements in 2D view in PowerFLOW [38].

As will also be presented in the following sections, PowerFLOW allows for areas in the computational grid with variable resolution (VR). The different levels of resolutions within the simulation volume enable resolving in detail the flow features and reducing the overall number of voxels. Thus, the region of highest resolution is placed in the areas of greatest interest, and simultaneously, the required total number of voxels is kept relatively small while the computational time is substantially decreased [38]. The simulation volume is based on the number of fine equivalent voxels. This number is computed based on the number of voxels at different resolution levels and the number of different grid levels, as given by:

$$\begin{aligned} \text{Fine equivalent voxels} &= N(\text{finest scale}) + N(2^{\text{nd}} \text{ finest scale})/2 \\ &+ N(3^{\text{rd}} \text{ finest scale})/4 + \dots \\ &+ N(\text{coarsest scale})/2^{\text{grid level}-1} \end{aligned} \quad (1.33)$$

Where N is the total number of voxels in a specific VR region. The number of fine equivalent voxels is used to distinguish the different resolution levels, as will be discussed in the next chapter.

3.1.2 Computational aeroacoustics

PowerACOUSTICS is the tool of PowerFLOW that is used for computing the far-field noise from components due to external pressure fluctuations. The far-field analysis module uses near-field PowerFLOW results as input to an acoustic analogy solver based on the Ffowcs Williams–Hawkings (FWH) equation [38]. Estimating the acoustic signature in the far-field would require a large domain with regions of high resolution that will enable the acoustic signal to travel in the far-field. In order to identify the acoustic signal, 12 voxels per wavelength or more [39] are required. This would result in a domain with an excessive number of voxels heavily affecting the computational cost. Therefore, the FWH analogy is implemented to compute the near-field pressure fluctuations and predict the far-field sound in a less computationally expensive

approach than direct calculation. The analogy is based on an inhomogeneous wave equation, the Ffowcs-Williams Hawkins equation, including terms of the homogeneous wave equation and the propeller's noise source term, as explained in Section 2.3.3.2.

The actual implementation of the FWH analogy is based on the formulation used to sample pressure data. Pressure data are saved on surfaces in PowerFLOW, both solid ones and permeable surfaces as described below:

- **Solid surface (FW-H Solid):** In this formulation, a physical surface of a body is used as the sampling area of the data. The integration of pressure values is computed over this physical surface of the body, reducing the computational cost of the solution as the solution of the volume integrals is avoided. Thus, the solid surface formulation confines all the flow non-linearity in a volume integral over a domain exterior to the body. In the case of a propeller, the solid formulation on the blade surface accounts only for the noise sources related to pressure fluctuations on the surfaces, i.e. loading and thickness source terms, neglecting the quadrupole term outside of the blade surfaces. In PowerFLOW, only pressure values are required to perform the FWH analogy using solid formulation.
- **Permeable surface (FW-H Permeable):** The surface used in this formulation to sample the required data covers an area that includes the physical bodies and the surrounding flow. The pressure field's integration is now performed over this control surface instead of the body surface as in the FW-H Solid. All terms defined in the FWH analogy (Eq. (1.18)) are considered, i.e. loading, thickness and quadrupole terms. Thus, the permeable surface extends to a larger region than the solid surface, increasing the computational cost. Another aspect of the permeable formulation is related to hydrodynamic fluctuations and turbulent structures. Due to the turbulent travelling structures and hydrodynamic fluctuations, interactions could alter the pressure data sampled on the surface. As a result, it is suggested that the permeable surface be positioned in a linear flow region. To implement the FW-H permeable analogy, PowerFLOW requires that the variables of pressure, velocity components and density be sampled on the control surface.

PowerFLOW applies the advanced-time solution of the FWH analogy. In this approach, the computational time is the emission time, and it is based on a retarded time approach, but the point of view is the source. This means that “at each computational time and for each source element, the time at which the corresponding disturbance will reach the observer is calculated and referred to as advanced time” [40]. Significant advantages of the advance-time approach are the employment in parallel architectures, leading to small computational cost, while non-iterative solutions of the retarded time equation are required [40].

3.2 Computational setup

This section presents the computational setup of the three computational models. The discretization of the isolated-propeller case and the distributed-propeller system is presented, accompanied by the flow and boundary conditions.

3.2.1 Propeller geometry

The propeller, known as the “XPROP-S” propellers [11], features six blades and a diameter of 0.2032 m. The distribution of chord and twist angle is shown in Figure 27b. The root chord length of the blades is 16 mm with a pitch angle equal to 30° at 70% of the radius. The propeller's hub has an elliptic shape with a diameter equal to 0.084 m. For the case of distributed propellers, three identical propellers will be used distributed along the Y-axis, with separation distance, i.e. the distance between two adjacent blade tips, 2% of the diameter (0.004 m), as shown in Figure 28a. There is no relative phase angle between the adjacent propellers in this model. On the contrary, the effects of the relative phase angle between the propellers (Figure 28b) is examined in a different model, where Propeller#1 is rotated by $\Delta\varphi=20^\circ$ clockwise with the separation distance between the propellers remaining the same. The direction of rotation is counter-clockwise, as illustrated by the arrows in Figure 28.

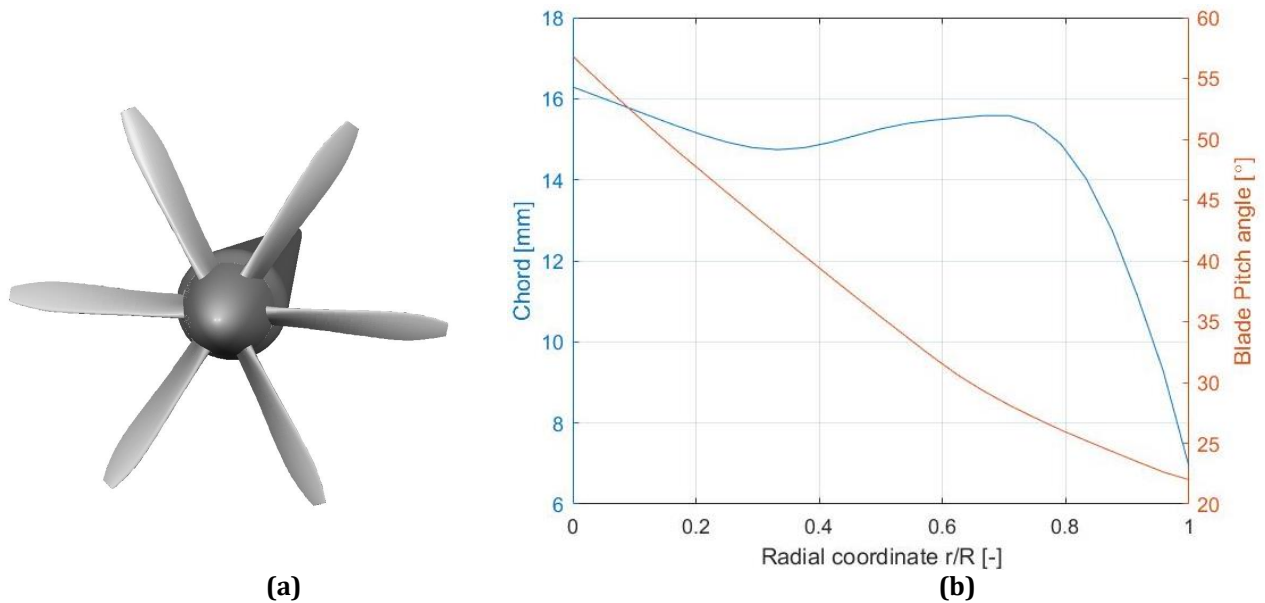


Figure 27. Propeller model (a) with its chord length and blade pitch angle distributions (b).

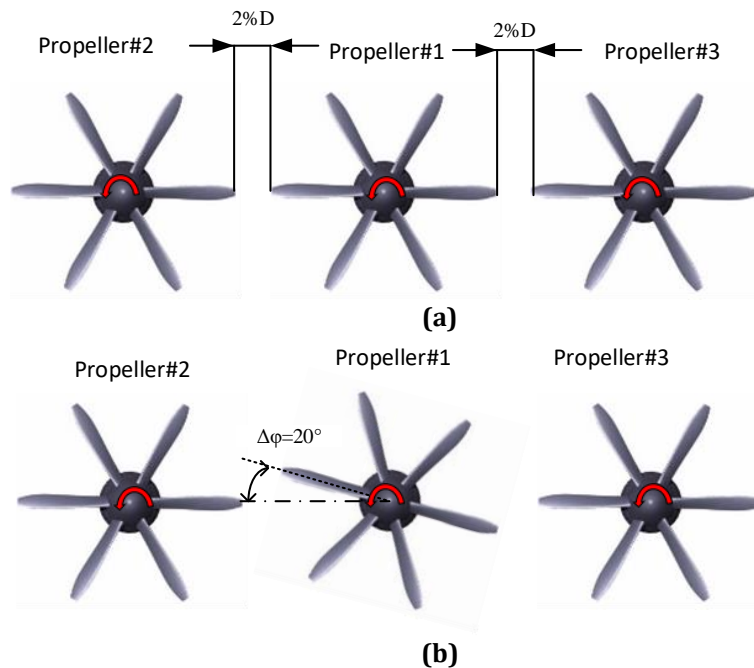


Figure 28. Distributed-propeller system (a) with the separation distance between blade tips equal to $2\%D$ ($0.004m$). The red arrows show the direction of rotation. The DP case with a relative phase angle $\Delta\phi=20^{\circ}$ is shown in figure (b).

3.2.2 Isolated-propeller case setup

The setup of the simulation starts with the definition of the flow domain. In both isolated-propeller and distributed-propeller cases, the flow domain is defined as a rectangle with length, width and height related to the diameter of the propeller (D): $[L, W, H]=[120D, 120D, 120D]$ as shown in Figure 29. The selection of the flow domain's size is essential to simulate the flow conditions realistically. A relatively large domain was selected to avoid undesired effects due to potential reflections from the boundaries. The origin of the Cartesian coordinate system is defined by the intersection of the propeller axis with the propeller plane. The flow domain is separated into rectangular regions with different resolutions (variable resolutions (VR)). The initial model of the isolated propeller is defined with 12 VR regions, as shown in Figure 29. The region of highest resolution is defined near the blade's surfaces. In this VR area, the voxel size is defined as the blade's root chord length ratio to the resolution level. The resolution increases with a factor of two from one VR region to the next (moving towards the boundaries), enabling fine mesh in the area of interest and coarse mesh near the boundaries. A volume of revolution is generated containing the propeller and spinner with a

clearance distance equal to 10% of the diameter. This value has been selected to avoid errors caused by the boundary rings of the volume crossing more than two regions of variable resolution. The rotating sliding-mesh (local reference frame) is defined for this volume with an angular velocity $n=148.8$ rps. This value corresponds to the propeller's high thrust setting in forward flight with an advance ratio of $J = 1$ and free-stream velocity of 30.23 m/s. The nacelle of the model has been extended to the outlet boundary to avoid including additional interaction mechanisms.

Figure 29a illustrates the existence of an acoustic sponge around the propeller. The aim of this feature is to dissipate potential reflections of the boundaries that could reach the region of interest and negatively affect the acoustic signal. Its implementation is based on varying the kinematic viscosity per unit temperature from $0.005 \text{ m}^2/(\text{sK})$ close to the geometry to $0.5 \text{ m}^2/(\text{sK})$ in the far-field. As shown in Figure 29a, two spherical regions define the area of viscosity transition, with the inner radius equal to $5.5D$ and the outer radius equal to $7D$ from the centre of the coordinate system.

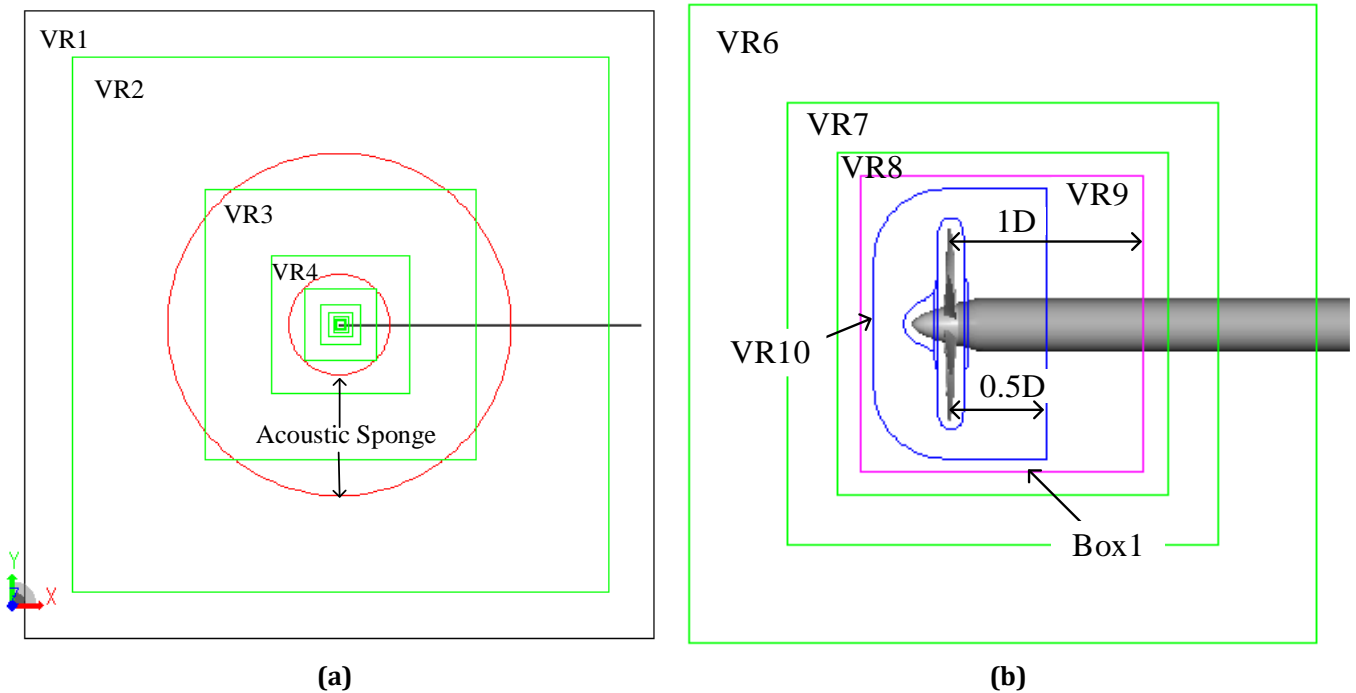


Figure 29. Flow domain and variable resolutions (VR) regions in the far-field (a). The acoustic sponge is indicated with red notation. Visualization of the VR regions around the propeller's surface (b). The rotating volume is indicated with blue colour around the blades and the spinner.

Close to the propeller, VR10 is defined as depicted with blue colour in Figure 29. This high-resolution region starts upstream of the spinner at a distance equal to 20% of the diameter and reaches half of the propeller's diameter in the downstream direction. Further outboard, "Box1" is defined as a rectangle, coloured purple in Figure 29b. This region starts upstream of the VR10 with an offset distance equal to 20 voxels, and it is extended up to one diameter downstream. This volume is used to save the mean and instantaneous flow data. In the outer regions of "Box1", each rectangle is defined as an offset from the previous one containing a fixed number of voxels (20).

The two VR regions around the blades are shown in Figure 30. The region with the highest resolution (VR12) is defined around the blades with an offset distance of 15 voxels. Region VR11 is defined around the blade surfaces as a second offset region to capture the blades surface fully, with an offset distance equal to 15 voxels from the VR12.

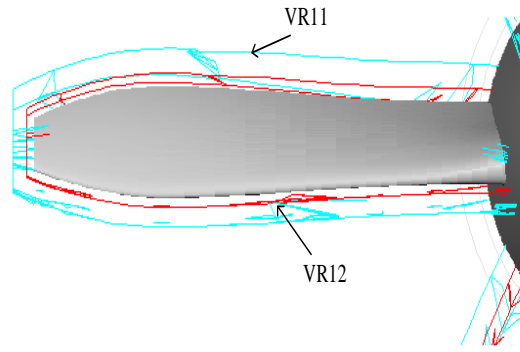


Figure 30. Visualization of VR11 and VR12 areas around a blade of the propeller.

3.2.3 Distributed-propeller case setup

In the case with the three propellers, similar discretization has been performed considering the small separation distance. Overall, 13 regions of variable resolutions (VR) have been defined, starting from the low-resolution areas near the boundaries and reaching the high-resolution region near the blades. The resolution increases with a factor of two, similarly to the isolated-propeller model, enabling the grid generation with an increased level of accuracy in the regions of interest, like between the propellers and at propellers surfaces. As a result, the total number of voxels in the domain is not excessively raised, keeping the computational cost of the simulation low.

The highest-resolution area of the domain is VR13, defined around the blade surface and the spinner, as depicted in Figure 33. This region includes 15 layers of voxels, similarly to the isolated-propeller case. This region plays a major role in the flow around the blades, affecting the boundary layer calculation and the tip vortices. The small distance between the three propellers poses a constraint for the rotating volumes of the propellers. Since the distinguished rotating volume cannot cross each other, proper selections are made in the setup to ensure a relatively large rotating domain, as shown in Figure 31. Thus, the clearance distance of the rotating volumes is selected as 0.019 of the diameter, excluding the rotating areas of the adjacent propellers.

Outboard of the rotating volumes VR12 is defined as depicted in Figure 31 and Figure 32 with light blue colour. It is defined as an offset of the rotating volumes containing 20 voxel layers. This region encloses all rotating volumes and the area between the propellers. The latter plays a major role in the analysis of this system, as the interference between the flow structures should be nicely computed. In this area, the tip vortices of adjacent propellers will start to interact when two neighbouring blades pass through. Therefore, the region between the adjacent propellers should incorporate an adequate number of voxels to capture the flow phenomena accurately. In principle, an adequate number of voxels should be greater than 8. For resolution =150 voxels/ c_r , the grid view in Figure 34 shows an adequate number of voxels at the area between the propellers.

Downstream of the propellers, VR11 covers the near-field slipstream of all three propellers. VR11 has circular arcs on the left and right sides (see the front view in Figure 31 denoted with red colour), and straight lines connect these arcs. This shape is extruded downstream with a length equal to half of the diameter. Further outboard, VR10 is a rectangular area called “Box1” containing all these features. “Box1” is located 0.368D upstream of the propellers and is extended up to one diameter behind them, as shown in Figure 31 and Figure 32. Its location allows for an adequate number of voxels (>20) to be placed, while its length is based on the literature. The description of the slipstream evolution for the three propellers can reveal the potential wake interference by visualising the tip vortices motion. “Box1” is also used for sampling the flow data both for the mean flow and instantaneous data. Subsequently, additional rectangular areas are defined as offsets of “Box1” (Figure 31 and Figure 32), dividing the far-field into different resolution areas, i.e. VR9, VR8. Each rectangular area contains 15 voxels. Simultaneously, the different resolution regions contain enough voxels for the acoustic waves to travel without reflections and spurious noise that can be induced due to undesired discretization. An acoustic sponge has also been located in the region between 18D and 34D from the coordinate system centre (Figure 32).

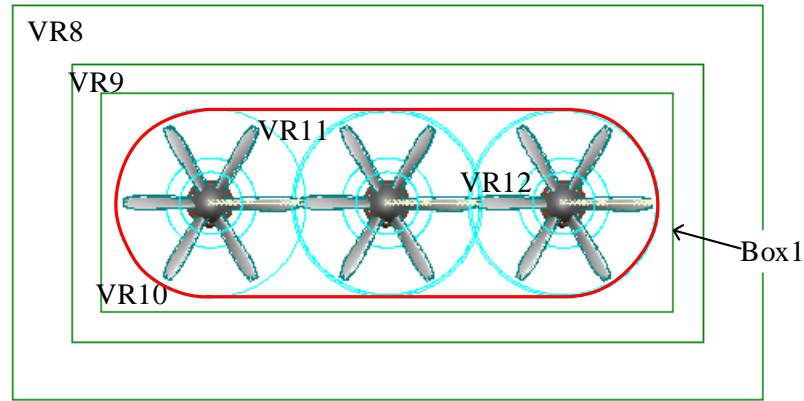


Figure 31. Visualization of the VR regions in the near-field of the three-propeller model (front view).

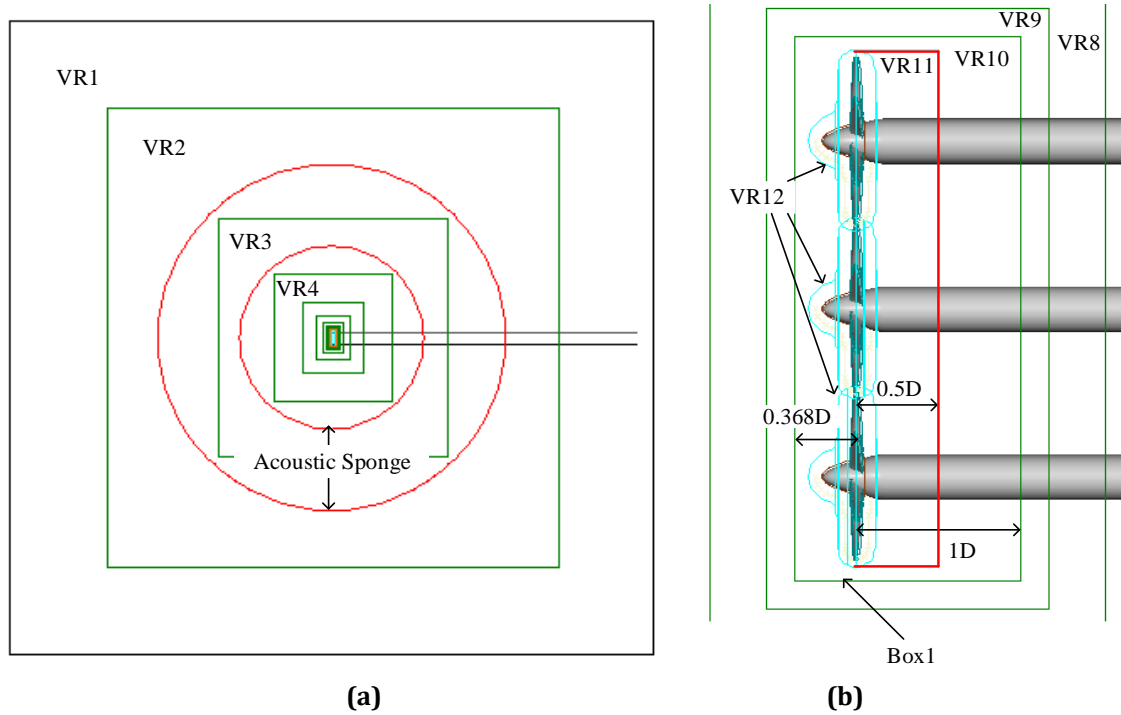


Figure 32. Visualization of the VR regions in the far-field (a) and near-field (b) of the three-propeller model (side view). "Box1" is indicated alongside the near-field of the slipstream (VR11-red coloured) and the outer discretized rectangular areas, i.e. VR10, VR9 and VR8.

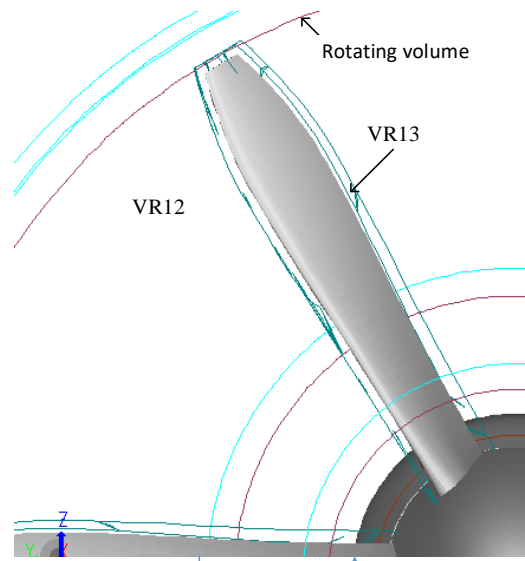


Figure 33. Zoom in view in the area of blades. Rotating volume (VR12) is indicated with purple colour, while region VR13 is denoted around blade surface.

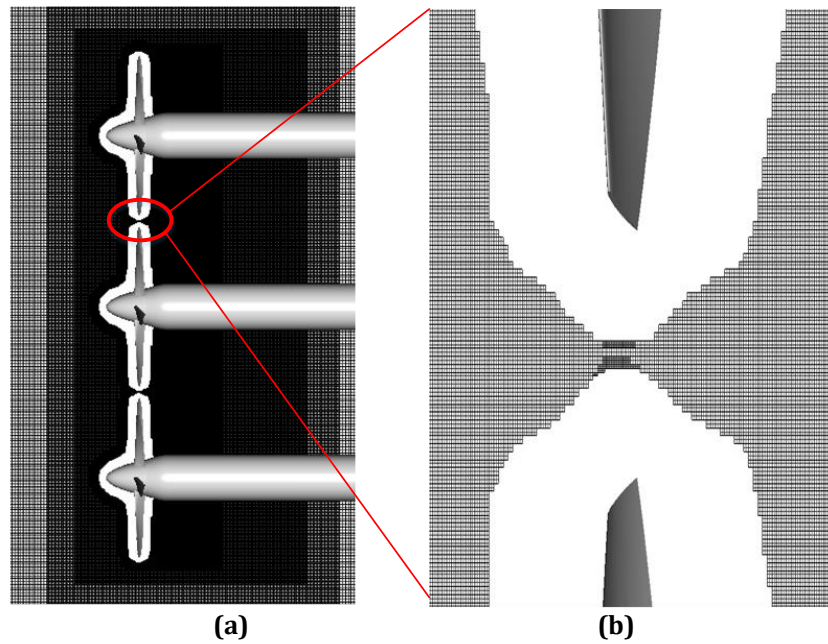


Figure 34. Grid view with different VR areas including all three propellers (a); zoom in view of the separation distance between the propellers (b).

3.3 Acoustic measurements

The aeroacoustic analysis is based on computing the acoustic pressure in the far-field. For this reason, 100 points radially distributed around the propeller with a radius equal to $10D$ are used to measure the acoustic pressure. The points for measuring the acoustic pressure in the far-field are positioned in the XY plane, as shown in Figure 35. The acoustic pressure is computed using the FWH analogy based on the pressure values on the blades and permeable surfaces located around the propellers. The sampling frequency of various measurement data is presented in Table 5.

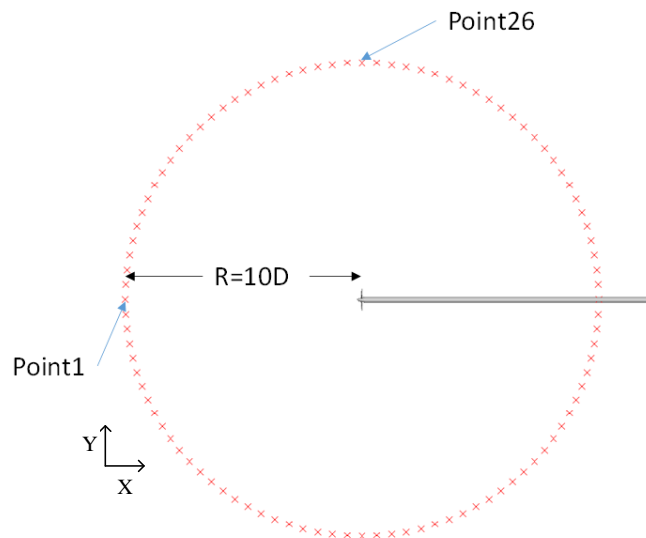


Figure 35. Sketch of propeller with the acoustic pressure measurement points at distance $10D$, where Point 1 and Point 26 are located at the front and parallel to the rotor plane.

Figure 36 depicts the permeable surfaces located around the propellers used in the acoustic analysis. The idea behind the application of three permeable surfaces is to average the acoustic pressure of each surface in the time or frequency domain [41]. Since the flow downstream of the propeller includes flow structures passing through the permeable surfaces, it creates additional fluctuations apart from the acoustic component. This is also obvious in the FWH Eq. (1.18), where the loading and thickness terms (2^{nd} and 3^{rd} terms of Eq. (1.18)) contribute to the hydrodynamic content of the flow passing through the surface. The hydrodynamic fluctuations are expressed through the flow velocity components on the surfaces of these terms that can induce spurious noise into the signal. Thus, by averaging the signal of the three surfaces, the

effect of the vortical structures of various sizes can be cancelled out. In other words, when an eddy passes through all surfaces, its effect will be cancelled out due to the different phases of the eddy projected on the permeable surface. Other authors ([41], [42]) have implemented the concept of multiple permeable surfaces. In the following analysis, the three permeable surfaces are distributed within the VR8 region (Figure 36a). This region includes 20 layers of voxels that are used as a constraint for the distance between the surfaces to keep the region's size relatively small. The offset distance of the permeable surfaces is computed based on the downstream distance that the vortical structures have travelled in the BPF. This distance is then divided by the voxel size of the local VR area to find the number of voxels that contain the vortical structures that contribute to the hydrodynamic fluctuations. Subsequently, the three surfaces are distributed evenly based on the required number of voxels.

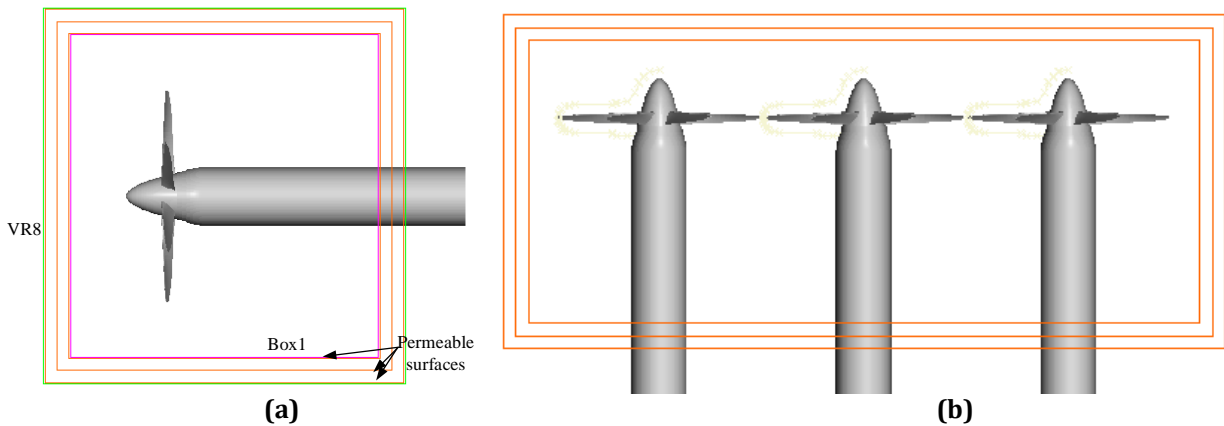


Figure 36. Permeable surface locations around the isolated-propeller (a) and distributed-propeller case (b).

3.4 Flow Conditions

Geometric and flow parameters are used in the PowerFLOW in order to non-dimensionalize the flow quantities. The flow parameters are presented in Table 2, while the thermodynamic properties of the air are shown in Table 3. The free-stream velocity has been corrected due to the blockage effects in the wind-tunnel experiments. The velocity combined with the thrust setting of the propeller determines the rotational speed. Since a high thrust setting is selected corresponding to forward flight conditions, the value of the aspect ratio is equal to 1, and the resulting rotational speed of the propeller is shown in Table 4. The propeller's root chord length is used as the characteristic length (c_r) to determine the resolution level, which is defined as the number of cells along the characteristic length. The characteristic velocity is calculated by adding the propeller's tip velocity, at 8926,2 rpm, to the free-stream velocity. The Reynolds number, based on the chord length at 80% of the radius, is calculated to be 2.1×10^5 .

Table 2. Flow parameters of the model.

Parameters	Values
Free-stream Velocity	30.23 m/s
Pressure	101325 Pa
Temperature	288.15 K
Viscosity	$1.46e-5 \text{ m}^2/\text{s}$
Propeller root chord length	0.016 m

Table 3. Thermodynamic parameters of the air.

Thermodynamic Parameter	Value
Gas molecular weight	28.96 kg/kmol
Gas specific heat ratio	1.4
Constant pressure specific heat	1004.7 J/(kgK)

3.4.1 Boundary conditions

The boundary conditions are given below:

- At the inlet boundary face, free-stream velocity is defined alongside turbulence intensity. The velocity has been corrected considering the effect of wind tunnel blockage to achieve a valid comparison with the experimental data. The values are shown in Table 4.
- At the outlet boundary face, static pressure is defined combined with a free-flow direction, as shown in Table 4.
- The solid surfaces of the spinner and blades are defined as standard walls (no-slip condition) with zero acoustic absorption and surface roughness. These components are the rotating parts, with rotational speed given in Table 4. Nacelle surfaces are defined as walls to ensure the no-slip condition.
- The remaining surfaces (floor, ceiling, left wall and right wall) are defined as frictionless walls to ensure the free slip conditions.

Table 4. Boundary conditions parameters.

<i>Boundary Conditions Parameters</i>	<i>Values</i>
<i>Inlet velocity</i>	30.23 m/s
<i>Inlet turbulence intensity</i>	0.050%
<i>Rotational speed</i>	148.8 rps
<i>Outlet Pressure</i>	101325 Pa

3.5 Time convergence-Measurements sampling

In this section, the time convergence of the setup is examined, presenting the measuring data simultaneously. Time convergence is shown through the time evolution plot of the thrust coefficient for the baseline model, as shown in Figure 37. The thrust coefficient of the middle propeller of the distributed-propeller system is plotted along the time, where time convergence is reached after four complete propeller rotations ($N_{rot}=4$). Thus, all flow measurements are saved after time convergence and the shadowed area in Figure 37 is neglected. The duration of the acoustic measurements is saved after convergence with signal duration equal to 10 rotations. Note that the time required for one complete rotation of the propeller is about $t_{rot}=0.0067$ s. For high-resolution cases, the simulations are seeded with the solution of the preceding simulation with a coarser grid to reduce the transitional period.

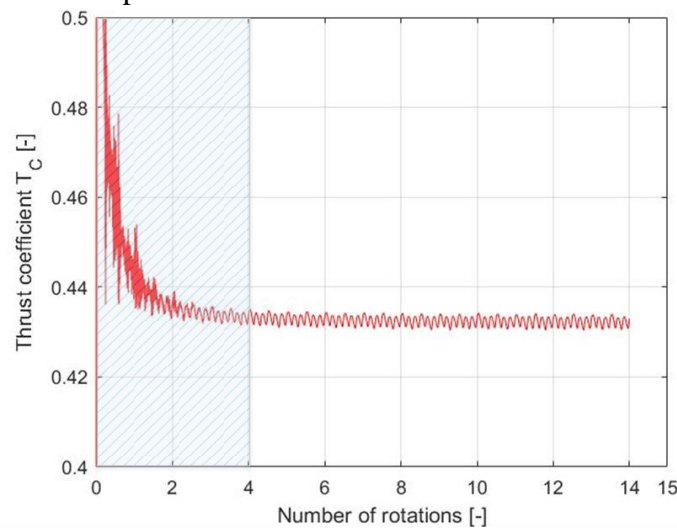


Figure 37. Time evolution plot of thrust coefficient for Propeller#1 of the baseline model. The light-blue-shadowed area denotes the transient period before convergence.

The resulting flow and acoustic data are subsequently saved. Three complete rotations of the propellers are saved regarding the flow data, and their data are post-processed for analysis. The measurement data and their sampling rates are shown in Table 5. The mean flow is sampled in time equal to one revolution of the propeller, while the transient flow is sampled every 7.5° of the propeller's rotation. Sampling data at a higher frequency would negatively impact the computational effort due to the large memory required to save these files. At the same time, no additional information on the flow analysis will be extracted, and thus the

selection of the transient flow frequency was based on a trade-off to keep the memory relatively low and an adequate number of frames necessary to assess the unsteady phenomena.

The acoustic sampling data on solid and permeable surfaces are presented in Table 5. Regarding the solid formulation, the acoustic signal of the blade surfaces is considered only for the analysis, as the rest of the solids (nacelle and spinner) do not affect the resulting noise significantly. The sampling frequency is equal to 15 times the 1st harmonic (BPF). Also, a safety factor of 2.2 is used to avoid the aliasing effect, based on the Nyquist frequency that requires the sampling frequency to be at least two times the highest measured frequency of the signal. The analysis of the output signals is done based on Welch’s method [26], where the signal is transformed to power spectral density in the frequency domain, and the post-processing analysis is performed as presented in Section 2.3.1. This method reduces the numerical noise compared to a straightforward discrete Fourier transform by applying multiple transformations on overlapping segments. Regarding the permeable surface formulation, the same sampling frequency with the solid formulation is applied. For high-resolution cases, like 200 voxels/ c_r , the grid is fine enough to neglect any potential difference between the sampling frequencies of the two formulations, as can be seen by the values in Table 5. The number of signal points used for the Welch method slightly differs between the two formulations, i.e. 1853 points are used for the solid formulation analysis and 1809 for the permeable. This difference is attributed to some inconsistencies at the start of the acoustic pressure signal that were neglected. The Hanning window used in the analysis has the same length as the discrete Fourier transform points with 50% overlap.

Table 5. Measurement data with sampling frequencies.

<i>Measurement data</i>	<i>Measuring period [s]</i>	<i>Sampling frequency [Hz]</i>
<i>Forces</i>	<i>1 timestep</i>	<i>7422000.0</i>
<i>FWH Solid formulation</i>	<i>0.000034</i>	<i>29570.0</i>
<i>FWH Permeable formulation</i>	<i>0.000034</i>	<i>29570.0</i>
<i>Transient flow</i>	<i>0.000140</i>	<i>7144.0</i>
<i>Mean Flow</i>	<i>0.006722</i>	<i>148.8</i>
<i>Near-field planes</i>	<i>0.000102</i>	<i>9831.0</i>

3.6 Experimental setup

The experimental setup performed by de Vries, et al. [11] is used for validating the computational results. This section provides an overview of the experimental setup that has been used for this purpose. The experiments were performed at the low-speed, low-turbulence tunnel (LTT) at Delft University of Technology. The turbulence levels of the tunnel are below 0.04% for the nominal free-stream velocity of 30 m/s, which was implemented. The test section has an octagonal cross-section of {1.25x1.8 m}, as depicted in Figure 38. An array of three propellers was used in the setup so that the flow conditions perceived by the middle propeller were representative of a distributed propulsion configuration. Uncertainty installation procedures showed that the tip clearance varied by less than 0.5 mm among the different measurements of a determined separation distance setting. The effective free-stream velocity was corrected for nacelle, supporting, and slipstream blockage, which was found to range between -0.5% and 1.0% of the nominal free-stream velocity, depending on the configuration and thrust setting. The uncertainty of the performance curves was estimated considering potential misalignments in propeller angle-of-attack, errors in the temperature-calibration factors and error in operating conditions. The resulting error bars present a 95% confidence interval for a determined propeller geometry, while the performance of the propellers showed deviations of approximately $T_c = 0.005$.

The wake-pressure measurements were performed using a Pitot probe and vertical wake rake containing 74 total-pressure probes. This combination enabled the computation of a two-dimensional pressure distribution of the flow field. The pressure sensors present uncertainty of ± 4 Pa on the full-scale measurement range, corresponding to $\pm 0.7\%$ of the free-stream dynamic pressure. The total-pressure distribution behind the propellers was measured at two locations: close to the propeller ($X/R = 0.2$), which reflects the non-uniform loading distribution on the propeller disk, and further downstream ($X/R = 1.2$), to determine whether the slipstreams had deformed significantly at a typical wing leading-edge location.

A stereoscopic particle-image velocimetry (PIV) setup was used to obtain the propellers' velocity distributions. A mixture of diethylene-glycol and water was used for flow seeding, obtaining tracer particles with an average diameter and relaxation time below $1\ \mu\text{m}$ and $1\ \mu\text{s}$, respectively, while the illumination was performed through a 200 mJ Nd:YAG laser. Image records at several planes were used to provide information on the time-averaged velocity field upstream and downstream of the propellers. The uncertainty range of the instantaneous velocity in the downstream direction reached 3.7% of the free-stream velocity, while it is only 0.2% for the mean velocity.

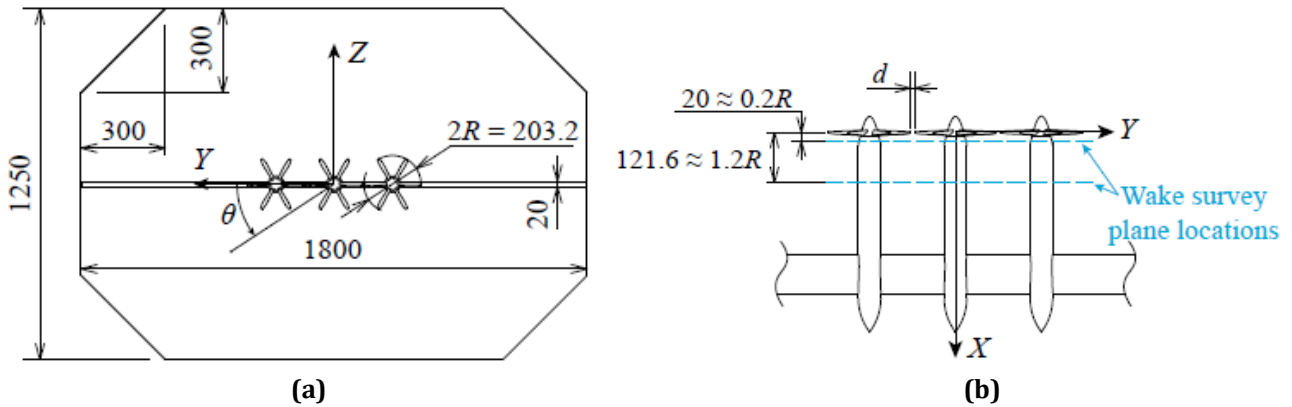


Figure 38. Front view (a) and top view(b) of the experimental setup indicating the main dimensions, reference system and configuration layout [11].

4

Resolution and Validation Study

This chapter presents the resolution and validation study of the numerical simulation for both the isolated- and distributed-propeller models. Initially, the isolated propeller is examined for different resolution levels and compared to the experimental data. The change in the resolution level illustrates the impact of the computational grid on the propeller's performance. Subsequently, the aeroacoustic resolution study presents the effects on noise emission for the isolated propeller. The last section of this chapter describes the comparison of the distributed-propeller model with the experimental data.

4.1 Isolated-propeller case

Initially, a grid convergence study is performed to examine the impact of the computational grid in the numerical solution. For this reason, the time-averaged thrust coefficient (T_c) of the isolated propeller for different resolution levels is compared with experimental results. The resolution (Res) is defined as the number of elements along the root chord of the propeller in the region of highest refinement (VR13 region), in voxels/ c_r . Four different resolution levels were examined, and the resulting time-averaged thrust coefficients are shown in Figure 39 and Table 6 compared to the experimental data. In Figure 39, the T_c values correspond to the fine equivalent number of voxels for the different resolution levels. With light yellow colour, the uncertainty range of the experimental analysis is shown. Table 6 depicts the different resolution levels with the corresponding equivalent number of voxels and the T_c values. Although the thrust coefficient presents an increasing trend for the low-resolution cases (for Res=50 and 100 voxels/ c_r), the opposite is the case for high-resolution levels. Thrust coefficients drop significantly for the cases of Res=150 and 200 voxels/ c_r , showing a discrepancy between the experimental curve and the numerical ones at high resolutions equal to 6.5%. Nevertheless, the comparison between the different resolution levels shows a converging trend, as the change between 150 and 200 voxels/ c_r is 0.3% (Table 6). The small change in the T_c for the high-resolution cases denotes that the impact of the grid is minor.

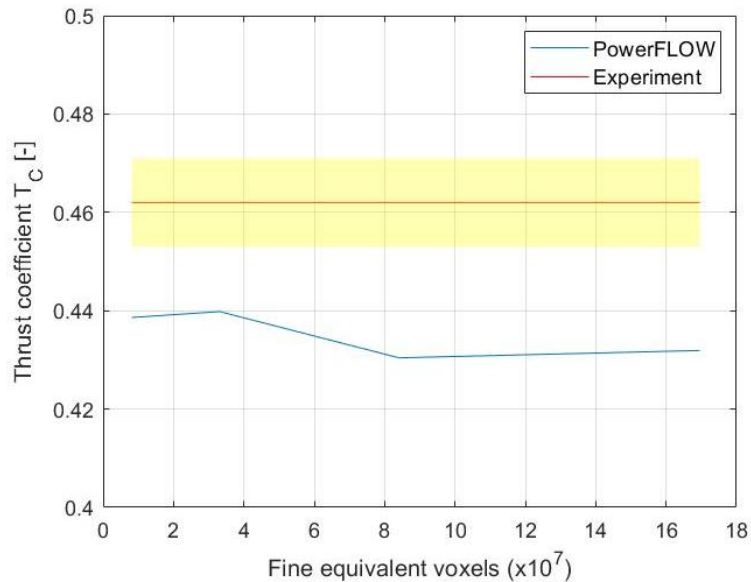


Figure 39. Time-averaged thrust coefficient of isolated propeller for different number of fine equivalent voxels. Experimental results are also visible for comparison, with the light yellow colour denoting the uncertainty range.

Table 6. Time-averaged thrust coefficient values at different resolution levels.

<i>Resolution level [voxel/c_r]</i>	<i>Fine equivalent voxels</i>	<i>T_c [-]</i>	<i>Relative change [%]</i>
50	8126291	0.4386	-
100	33139828	0.4398	0.271
150	84067940	0.4304	-2.184
200	169578122	0.4319	0.346

The small effect of the grid in high-resolution levels is also evident in the thrust coefficient distribution along Blade1. Figure 40 presents the thrust coefficient distribution per blade's segment at three different resolution levels (Res=50, 150 and 200 voxels/c_r). The small impact of the grid is noticed in the two curves of the two high-resolution levels, which are almost identical without major discrepancies.

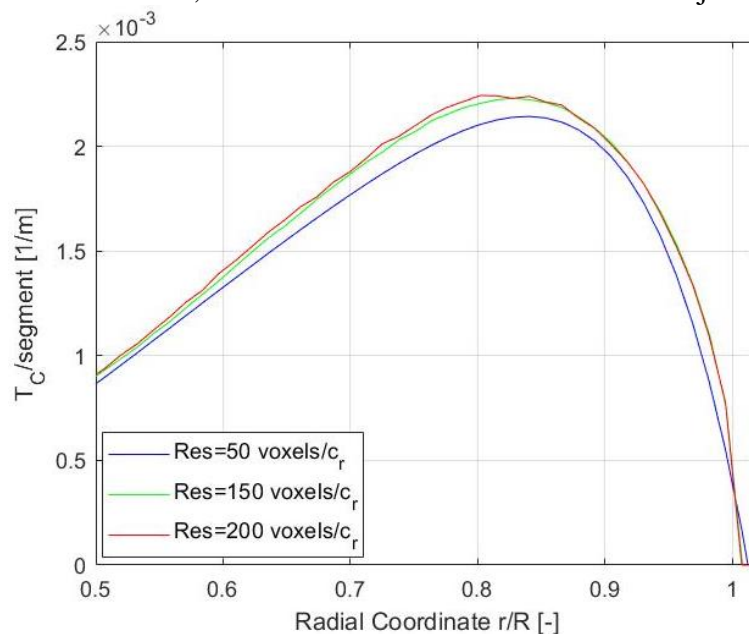


Figure 40. Distributions of time-averaged thrust coefficient per segment of Blade1 at different resolution levels.

The convergence of the solution is also examined through the analysis of the velocity distributions at different resolutions. Observing the propeller's axial velocity plots upstream (Figure 41) and downstream (Figure 42) underlines the difference between experiments and simulations. The velocity distributions

correspond to the time-averaged solution during one propeller rotation. These values were measured upstream and downstream of the propeller in planes 10% and 60% of the diameter, respectively. The comparison of the experimental and numerical curves illustrates that the axial velocity at inboard sections ($r/R < 0.8$) of the blade span is reduced as the resolution increases (Figure 41). Similarly, the downstream axial velocity curves (Figure 42) illustrate a discrepancy with the experimental data. The discrepancy between the numerical and experimental axial velocity curves is associated with the time-averaged thrust coefficient differences (Figure 39). The reduced axial velocity downstream of the propeller is attributed to the reduced loading on the blades, as denoted by the actuator disc theory, where the thrust is the momentum difference between the downstream and the free-stream flow. Thus, the resulting downstream flow will have low axial velocity in case of the same free-stream velocity and decreased thrust generation. In addition, the maximum velocity value is shifted outboard (at $r/R \sim 0.8$) compared to the respective value for the experimental curve ($r/R \sim 0.7$). This implies a difference in the thrust distribution along the blade span, as the thrust distribution based on the numerical analysis shows a high loading at $r/R = 0.82$, as shown in Figure 40. Upstream of the propeller, the axial velocity is determined by the induced effects of the trailing vorticity by the propeller. As will also be discussed later, the vorticity of the slipstream induces velocity components upstream of the propeller, contributing to the increase of the axial velocity compared to the free-stream one. Therefore, the discrepancy of the experimental and numerical curves is attributed to the differences in vorticity systems of the two cases.

In parallel, the velocity curves for the different resolution levels seem to converge in high-resolution cases. As observed in the two high-resolution cases (Res=150 and 200 voxels/ c_r), the axial velocity curves at the inflow plane are almost identical, while the respective curves in the downstream direction show only minor differences at approximately 70% of the blade span. Thus, the grid resolution does not impact the flow field, resulting in a grid-independent solution. Thus, it is suggested that the resolution of 200 voxels/ c_r is adequate for the following aerodynamic analysis.

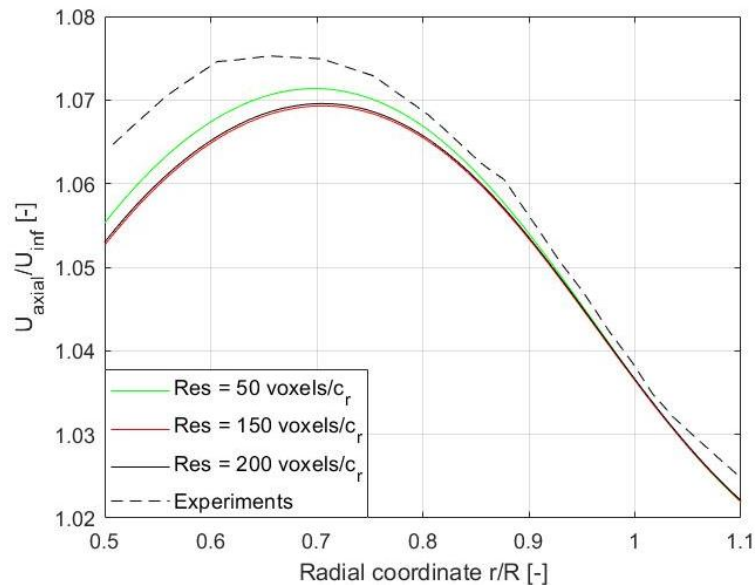


Figure 41. Time-averaged axial velocity distribution measured upstream of the propeller at 10%D for different resolution levels. The experimental data is plotted for comparison.

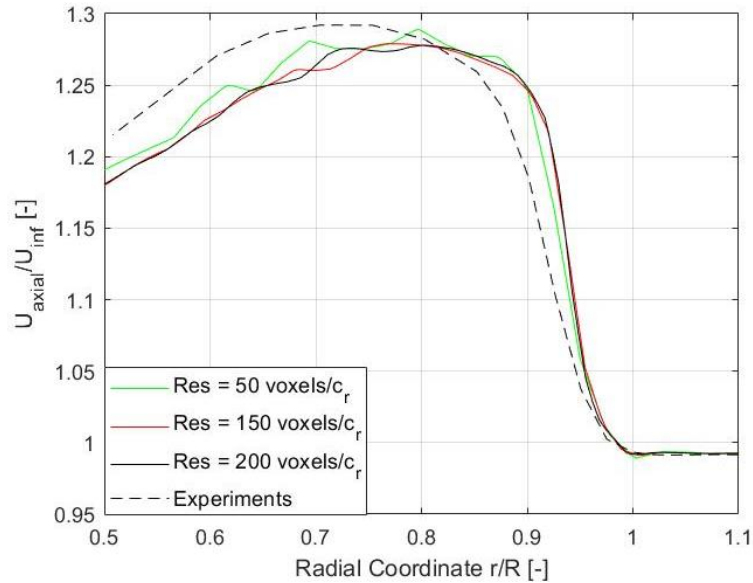


Figure 42. Time-averaged axial velocity distribution measured downstream of the propeller at 60%D for different resolution levels. The experimental curve is plotted for comparison.

The analysis of the six blades' performance shows a noticeable difference in thrust production up to 10.9%. Observing Table 7, it is noticed that Blade1 contributes the most to the total thrust, whereas Blade2 the least. Blade1 shows enhanced thrust generation up to 0.11 N compared to the other two blades. Similarly, the remaining blades (Blades 4, 5 and 6) show the same performance as their symmetric ones. For clarity, only the results for the first three blades are discussed later on. The propeller shows a non-uniform behaviour, which is not expected in an isolated-propeller model of uniform flow conditions. The discrepancy between the blades is also evident in the (time-averaged) thrust distribution along the bladespan in Figure 43. Thrust coefficient distributions show a difference in performance across the blade span at inboard sections and the maximum loading location. The curve of Blade1 presents a clear difference from the other two curves, which are close to each other, implying the major contribution in thrust production. So, a deep analysis of the blade loading is needed to understand this difference between the blades.

Table 7. Thrust and thrust coefficients of the propeller's blades.

	$T_c [-]$	$Thrust [N]$
<i>Blade1</i>	0.076489	1.342
<i>Blade2</i>	0.068974	1.210
<i>Blade3</i>	0.070570	1.238
<i>Blade4</i>	0.076469	1.342
<i>Blade5</i>	0.068684	1.205
<i>Blade6</i>	0.070574	1.238

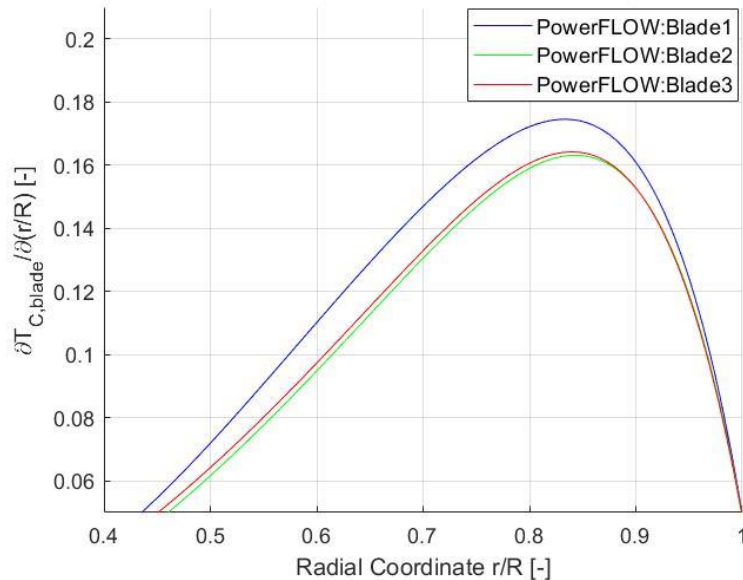


Figure 43. Time-averaged thrust coefficient distributions for the three blades of the isolated propeller.

Pressure coefficient distributions at different blade locations reveal the differences in the loading for Blades 1, 2 and 3. Figure 45 illustrates the time-averaged pressure coefficient (C_p) distributions for the three blades at two radial locations, i.e. 50% and 70% of the blade span. Specifically, the pressure coefficient curves at 50% of the radius depict that Blade1 has higher suction values than the other two blades. However, the behaviour of Blades 2 and 3 presents a noticeable difference from Blade1 at the trailing edge. The relatively flat curve near the trailing edge of these blades is associated with a flow separation that takes place, while in Blade1 this trend is less pronounced. This implies a different behaviour of the boundary layer evolution, as shown in the flow field cross-sections at this span location. Carefully inspecting the flow in Blade 2 in Figure 46b, it is evident that the flow is separated earlier than in Blade1, as the region near the trailing edge, with low axial velocity values, is enlarged. Near the trailing edge of the cross-section for Blade1, the region of zero axial velocity is smaller than the respective region in Blade2. In addition, the flow field of Blade2 includes flow structures downstream of the cross-section (see annotation in Figure 46), not present in the flow field of Blade1, where the flow downstream of the Blade1 is smooth and uniform. Therefore, the differences between the blades are attributed to the high suction values of Blade1 and the different evolution of the boundary layer in Blades2 and 3.

The airfoil performance is strongly related to its boundary layer, which is affected by the Reynolds number regime. Figure 44 depicts the streamlines schematically over an airfoil at different Reynolds numbers and for a moderate angle of attack. At a low Reynolds regime (up to 5×10^4), the boundary layer is laminar, and the separation, if it occurs, takes place near the trailing edge. As the angle of attack increases, the separation point shifts towards the leading edge, with the shear layers unable to transition and reattach on the surface, leading to poor lift generation and high drag production [43] (Figure 44a). In higher Reynolds number regimes (from 5×10^4 to 10×10^4), the separated flow re-attaches on the airfoil (Figure 44b) contrary to the lower Reynolds numbers. As the shear layers get separated, they gain momentum by the free-stream flow leading to flow reattachment as a turbulent boundary layer. This creates a separation bubble, increasing airfoil drag. At even higher Reynolds numbers (greater than 50×10^4), the initially laminar flow separates from the surface due to the adverse pressure gradients but quickly reattaches due to the momentum of the free-stream. Since the turbulent boundary layer is energized from the free-stream, it is less prone to separation than the laminar one [43]. At a high angle of attacks, the turbulent boundary layer starts separating from the trailing edge, resulting in increased drag and lift drop. Eventually, airfoil will stall with a further increase in the attack angle, with lift decrease and drag increase.

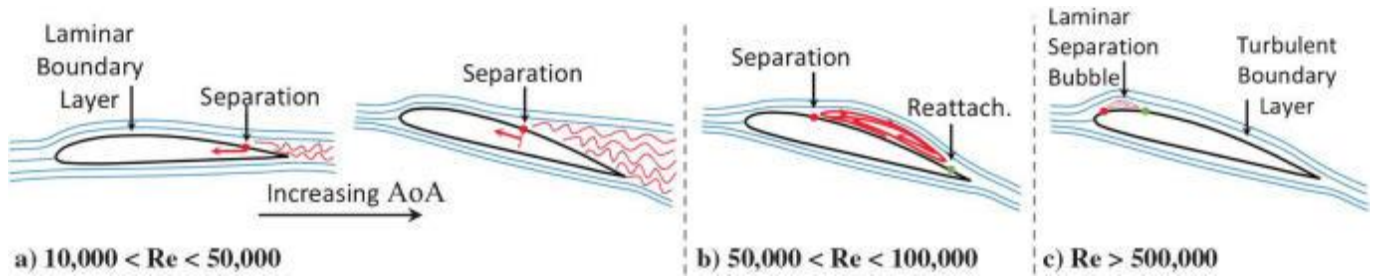


Figure 44. Illustration highlighting conventional airfoil separation characteristics at different Reynolds number regimes below 10^6 [43].

A potential explanation of this behaviour could be related to the location of the blades in the Cartesian coordinate system. The discretization process is based on the initial position of the blades with respect to the Cartesian coordinate system. Thus, the computational grid around the six blades with various orientations would differ. Figure 47 depicts the computational grid around Blades 1 and 2. It is evident that voxel distribution around Blade1 (aligned with Y-axis) is almost parallel to the geometric shape of the blade's cross-section. However, the voxel distribution around Blade2 is different, with the edges of voxels crossing the blade's cross-section. This is attributed to the oblique orientation of Blade2, whose angle with the Y-axis is 60° . Thus, it is conjectured that a different orientation of the blades would result in a change in performance and potentially erase all differences between the blades. This analysis is presented in the subsequent section, where the impact of the location of the blades with respect to the Cartesian axis is examined.

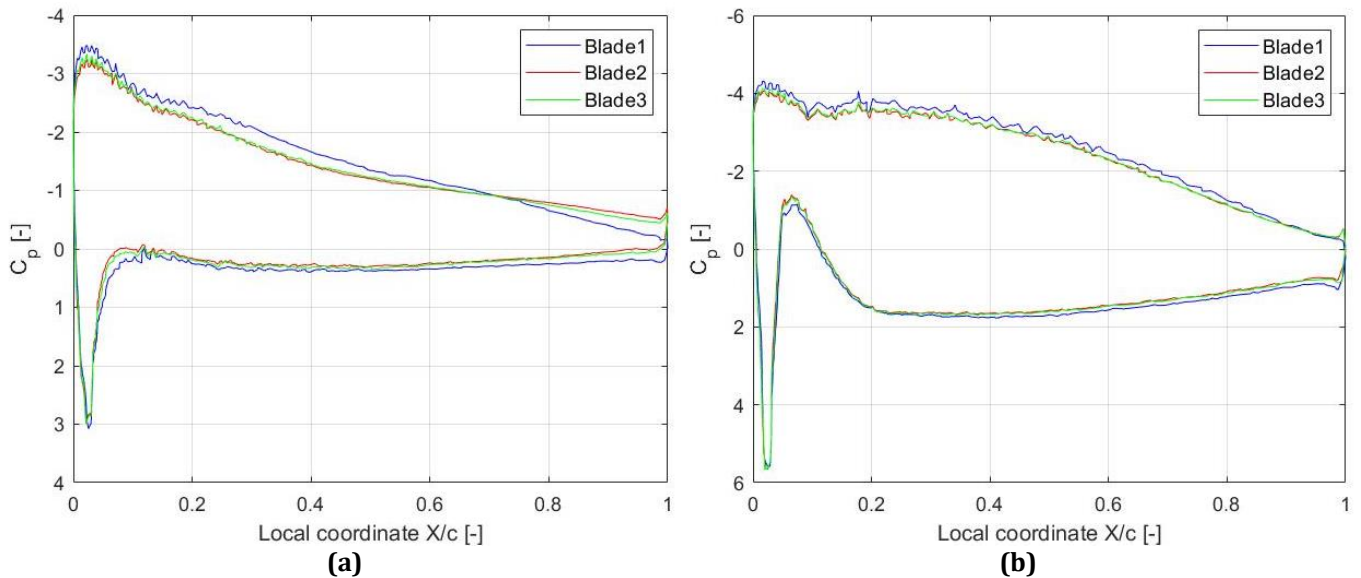


Figure 45. Pressure coefficient (C_p) curves for the three blades at radial position $r/R=0.5$ (a) and 0.8 (b).

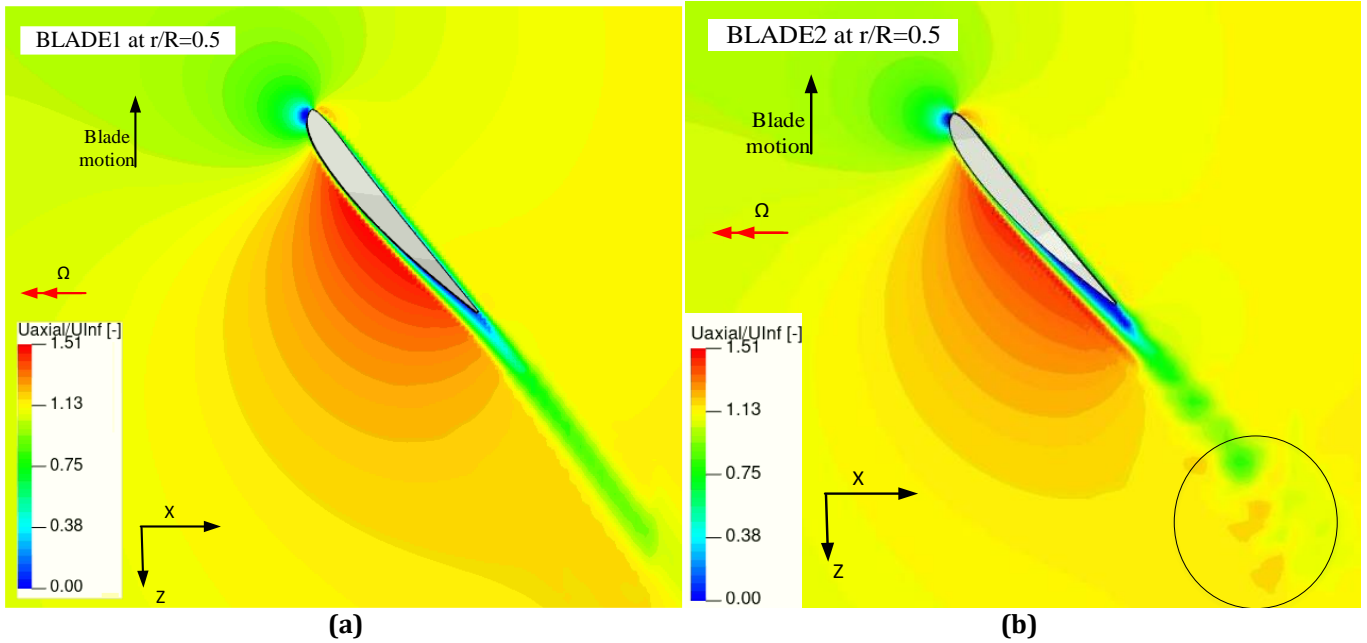


Figure 46. Phase-locked normalized axial velocity flow contours for Blades 1 (a) and 2 (b) at radial position $r/R=0.5$.

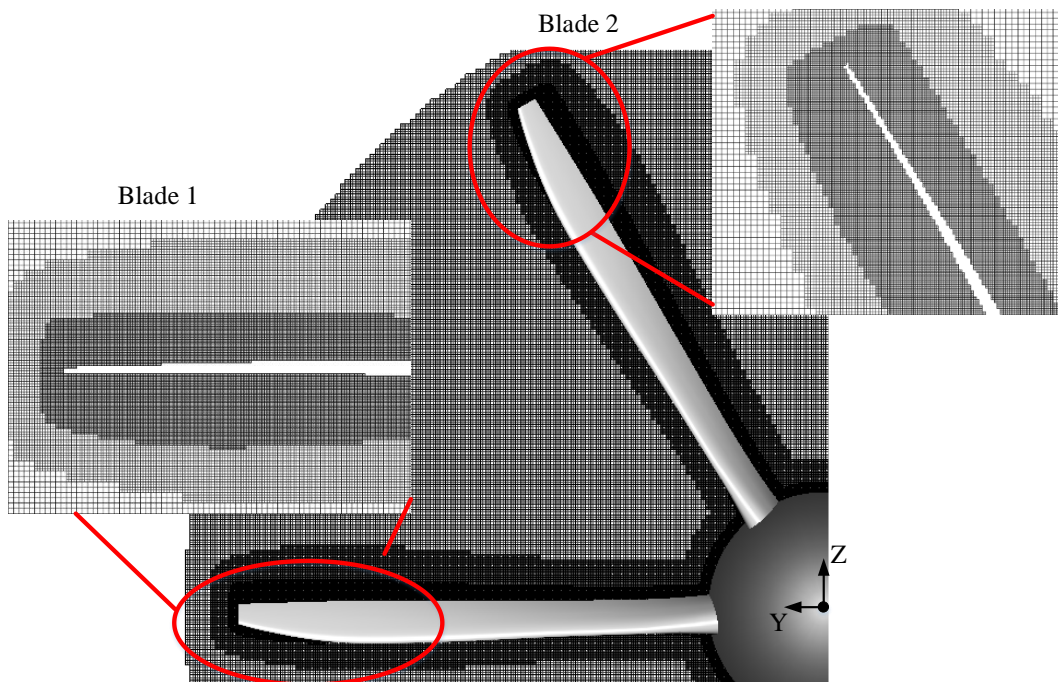


Figure 47. Grid view of the voxels distributions inside the rotating volume (YZ plane). Zoom in views shows the difference in voxels around Blade1 and Blade2.

4.1.1 Effect of blades azimuthal position with respect to the Cartesian axis

The current section presents the impact of blades orientation with respect to the Cartesian coordinate system on their performance. The blades thrust coefficients are evaluated at various azimuthal angles to identify potential changes. Apart from the above-mentioned model (Case1-Figure 48), two other cases are tested: propeller rotation by 15° (Case2-Figure 49a) and propeller rotation by 30° (Case3-Figure 49b). In Case2, Blade1 forms an angle with Y-axis equal to 15° , which is equal to the angle that Blade2 has with the Z-axis. Thus, it is expected that the grid generation will be the same around these blades, and their performance will be equal. On the contrary, in Case3, Blade2 is aligned with the Z-axis, and Blade1 is oblique by 30° to the Y-axis. In this case, it is expected that Blade2 will have increased performance compared to Blade1,

similarly to Case1. To reduce the simulations' computational cost, the resolution corresponds to 150 voxels/ c_r without any loss of the general trend.

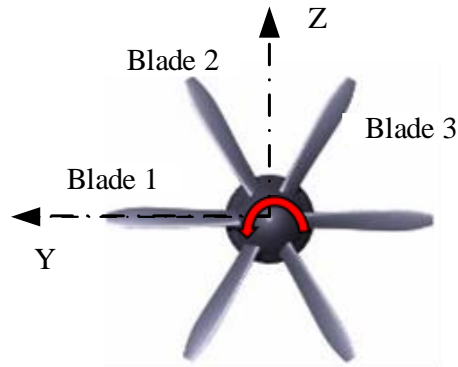


Figure 48. Case1: Blade 1 is aligned with the Y-axis, while Blades 2 and 3 are oblique by 30° with the Z-axis. The red arrow shows the direction of rotation.

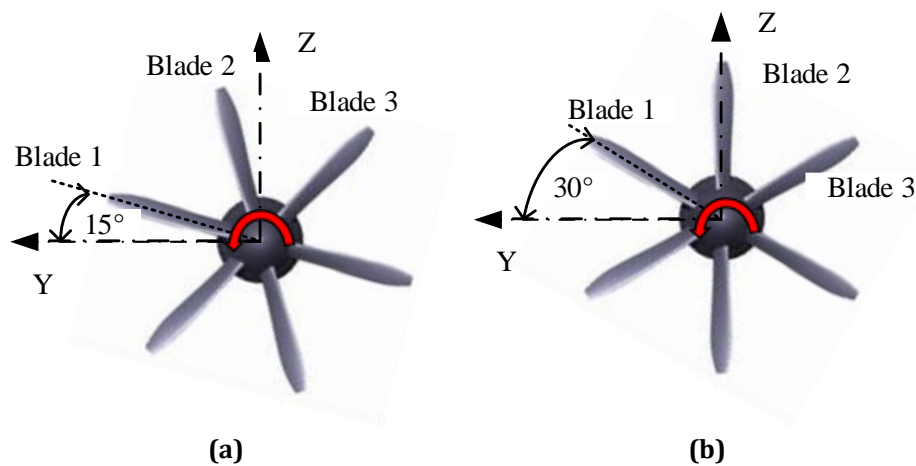


Figure 49. Case2 (a): Blade 1 is rotated by 15° wrt Y-axis, and Case3 (b): Blade 1 is rotated by 30° and Blade 2 is aligned with Z-axis. The red arrow shows the direction of rotation.

4.1.1.1 Performance analysis

The change in thrust coefficients for the three cases illustrates the effect of the blades' orientation on their aerodynamic performance. The bar chart (Figure 50) shows the T_c values of the three blades for the three different cases (in Figure 48 and Figure 49). The comparison of Case1 and Case3 reveals a reversed behaviour of Blades1 and 2. The thrust production of Blade2 in Case3 is almost equal to the respective value of Blade1 in Case1 ($T_c = 0.0759$). The resulting thrust drop in Case3 for Blade1 is 7.8%. This result justifies the initial assumption for Case1 and Case3 that the blades aligned to the Cartesian axes will behave the same and have enhanced performance compared to the oblique ones. Contrary to the behaviour between Case1 and 3, the performance of Blades1 and 2 are similar in Case2. The relative difference of the thrust coefficients values is 0.53%, implying that their performance is almost identical. Thus, the blades' performance is identical when equally spaced with respect to the Cartesian axes, confirming the initial assumption. In all three cases, the blade that contributes the least to the propeller's thrust is Blade3 which has a decreasing trend (0.34% in Case3 compared to Case1). The discrepancy between Blades 1 and 3 remains significant even for Case2, equal to 5.5%, while this difference rises for Cases1 and 3 to 9.3%. Due to the existence of 6 blades, it is not possible to rotate all blades such that they are equally spaced with respect to the Cartesian axes and have the same thrust production.

This blades behaviour should be associated with the different voxels distribution around the propellers. Figure 51 depicts a cross-section view of the computational grid for Case2, with zoom-in views showing the voxels distribution around Blade1 and 2. It is observed that the cells' distribution around the blades is almost identical, with the voxel edges oblique to the blades' surfaces cross-sections. The similar grid distribution around these blades results in a similar performance. On the contrary, Blade3 has a different orientation angle with the Cartesian axis, leading to a different voxels distribution around its surface,

affecting its performance. In Case3, Blade2 is aligned with the Z-axis resulting in a distribution of voxels parallel to its surface, similar to Blade1 for Case1.

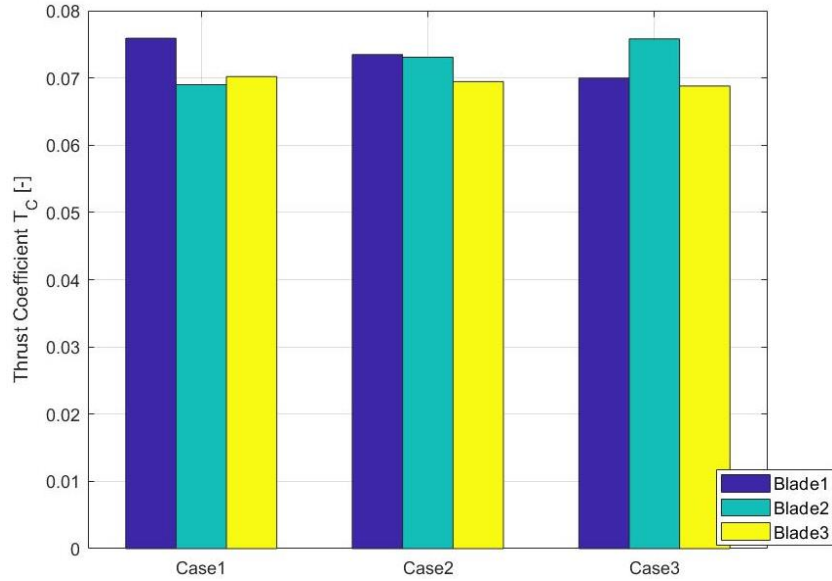


Figure 50. Evolution of thrust coefficient per blade for the different cases of initial azimuthal positions. Case 1 corresponds to a 0° angle for Blade 1 with respect to Y-axis, Case2 corresponds to 15° and Case3 to 30°.

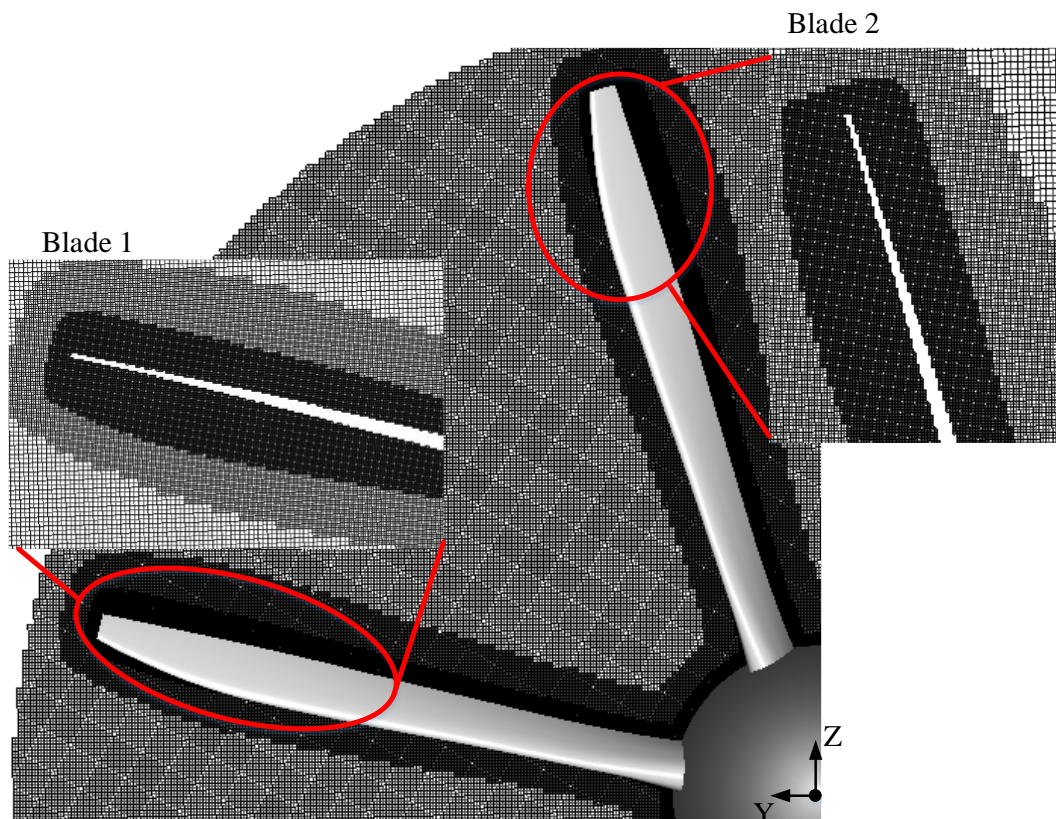


Figure 51. Grid view of the voxels distributions inside the rotating volume (YZ plane) for Case2: Rotated by 15° wrt to Y-axis. . Zoom in views shows the difference in voxels around Blade1 and Blade2.

The change in blades' performance is also depicted through the pressure distributions and the flow field. The C_p values of Blades 1 and 2 for the three cases, at a spanwise location equal to 50% of the radius (Figure 52), reveals a change in their behaviour. The reduced performance of Blade1 is evident by the decrease in suction values in Case3 compared to the rest of the cases. In Case2, the performance of Blade1 is slightly reduced, as shown by the thrust coefficient decrease of 3.2% in Figure 50. The phase-locked axial velocity field for Blade1 in Case3 is depicted in Figure 53a. It is noticed that the flow field in Case1 (Figure

46a) has changed, with reduced C_p values in the suction side and vortical structures are present after the trailing edge that does not exist in Case 1.

Regarding Blade 2, the increase in suction peak value combined with the different curvature near the trailing edge for Case 3 justifies the enhanced performance. This is also visually verified by the cross-sectional flow field (Figure 53b). The previously observed vortical structures (associated with the flow separation in Figure 46b) have disappeared, and a uniform flow in the downstream direction is evident. As a result, this analysis showed that the occurring inconsistencies between the blades of the same propeller are highly related to the initial position of the blades with respect to the Cartesian axis. Since the propeller has six blades, it is inevitable to avoid the performance difference between the blades by properly rotating the propeller to achieve equally spaced angles with respect to the Cartesian axis. Thus, the following analysis will refer to Case1, where Blade 1 has a 0° angle with the Y-axis unless mentioned otherwise.

A potential solution to achieve identical performance on all six blades would be to place zig-zag trips of the suction side. Since the evolution of the boundary layer on the blades is different, placing transition trips would lead to the same phenomena on all blades. Flow transition from laminar to turbulent is induced by applying blade tripping, affecting the performance of the blades. The implementation of this tape will enhance the flow instabilities leading to turbulent flow [44]. Thus, the turbulent boundary layer will be less prone to potential flow separations than the laminar one [43].

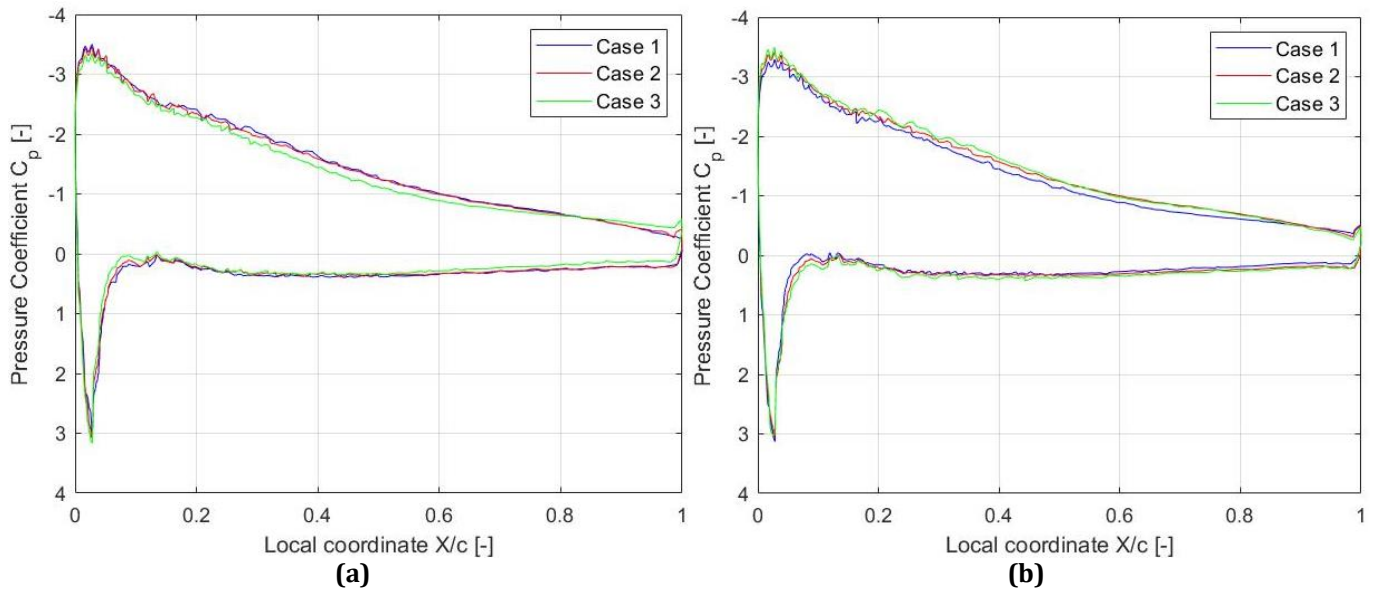


Figure 52. Pressure coefficient (C_p) values of Blade 1 (a) and 2 (b) at radial position $r/R=0.5$ for all three cases.

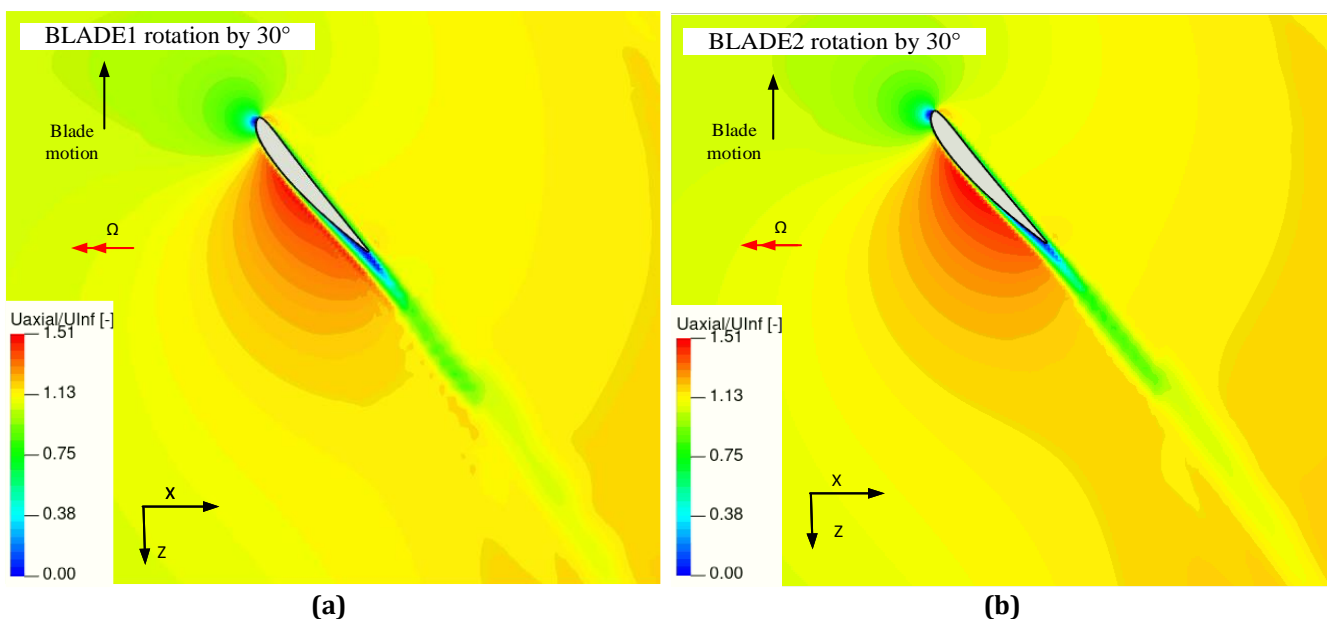


Figure 53. Phase-locked normalized axial velocity contour for Blades 1 (a) and 2 (b) corresponding to Case 3 at radial position $r/R=0.5$.

4.2 Aeroacoustic resolution study

The analysis of the aeroacoustic solution is necessary to examine the system's behaviour at different resolution levels and compare the solid and permeable surface formulations. The frequency-domain analysis takes place using the signal's power spectrum to compute the tonal and broadband components. This analysis will depict the energy content of the signal at different frequencies. The frequency range that will be examined in the present thesis extends up to the 10th BPF with range [0-8920Hz]. Initially, the convergence of the solid surface formulation is examined, followed by the comparison between the permeable and solid surfaces.

The implementation of the FWH analysis for the solid surface formulation reveals the acoustic signal considering only the solid blades of the propeller. The change of the overall sound pressure level (*OSPL*) at different resolution levels indicates the level of grid convergence of the solution. The comparison of the *OSPL* values along the propeller plane at $\theta=90^\circ$ (along the propeller plane) shows a converging trend (Figure 54a). The values at the two highest resolution cases differ by 0.7 dB, while this difference increases for low resolutions. At the same time, the *OSPL* at 1st BPF varies less than 0.2 dB for the high-resolution cases, while the converging trend is evident when all frequencies are considered up to 5th BPF [0-4460Hz] (Figure 54b). The difference between the two high-resolution cases is less than 0.5 dB. On the contrary, the broadband component (with a range from 5th to 10th BPF) shows a constantly increasing trend with the resolution level. This is also noticed in the spectrum plot (Figure 55) for different resolution levels, where the spectrum at high frequencies (frequency/BPF>5) for the high-resolution case (Res=200 voxels/c_r) shows enhanced power compared to the other two resolution levels. The increase in the high-frequency components is the reason for the *OSPL* values increase in Figure 54a.

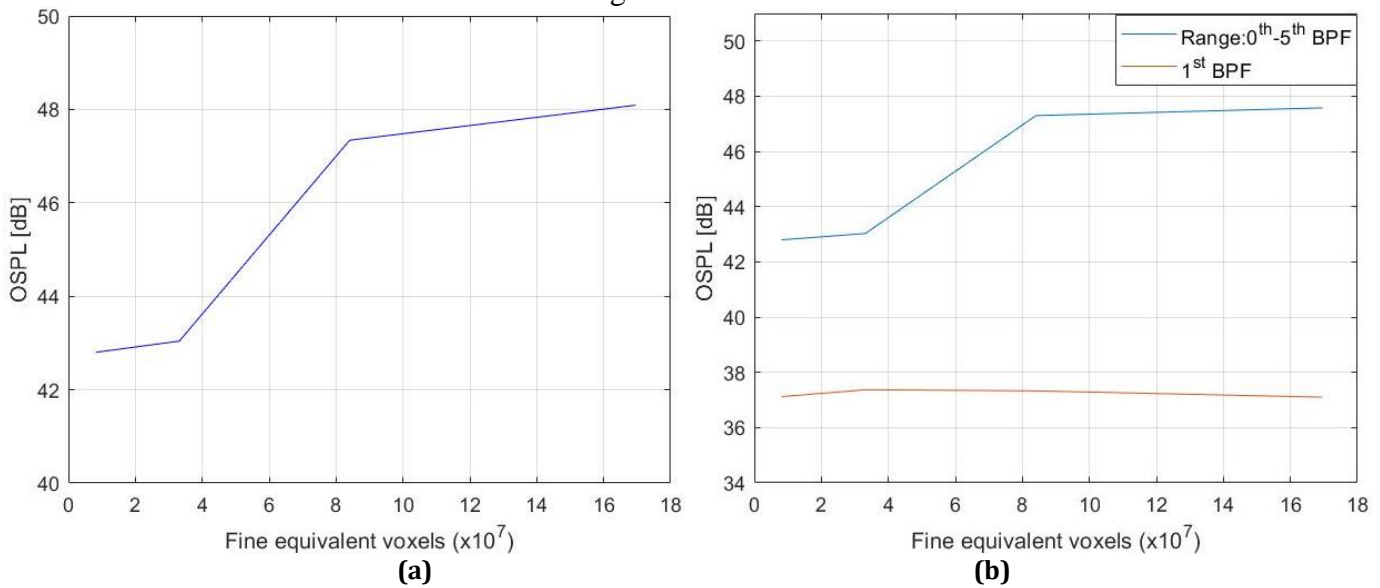


Figure 54. Variation of Overall Sound Pressure Level (*OSPL*) values along the propeller plane ($\theta=90^\circ$) for different resolution levels (a). *OSPL* values of the 1st BPF and up to the 5th BPF [0-4460Hz] for different resolution levels (b).

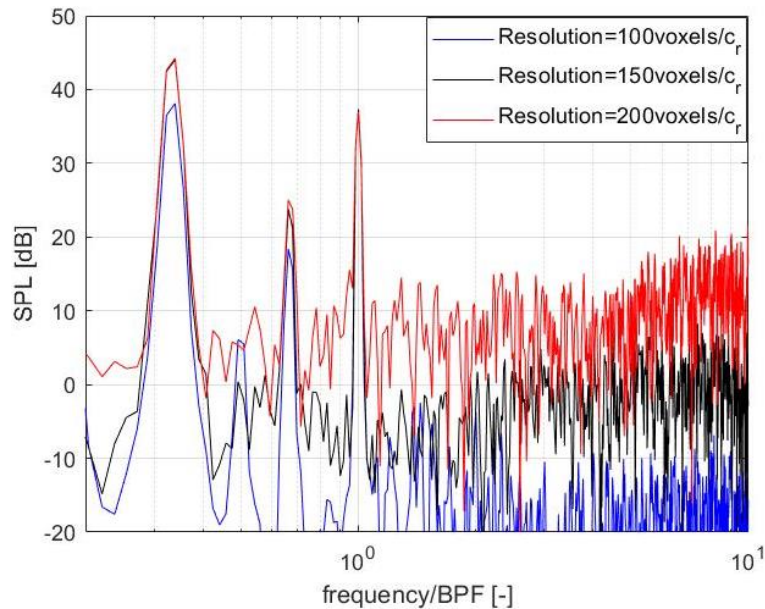


Figure 55. Variation in spectrum level of the acoustic signal along the propeller plane ($\theta=90^\circ$) for different resolution levels.

Carefully inspecting the power spectrum curves at emission angle $\theta=90^\circ$ (Figure 55), it is interestingly found that apart from the high power level at BPF, there is another dominant tone at $1/3$ of BPF. This tone exists at both low- and high-resolutions, in angles close to the propeller plane. The *SPL* value at BPF is 37.0 dB for the high-resolution case, while at $1/3^{\text{rd}}$ of the BPF, it is 44.2 dB, making this tonal peak dominant. The tonal peaks at higher frequencies cannot be clearly predicted. The dominance of the $1/3^{\text{rd}}$ BPF is not expected in an isolated propeller, as the dominant tonal frequency is at the BPF. However, this behaviour should be attributed to the discrepancy of thrust between the propeller's blades. Two out of six blades (Blade1 and 4) contribute the most in thrust generation, as described in Section 4.1, with 10% more thrust than the rest of the blades. Thus, this loading difference would lead to an acoustic power increase in rotational frequency equal to $1/3^{\text{rd}}$ of the BPF.

Since the discrepancy between the blades thrust production has been associated with the grid generation, the aeroacoustic signature is also compared for the different cases examined in Section 4.1.1. As observed in Figure 50, the performance of Blades1 and 2 are similar with a difference of 0.5% between Case1 and Case2, but there is still a discrepancy between Blade1 and 3 equal to 5.5%. As a result, the loading noise component creates a dominant tonal noise at $1/3^{\text{rd}}$ of BPF, as shown in Figure 56. The comparison between Case1 and Case2 shows a reduced power in $1/3^{\text{rd}}$ BPF by 4.5 dB, implying that the 15° angle reduced the acoustic signature deviations due to the loading differences between the blades. Nevertheless, the thrust discrepancy is still evident, resulting in a tonal noise at the $1/3^{\text{rd}}$ of BPF. Case 3 has an identical acoustic signature with Case1, as expected, as the behaviour of Blade1 and Blade2 in the two cases has been reversed. Thus, although the change of the blades angle with respect to the Cartesian axis affect the acoustic signature, it does not dominantly reduce the tonal component at $1/3^{\text{rd}}$ of the BPF, implying that the blades do not behave the same way.

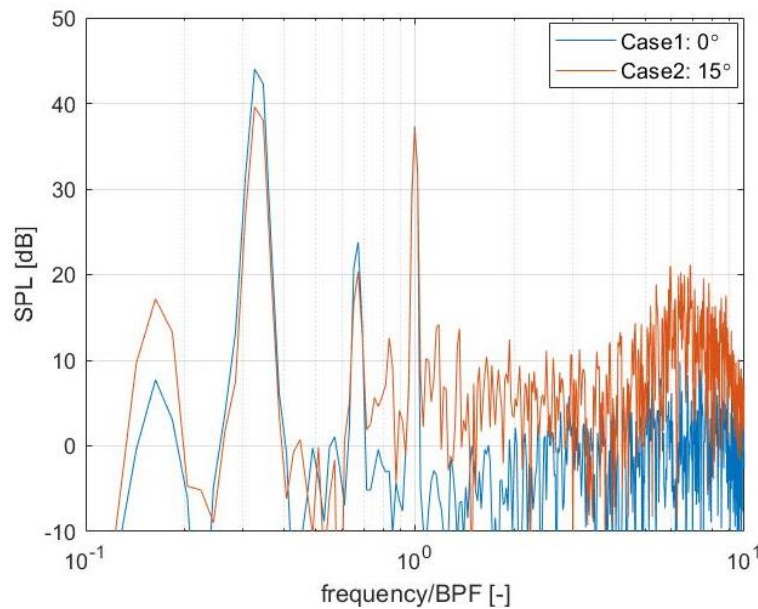


Figure 56. SPL frequency distribution between Case1 and Case2 along the propeller plane ($\theta=90^\circ$). Case 1 corresponds to a 0° angle for Blade 1 with respect to Y-axis, and Case2 corresponds to 15° , as shown in Figure 49.

The noise emission of the isolated propeller at different emission angles depicts a difference in the direction normal to the rotational plane between the resolution 200 and 150 voxels/ c_r (Figure 57). The increase of approximately 10 dB between the two resolution levels is attributed to the acoustic power increase across all frequencies. In these emission angles ($\theta=0^\circ$ and 180°), no tonal component is dominant, and thus, the noise level is determined by the broadband noise. Therefore, the observed increase between the Res=150 and 200 voxels/ c_r , should be associated with the vortex structures along the propeller axis, as the flow emitted by the blades are computed with enhanced accuracy in the high-resolution case (Res=200 voxels/ c_r). Nevertheless, the noise emission pattern at angles with range $[30^\circ, 150^\circ]$ show a converging trend as the curves corresponding to high-resolution levels overlap.

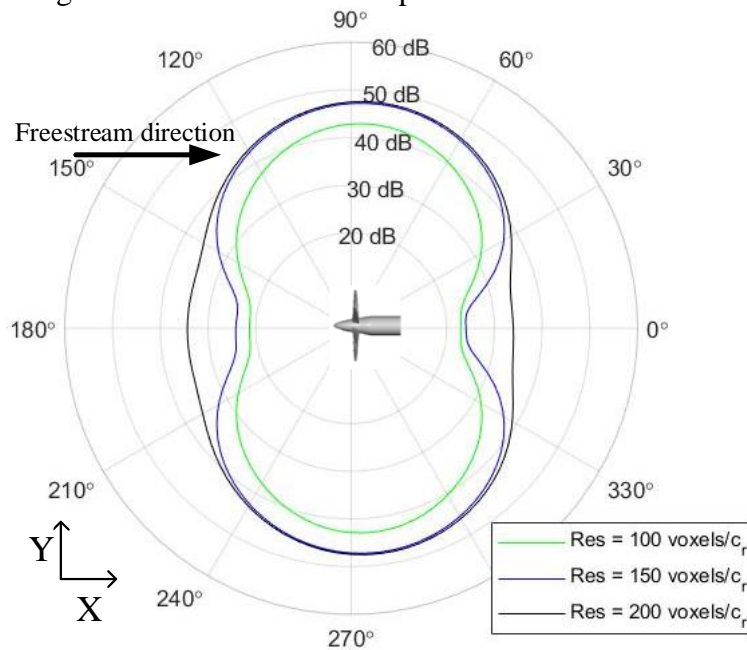


Figure 57. Noise emission angles along the XY plane in the far-field for different resolution levels. OSPL values correspond to the frequency range $[0-4460\text{Hz}]$ (up to 5th BPF).

4.2.1 Comparison between solid and permeable surfaces formulation

Before proceeding to the distributed-propeller model, it is interesting to examine the differences between the solid and permeable surface formulations. Since both surface formulations will be used in the distributed-propeller model, their examination, in the first place, will depict potential differences. The noise emission comparison between the two formulations is shown in Figure 58, based on the OSPL values. This figure

depicts the difference between the *OSPL* values by subtracting the *OSPL* values of the solid surface from the respective ones of the permeable surface. The low-frequency analysis (Figure 58a) shows enhanced noise emission levels (up to 10 dB) upstream and downstream of the propeller plane at angles 30°, 150°, 210° and 330°. The shape of the difference resembles a quadrupole, implying that the difference between the two surfaces is attributed to the quadrupole noise component. For high-frequency values, the difference between the directivity pattern of the two surface formulations is focused on emission angles equal to 100° and 260°, where the noise level enhancement in the permeable surface is up to 8.6 dB (Figure 58b). Since the implementation of the permeable surface formulation means that the integration of the pressure field takes place over a control surface, an additional noise term is considered compared to the solid surface formulation, i.e. the quadrupole term Eq. (1.18). Therefore, the vortical structures observed in Section 4.1 affect the resulting pressure field of the control surface. Based on the scaling law of the quadrupole term [45], the noise from these sources is scaled with the eighth power of the flow velocity (U^8) compared to the sixth power of the flow velocity (U^6) that the dipole sources are scaled. Since the quadrupole terms become dominant in near transonic regions, it is expected that the dipole contribution to be the dominant noise source, as the simulation Mach number is 0.36 in the present analysis. A spectral analysis is performed below to further examine the differences between the two surface formulations.

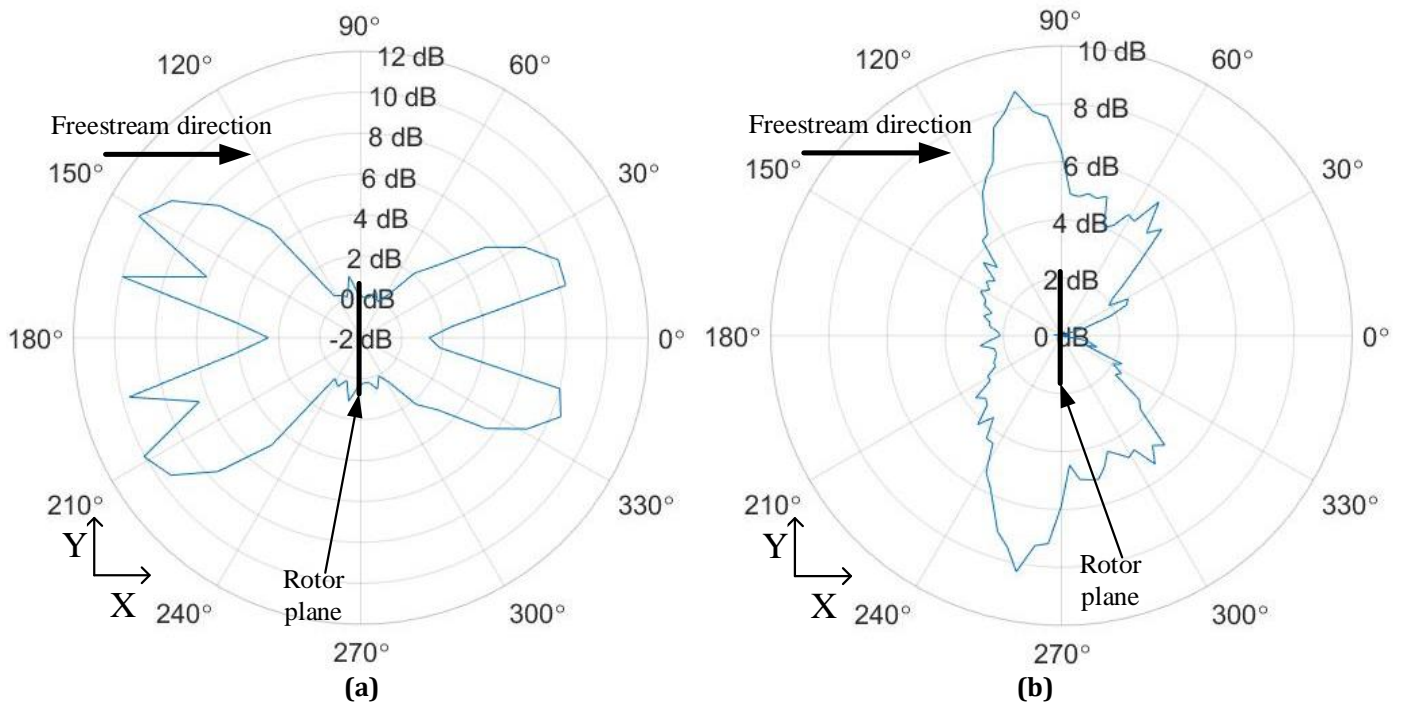


Figure 58. Difference of *OSPL* noise emission values between solid and permeable surface formulations for low-frequencies [0-4460Hz] (a) and high-frequencies [4460-8920Hz] (b) along the XY plane.

The comparison of the spectrum analysis for the two surface formulations is presented in Figure 59, referring to emission angles equal to $\theta=100^\circ$ and 150° , where the major discrepancies in far-field noise emission were observed. The major differences between the two formulations are noticed in the mid- and high-frequency components, around 5th and up to 10th BPF, respectively. The tonal components up to 4th BPF are observed in both emission angles for the permeable surface formulation, whereas they are underpredicted in the solid one. For the 100° emission angle (Figure 59a), all tonal components up to 5th BPF are enhanced compared to the corresponding values of solid surface, while the high-frequency components near 10th BPF are also augmented. This denotes that the increased noise emission values for the permeable surface formulation are a result of both tonal and broadband noise enhancement, with the power of the mid-frequency tonal components more dominant than the broadband ones. On the contrary, the increase along 150° emission angle is attributed to the increase of tonal components in the mid-frequency range (enhanced power of the 3rd and 4th BPF). The above analysis shows that the permeable surface provides a better overview of the noise components than the solid surface formulation. The prediction of tonal components in the mid-frequency range is associated with the propeller’s loading, while the enhanced broadband noise should be associated with the quadrupole term.

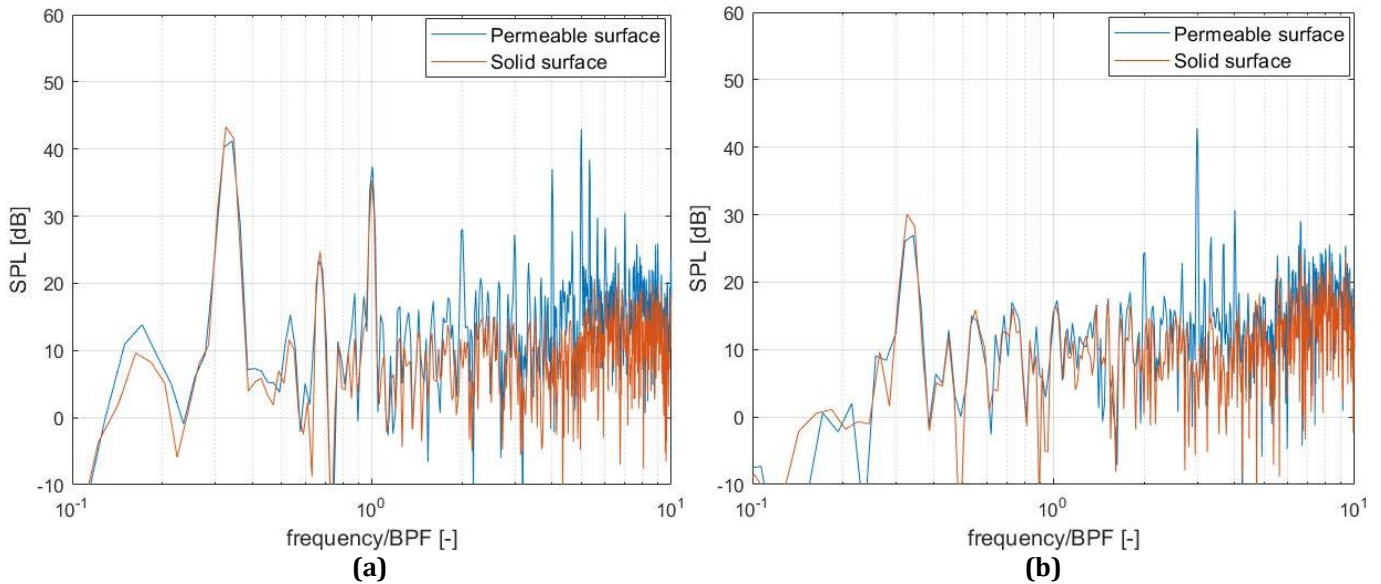


Figure 59. Spectrum analysis between solid and permeable surface formulations at azimuthal angles $\theta=100^\circ$ (a) and $\theta=150^\circ$ (b) based on Figure 58.

All in all, this comparison between the FWH analysis using solid and permeable surface was not performed to prefer one surface over the other but to achieve a vital analysis of the isolated propeller as an initial step for the distributed-propeller model. The analysis of the distributed-propeller case requires both formulations for the acoustic assessment to consider both the pressure fluctuations on the blades and the acoustic interference between adjacent vortical structures.

The resolution study presented above for the isolated-propeller model showed that a grid-independent solution was achieved in both aerodynamic and aeroacoustic analysis. The aerodynamic investigation showed that a thrust coefficient convergence had been accomplished for medium ($Res=150$ voxels/ c_r) and high-resolution ($Res=200$ voxels/ c_r), as can be proven by the thrust coefficients values (relative change less than 0.5%) and distributions along the blade-span. Similarly, the aeroacoustic emission has been converged for the same level of resolution, as the tonal noise component at 1st BPF along the propeller plane has changed by less than 0.5 dB. Therefore, the resolution level that is being used for the analysis of the distributed-propeller model is equal to 200 voxels/ c_r .

4.3 Distributed-propeller model: Comparison with experimental data

In this section, the performance of the distributed-propeller model will be compared with the experimental data. In this model, the resolution of 200 voxels/ c_r is used, as it was considered sufficient for the isolated-propeller model. The comparison of the thrust coefficients of both numerical data using PowerFLOW and experiments is shown in Table 8. It is evident that there is a discrepancy between the values of the experiments and the simulations, with error values reaching 6.6% and 4.9% in the isolated- and distributed-propeller cases, respectively. Although the error is within reasonable limits, it can be related to the non-uniform behaviour of all six blades due to the different azimuthal locations wrt to the Cartesian axis, as discussed in a previous section. Also, experimental misalignments of the configuration, differences in the geometry of the blades and flow conditions could lead to minor deviations between numerical and experimental data.

Table 8. Time-averaged thrust coefficients (T_c) of isolated- and three-propeller cases computed numerically in PowerFLOW and experimentally.

	PowerFLOW	Experiments	Error (%)
<i>Isolated propeller</i>	0.43207	0.46246	6.57
<i>Distributed propellers</i>	0.43241	0.45448	4.86

The difference in performance can be shown by the upstream conditions measured at the Inflow plane (Figure 60a), which is located 10% of the diameter upstream of the rotor plane. Both axial and

tangential velocities determine the inflow conditions, measured in different directions, as shown in Figure 60b. Axial and tangential velocities are measured for propeller #1 while its blades are approaching (-30°), are retreating (30°) and are at the horizontal plane (0°).

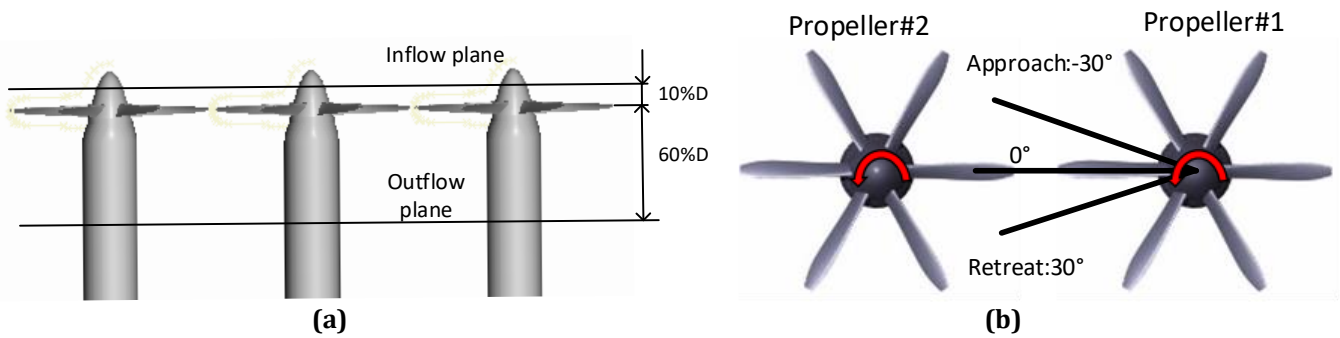


Figure 60. Measurement locations upstream and downstream from the propeller (a). The orientation angles used to measure the velocity distributions in the upstream direction are shown in the right figure(b).

Figure 61 depicts the comparison between the axial velocities of experimental and numerical data in the upstream direction (inflow plane in Figure 60a). Looking at parts of the blade that are located inboard ($r/R < 0.8$), there are discrepancies between the experimental and numerical curves. The experimental curves are higher than the respective numerical curves in all three different directions, presenting higher peak values. The same behaviour was observed in the isolated propeller (section 4.1) and was related to the reduced induced effects by the slipstream due to the low thrust compared to the experiments presented in Table 8. Both numerical and experimental curves present the same trend at the outboard sections ($r/R > 0.8$), especially at the region between the propeller tips at a 0° angle. In parallel, tangential velocities present many similarities in both experimental and numerical data in all directions. There are slight differences between the numerical and experimental curves, but the curves show the same trend. This trend shows a change in the behaviour of the tangential velocity. The non-zero tangential velocity with the change in sign with respect to the horizontal axis is related to adjacent propellers that affect the flow field upstream of the propellers, inducing velocity components. An in-depth analysis of this behaviour will be discussed in Chapter 5.

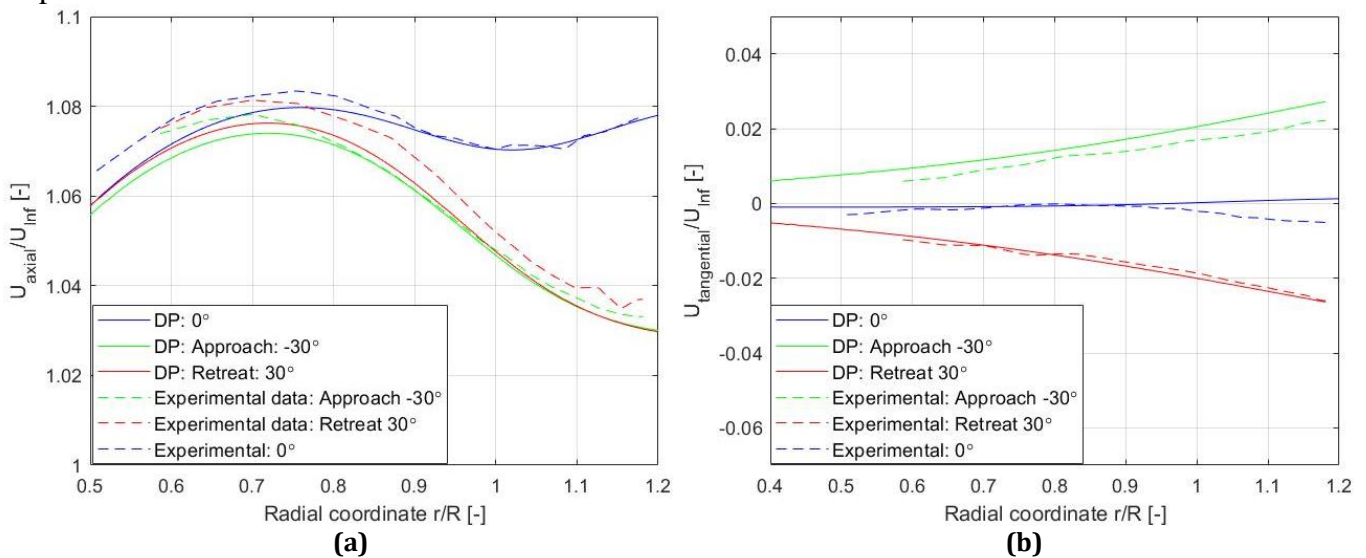


Figure 61. Normalized time-averaged axial (a) and tangential (b) velocity distributions of the distributed propellers comparing the numerical and experimental data in the upstream direction ($X/D = -0.1$).

The comparison of the wake flows between the experimental and numerical curves shows similarities and differences. Figure 62 shows the comparison of the experimental and numerical data for the axial and the tangential velocity distributions measured at the outflow plane (see Figure 60a). The axial velocity curve corresponding to the numerical model shows decreased values at inboard sections compared to the experiments, similarly to the isolated propeller. Subsequently, the axial velocity curve of the numerical data presents higher values than the experimental ones at the outboard sections ($r/R > 0.8$) due to the outboard blade loading. Further outboard ($r/R > 1$), the velocity curves have a similar trend as the axial velocity

increase. This increase is attributed to the wake flow of the adjacent propeller. Regarding the tangential velocity, the experimental and numerical curves have the same behaviour near the tip and at the outboard sections. The similarities in the behaviour of both the experimental and numerical curves provide the necessary confidence on the model to investigate further and analyse the resulting data.

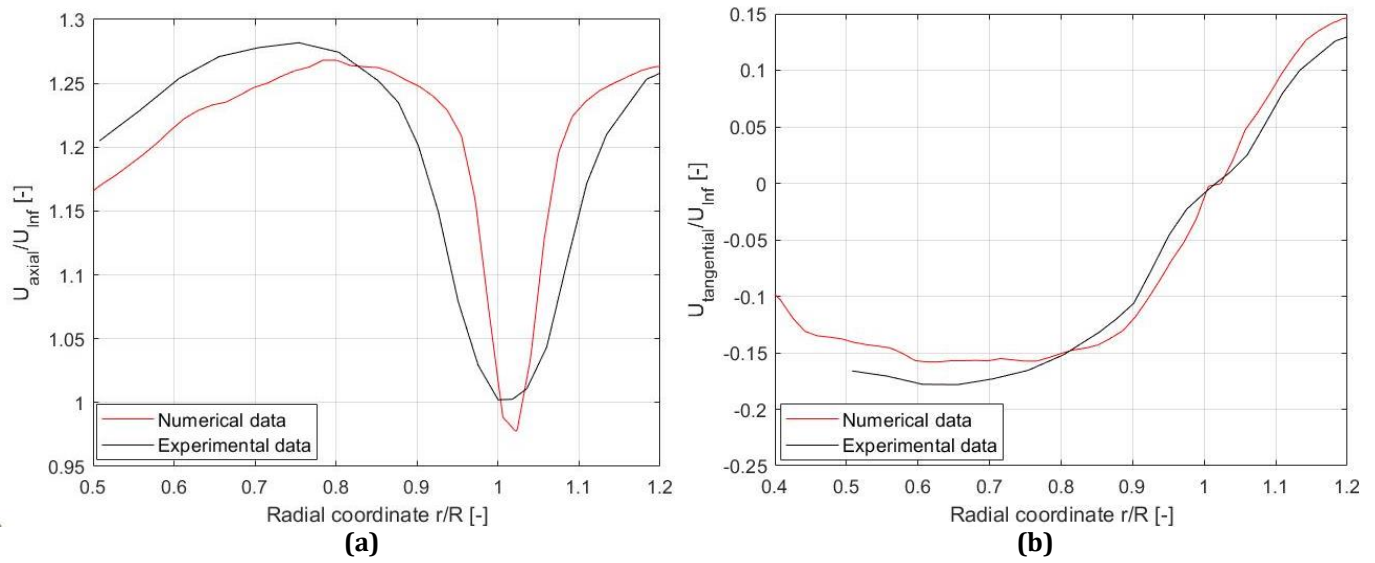


Figure 62. Normalized time-averaged axial (a) and tangential (b) velocity distributions of the distributed-propeller case comparing the numerical and experimental data of the wake in the downstream direction ($X/D=0.6$).

5

Aerodynamic Analysis

The following chapter presents the aerodynamic investigation for the distributed-propeller cases. The case that will be examined at first is the baseline configuration, where the separation distance of two adjacent blades is 2% of the diameter (Figure 28). The effects of the propeller array are examined by comparing the performance of the isolated propeller with Propeller#1 of the distributed-propeller (DP) case as well as the flow field changes. Also, the last section of the current Chapter (Section 5.2) refers to the effects of the relative phase angle between adjacent propellers presenting the changes in aerodynamic behaviour of the model compared with the baseline case.

5.1 Aerodynamic performance of the baseline configuration

In this section, the aerodynamic performance of the distributed-propeller system is presented, examining both the thrust coefficient and the flow field. Figure 63 illustrates the thrust coefficient (T_c) time-evolution corresponding to Propeller#1 (propeller in the middle) of the DP system compared to the respective values of the isolated propeller. The time-averaged performance of Propeller#1 is slightly affected, as its thrust coefficient presents a slight increase compared to the isolated-propeller case from $T_c=0.4321$ to 0.4325. Simultaneously, the standard deviation value of the thrust coefficient in the DP system is equal to 0.0011, while the respective value for the isolated propeller is near zero ($2.8e-5$). This is related to the occurring oscillations of the thrust coefficient for the baseline case, as shown in Figure 63. In the three-propeller case, the thrust coefficient fluctuates remarkably compared to the isolated propeller, which is stable. A thrust reduction was expected in a time-averaged perspective, as mentioned in [8] and [9], where up to 5% reduction in thrust was observed. In these studies, the standard deviation of the thrust coefficient is 0.008 and 0.001, respectively. The underprediction of the standard deviation value in the numerical model [8] compared to the experimental one [9] was attributed to “interactions with the test stand” not captured in the simulation. The resulting value in the present analysis is similar to the respective value of the numerical analysis in [8], showing a common trend to the literature findings. Regarding the time-averaged performance of the propeller, the non-uniform behaviour of the blades needs to be considered. Table 9 presents the comparison of the time-averaged T_c values between Blades1, 2 and 3 for both the isolated propeller and Propeller#1 of the DP system. It is noticed that the three blades behave inconsistently, with the T_c value for Blade1 remaining approximately the same with the isolated propeller, while a slight decrease (0.11%) for Blade2 and an increase (0.24%) for blade3 are observed. As a result, the time-averaged thrust coefficient of Propeller#1 shows an increase (0.09%) compared to the isolated propeller.

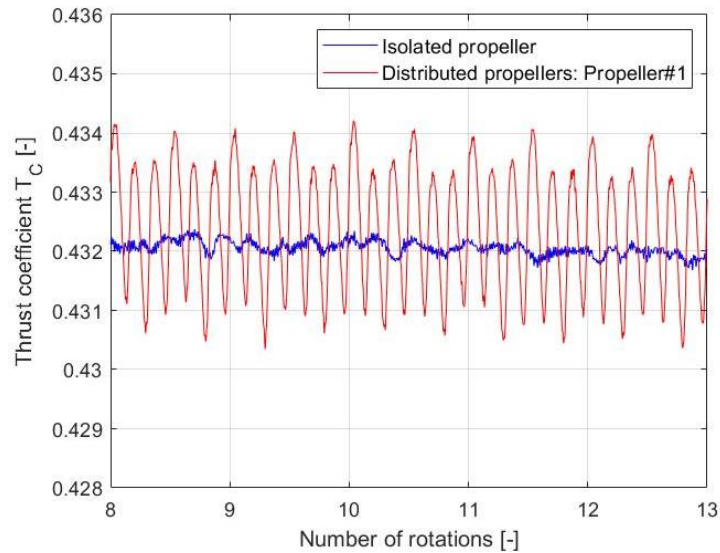


Figure 63. Time-evolution of thrust coefficient (T_c) for both the isolated-propeller and the baseline case

Table 9. Time-averaged thrust coefficient (T_c) values comparison between the isolated-propeller and distributed-propeller models.

	T_c (DP)	T_c (Isolated Propeller)
Blade1	0.0765 ± 0.001	0.0765
Blade2	0.0689 ± 0.001	0.0690
Blade3	0.0708 ± 0.001	0.0706

In the time evolution plot (Figure 63), the fluctuating thrust coefficient curve periodically appears two peak values higher than the other peaks during a single propeller revolution. Figure 64 presents the time-evolution of thrust coefficients for the three blades of Propeller#1 as well as the propeller's thrust coefficient. It is observed that the propeller's thrust coefficient peaks take place at the same time as the peaks for blade 1. Thus, the peak values of the propeller's thrust coefficient curve are repeated twice per revolution, corresponding to the peaks of Blade 1 and blade 4. The performance of Blades 1, 2 and 3, also illustrated in Figure 64, depicts the same behaviour with the isolated propeller, as explained in Section 4.1. Nevertheless, all blades appear fluctuating thrust curves, which clearly show thrust's unsteady behaviour.

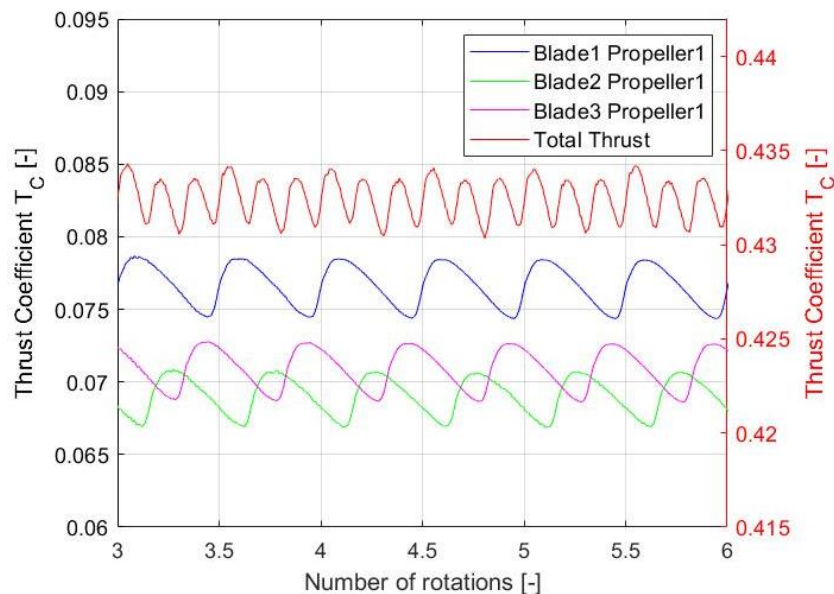


Figure 64. Time-evolution of thrust coefficients for each blade. Propeller's thrust coefficient is also shown on the right vertical axis.

5.1.1 Mean flow field analysis

The existence of multiple propellers operating in close proximity has affected the mean flow field of the DP system. In Figure 65, the mean flow velocity contours are depicted for the isolated propeller and the

distributed-propeller model. The velocity is normalized by the free-stream velocity. The mean flow contours depict a change in axial velocity magnitude as the areas with high velocities in the distributed-propeller case decrease. As the flow of Propeller#1 travels downstream, the slipstream approaches the adjacent flows extending its radial cross-sectional area, as shown in the circled area in Figure 65b. The radial contraction of the slipstream in the isolated-propeller case downstream of the rotor is absent for the three propellers case. On the contrary, the flow behind Propeller#1 bends towards the adjacent wake flows of the other two propellers, as can be noticed in the mean flow field. The extension of the flow field is evident at a streamwise position equal to $X/D=0.6$ and further downstream. The high-velocity areas in the far-field are extended from $Y/D\sim 0.45$ in the isolated propeller to $Y/D\sim 0.5$ in the distributed propeller model, which implies a flow interference.

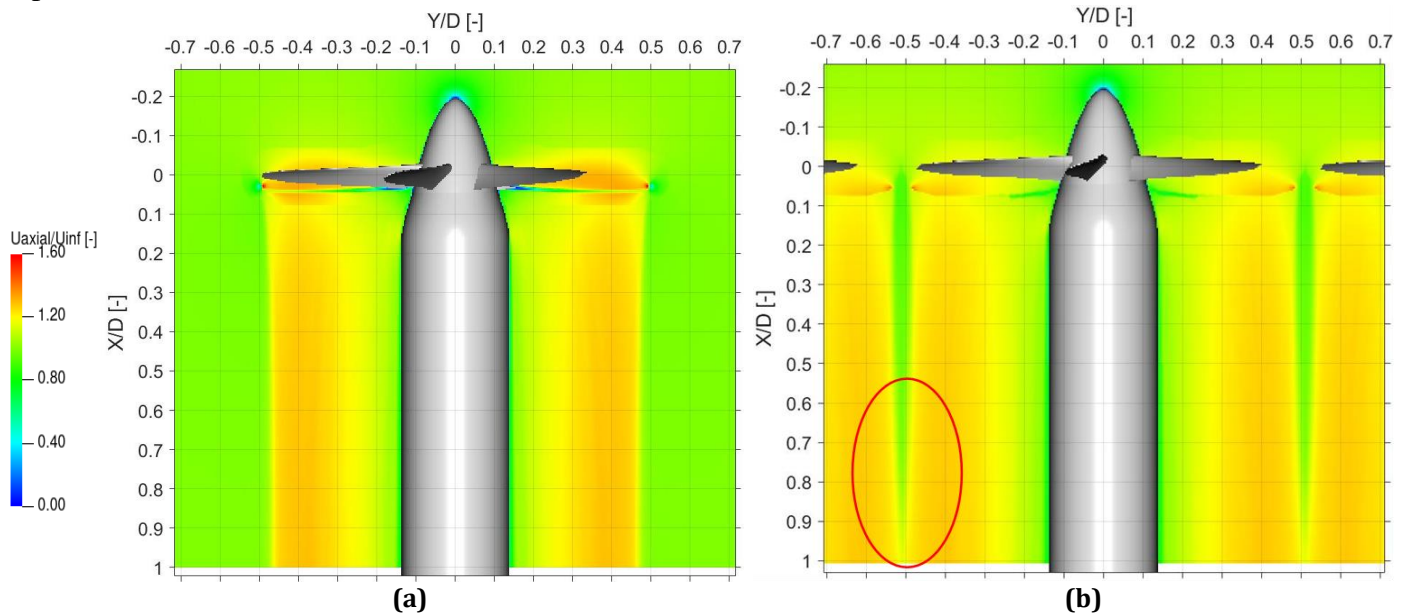


Figure 65. Axial velocity contour of the mean flow field for the isolated-propeller case (a) and the distributed-propeller configuration (b). The normalized values are relative to the free-stream velocity. The slipstream extension is annotated with red colour.

The velocity in the upstream directions is directly related to the thrust generation of the system. Axial and tangential velocities of the isolated and three propellers are compared in Figure 66. An increase in axial velocity in the region between the propellers is observed combined with a change in tangential velocity. In 0° orientation (based on Figure 60b), the axial velocity slightly declines near the tip of Propeller#1, but then it grows due to Propeller#2. On the contrary, the axial velocity approaches free-stream conditions further outboard from the blade tip during approach and retreat. The comparison with the isolated propeller reveals an increase of the axial velocity component in all directions. In parallel, tangential velocity appears to change direction in approach and retreat, as implied by the change in sign in Figure 66. At 0° , no tangential component appears as expected since the propeller does not induce swirl in the upstream direction. This behaviour of the tangential component affects the thrust coefficient curve, contributing to the oscillating performance of the thrust. The change in tangential velocity sign does not alter the time-averaged thrust coefficient, as the local effect of the negative and positive tangential components will be averaged during a single rotation of the propeller, with no effect on the mean value. The increase in axial velocity components and the change in tangential velocity are attributed to the vortex system downstream of the propeller, which induces upstream velocity components, as will be explained below.

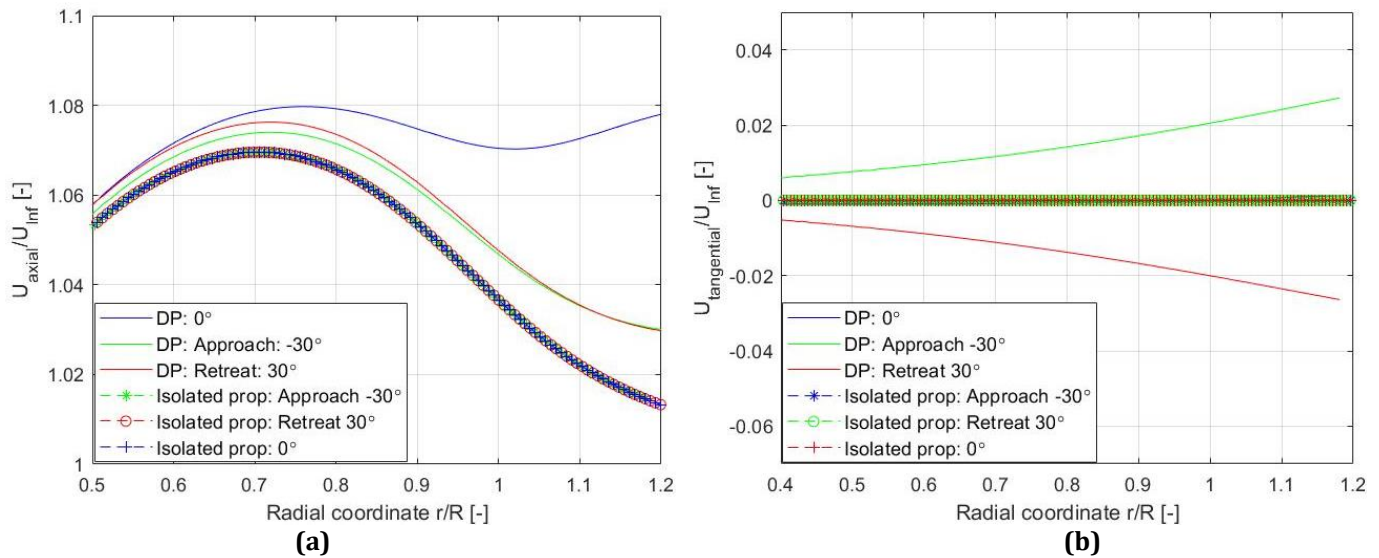


Figure 66. Comparison of normalized time-averaged axial (a) and tangential (b) velocities between the isolated-propeller and the distributed-propeller case in the upstream direction ($X/D=-0.1$). Velocity components are measured in the three orientations, as shown in Figure 60.

The implementation of the vorticity tube model (as described in Section 2.1.3) reveals the induced effects upstream of the propeller. Using Biot-Savart law, the axial and radial velocity components can be calculated and presented in Figure 67. There is a gradual acceleration of the axial flow that starts upstream of the propeller, while inside the vorticity tube, the continuous distribution of circular vorticity sheets creates a gradient along the axis, which induces a uniform axial velocity within the cylinder [14], in accordance to momentum theory. The radial velocities induced by the vorticity tube model seem to be highest at the propeller plane, while its effect upstream and downstream is reducing. Therefore, the vortex system of a propeller modelled by a vortex tube induces radial and axial velocity components both in the upstream and downstream directions. Figure 67 also depicts the axial velocity distribution at a distance equal to 10%D upstream of the propeller. For comparison, the axial velocity distribution for the isolated propeller is plotted. The wake model shows a nice trend with the curve from the CFD analysis, where the curve smoothly drops near the propeller's tip and further outboard, where the induced axial velocity is near zero. The difference at the inboard sections ($r/R < 1$) is attributed to the assumption of the wake model, that the vorticity emanates from the tip. Had the vorticity from each blade segment been considered, the curve at the inboard sections would approximate the actual distribution.

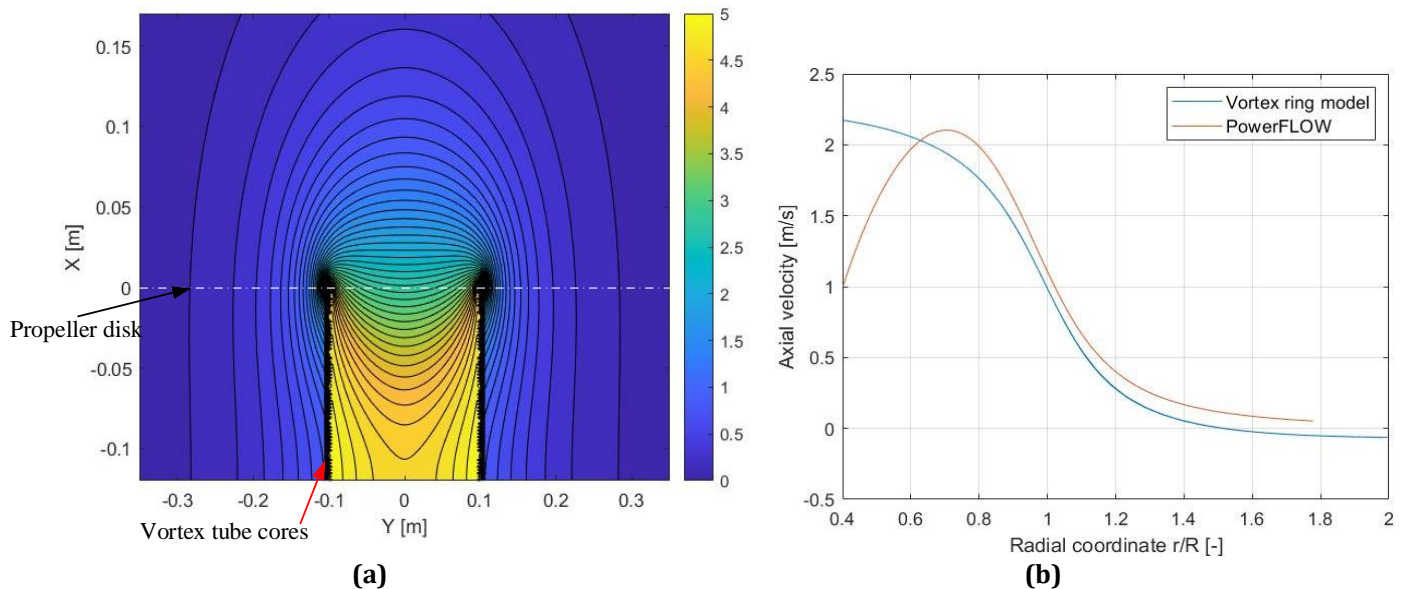


Figure 67. Velocity contour based on the semi-infinite vorticity wake tube model (a). Induced axial velocity comparison between CFD analysis and the vorticity tube model (b) upstream of the propeller at $X/D=-0.1$.

This model can also be applied in the case of distributed propellers. In an array of propellers operating in close proximity, the induced velocities by the adjacent propeller will alter the flow field upstream of the rotational plane. Figure 68 depicts the induced velocity on point P, which is located upstream of the propellers in a plane with angle θ to the horizontal plane ($Z=0$) and distance $R+r$ from Propeller#1 axis. Point P is located in the region between propeller #1 and #2 with radial distance from Propeller #2 equal to $R+r_l$. The induced velocities from Propeller#1 are denoted with black coloured vectors and the respective velocities from Propeller#2 with green. Therefore, the total axial velocity is the summation of the induced axial components from the adjacent propellers ($V_{ind,x}$). As a result, the axial component upstream of the propellers is increased, as shown in Figure 66. At the same time, the two components along the radial direction contribute to the induced $V_{ind,\theta}$. The out-of-plane induced velocity $V_{ind,\theta}$ is illustrated in Figure 69, where it is evident that there is a vertical velocity component to the radial direction.

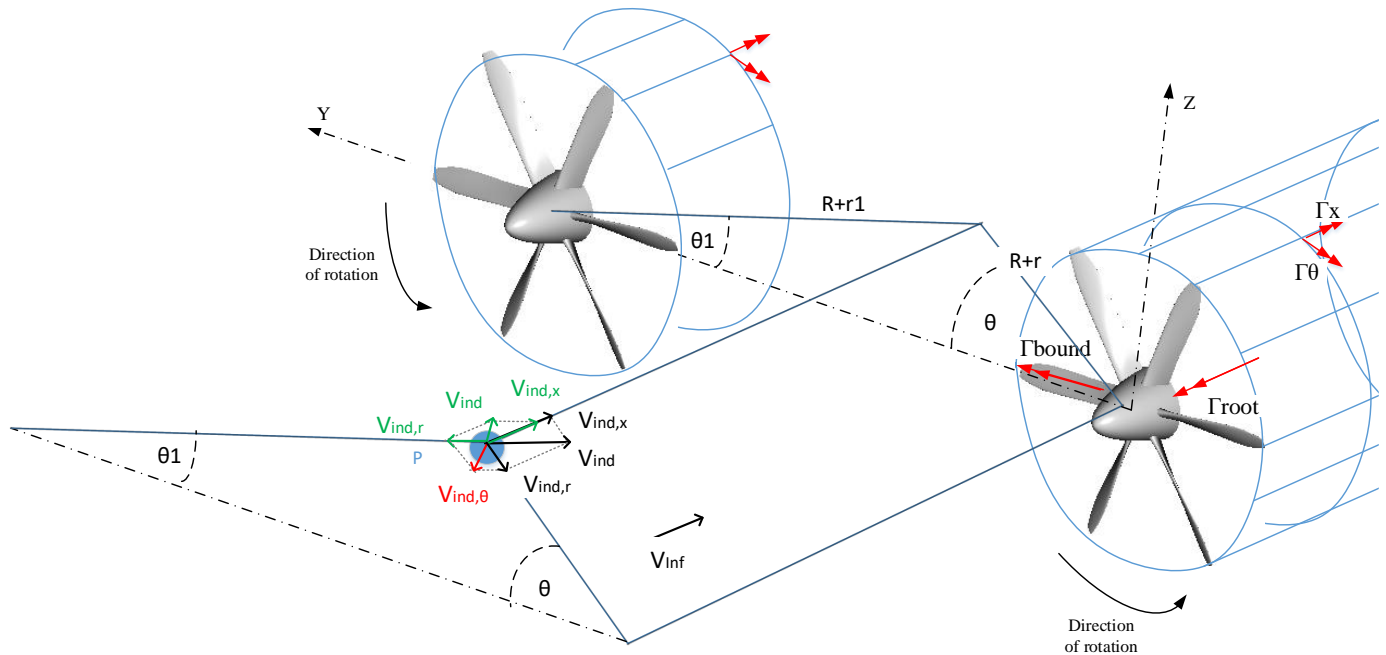


Figure 68. Sketch of the induced velocities on a point P upstream of propellers. The induced velocities from Propeller#1 are shown with black colour and green the induced velocities from Propeller#2.

Figure 69 illustrates the induced velocities on point P by the adjacent propellers. Above the horizontal axis (for $Z>0$), it is evident that the flow, apart from the radial components, has a vertical component, making the flow travel downward. Below the horizontal axis ($Z<0$), there is a reverse in the flow direction, and the vertical component is now directed upwards. Along the horizontal axis ($Z=0$), the radial components are of opposite direction, and, thus, no tangential velocity is induced. This change in the sign is the reason for the change in the tangential velocity. So it can be concluded that the existence of an adjacent propeller leads to non-radial velocity components associated with the change in tangential velocity signs and as a result of the thrust oscillations. It is also essential to notice that this behaviour will not be affected by the direction of rotation or difference in the phase angle between the propellers in a time-averaged sense. Thus, the effect of induced velocities upstream is attributed to the separation distance between the adjacent propellers. In the case of large distances, the induced velocities from adjacent propellers can be neglected, and thus the effects of induced velocities are negligible.

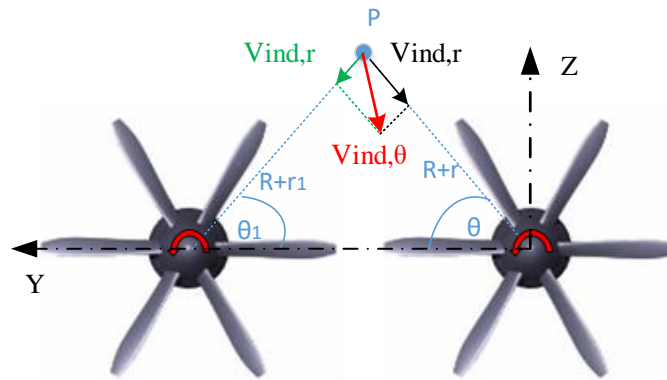


Figure 69. Induced velocities on a point P located above the Y-axis between the two propellers. The total induced velocity has a component normal to the radial direction that is directed downwards.

As mentioned before, the increase in the axial velocity upstream of the propellers is attributed to the induced axial velocity components by the adjacent propeller. However, the induced effect along the propellers plane is different. The vorticity tube model shows that the induced effect on axial velocity along the propeller plane is minor. This is proven by the velocity distribution outside the propeller disk, as the axial velocity component is near zero. Similarly, de Vries, et al. [11] showed that no axial velocity is induced on the propellers plane, but it is the nacelles that play a major role in the axial velocity increase. The dominant effect on thrust loss is, thus, attributed to the blockage effect caused by the nacelles [11]. In the present analysis, though, no thrust loss was observed in the baseline model, and still, the increase in axial induced velocities was nicely identified. Thus, although the adjacent propellers induced axial velocity components upstream of the propellers, this increase has no impact on the propeller's performance.

5.1.1.1 Loading distribution

The examination of loading distribution will provide additional details on how the multiple propellers affect the performance. The difference of the thrust distribution per segment ($\delta T_c = T_{c,prop} - T_{c,iso}$) between the isolated propeller and Propeller#1 denotes the performance changes (Figure 70). In Figure 70, the symmetry in thrust distribution of the isolated propeller is broken, and a varying thrust distribution occurs in the case of the distributed propellers. As the blades of Propeller#1 approach the side propellers, there is a reduction in thrust until it reaches the minimum distance from the adjacent propeller at the horizontal plane (along the Y-axis), while during the retreat, there is an enhancement of thrust. For Propeller#1, the same process is repeated twice in one revolution, i.e. when the blades approach and retreat Propeller#2 and #3. Other studies ([10] and [8]) have shown similar behaviour of the propeller during its rotation. It is most remarkable that the changes in thrust take place near the blade tip, outboard of thrust peak location at $r/R \approx 80\%$. These local changes in thrust at blade tips are not related to the time-averaged analysis presented above, as the decrease and increase in thrust are symmetric and, thus, they will not affect the time-averaged propeller's performance. However, this behaviour is related to the unsteady interference between the propellers that will be mentioned later.

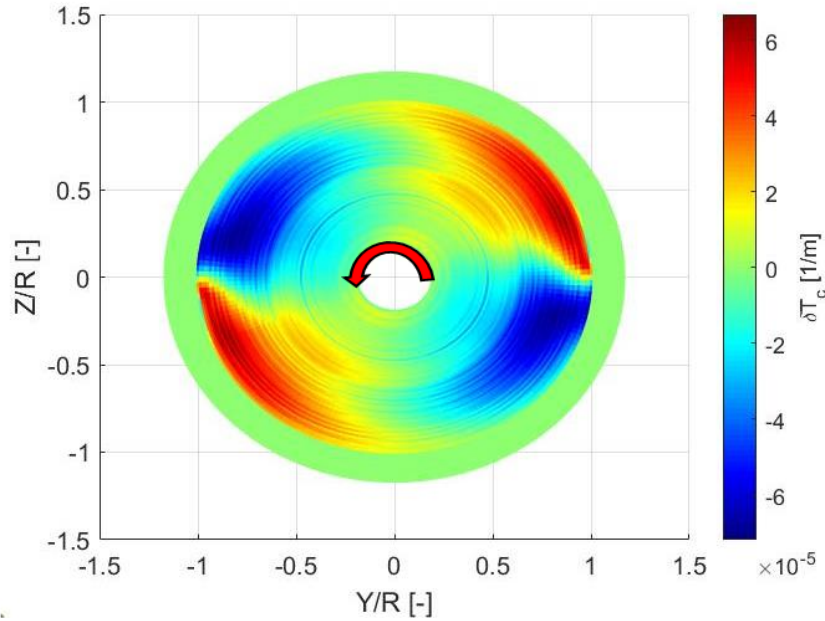


Figure 70. Thrust distribution difference (δT_c) at rotor disk plane between Propeller#1 of the baseline case and the isolated one.

Contrary to Propeller#1, Propeller#2 experiences this thrust variation only once per revolution. The respective graph with the difference of the thrust coefficient distribution between Propeller#2 and the isolated propeller (δT_c plot in Figure 71) illustrates that the reduction and the subsequent increase in thrust take place at the positive of the Y-axis ($Y/R > 0$) near Propeller#1.

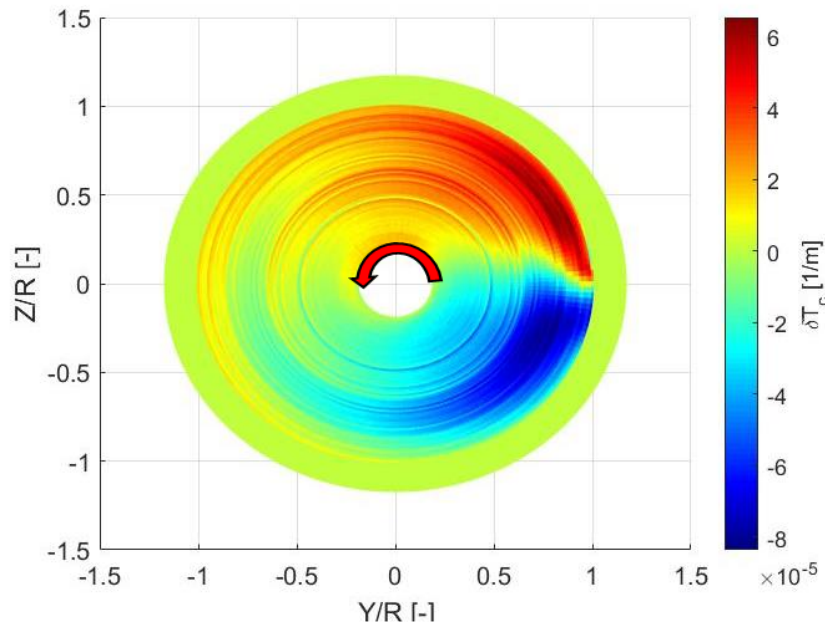


Figure 71. Thrust distribution difference (δT_c) at rotor disk plane between Propeller#2 of the distributed-propeller model and the isolated one.

5.1.1.2 Slipstream analysis

The change in the thrust along the blade span will eventually affect the slipstream of the distributed-propeller system. The changes in the slipstream are illustrated via the total pressure coefficient (“pressure jump” - $C_{p,total}$) defined in Eq. (3.1).

$$C_{p,total} = 1 + \frac{P_{total} - P_{total,\infty}}{q_\infty} \quad (3.1)$$

Where $p_{total,\infty}$ is the total free-stream pressure and q_∞ is the dynamic pressure of the free-stream flow.

It is measured at a plane located at 10% of the diameter downstream of the rotor, as shown in Figure 72. The $C_{p,total}$ distribution is symmetric in the slipstream of the isolated propeller, while in the baseline model, this symmetry is broken. In particular, the “pressure jump” distribution has the same trend as the thrust loading, with a reduction in pressure distribution as the blades approach the adjacent propellers and a subsequent increase during the retreat. This is shown in Figure 73, where the total pressure difference between

distributed propellers (both Propeller#1 and #2) using the index: $\frac{\Delta C_{p,total}}{C_{p,total_iso}} = \frac{C_{p,total} - C_{p,total_iso}}{C_{p,total_iso}}$.

Additionally, there is an obvious slipstream deformation in the region between the propellers. The flow at the slipstream of Propeller#1 (middle propeller in Figure 72) bends inboard as the blades approach the adjacent ones and then is curved outboard as it retreats. The slipstream of the adjacent propellers deforms in a similar way, though anti-symmetrically to the middle propeller.

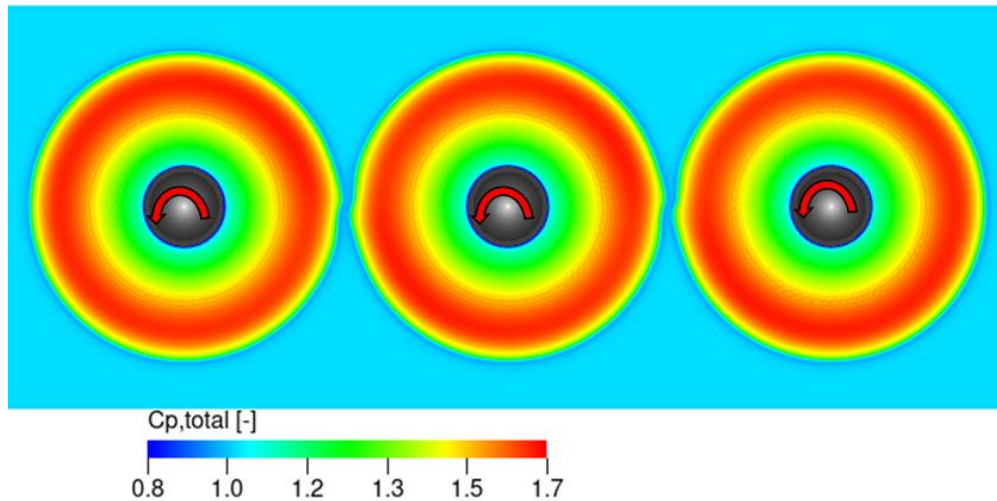


Figure 72. Total pressure coefficient distribution in the slipstream at $X/D=0.1$ of the distributed-propeller case. The red arrows show the direction of rotation.

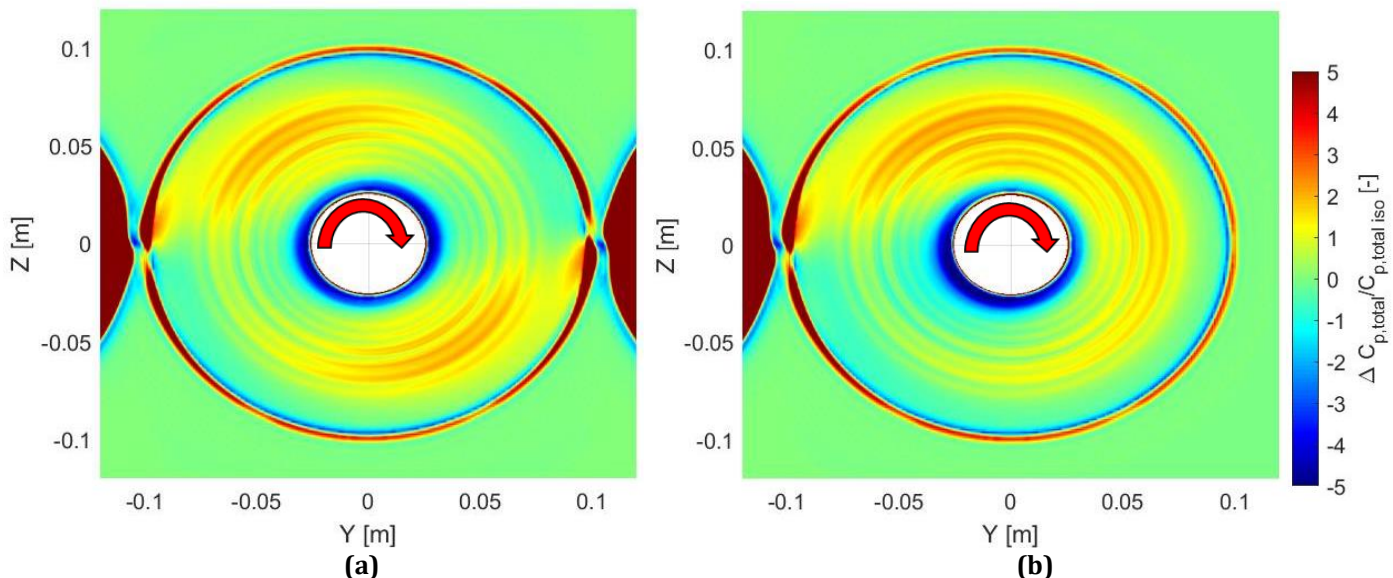


Figure 73. Total pressure differences ($\Delta C_{p,total}/C_{p,total_iso}$) between the isolated propeller and Propeller#1 (a) and Propeller#2 (b) measured at $X/D=0.1$. The red arrows show the direction of rotation.

The evident change in the wake shape due to the deformation alters the radial contraction of the slipstream in the distributed propellers. The slipstream of Propeller#1 in the DP system is extended further outboard compared with the isolated propeller, as depicted in the axial velocity distribution measured at $X/D=0.6$ (Figure 74a). The axial velocity presents lower values at inboard sections ($r/R < 0.8$) of the baseline model than in the isolated propeller, with a decrease of up to 1%. The slipstream extension is evident further outboard ($r/R > 0.8$) due to the increased axial velocity values up to 4% at $r/R=0.95$. A similar level of

reduction at inboard sections was also noticed in the experimental study [11], and it was related to the slight reduction in thrust. This thrust reduction is, though, not observed in the present analysis. Therefore, the reduced axial velocity values at the inboard section are attributed to the distribution of axial momentum at a wider area than in the isolated propeller. Compared to the isolated propeller, the tangential velocity component does not seem to be affected inboard or outboard of the propeller (Figure 74b).

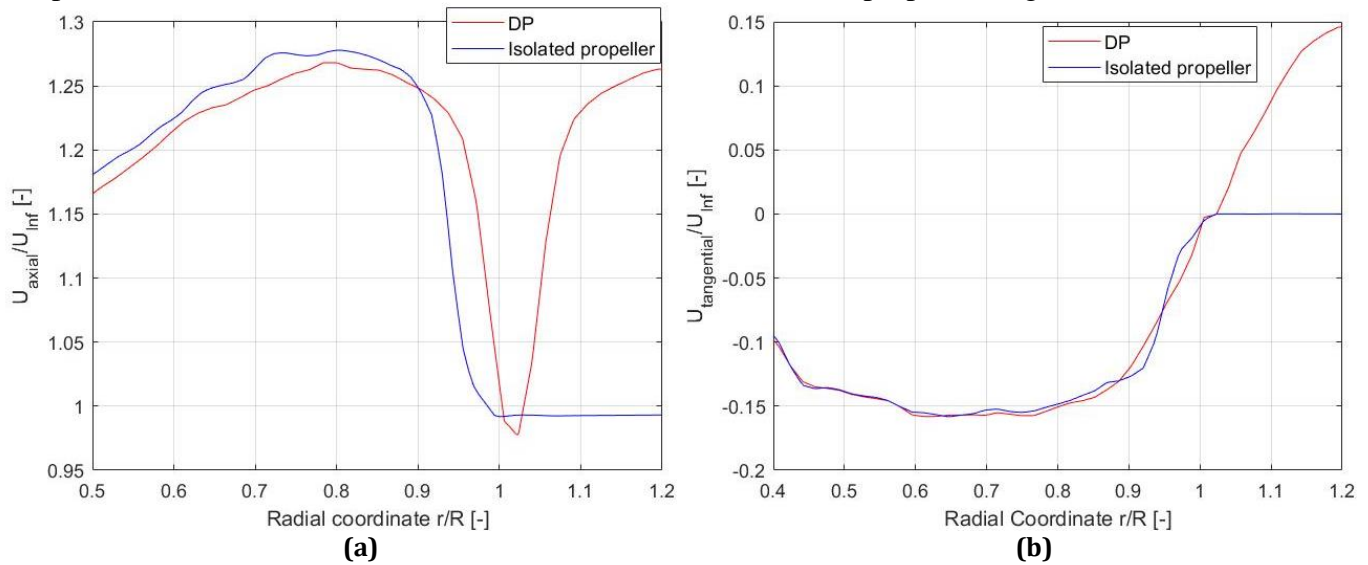


Figure 74. Comparison of normalized time-averaged axial (a) and tangential (b) velocity distributions between the distributed-propeller case and the isolated propeller. The measurement location is downstream of the propellers at $X/D=0.6$.

5.1.2 Vortex field

The instantaneous flow field will provide data on the wake development and vorticity distribution for the three-propeller model to analyse the interference between the propellers. For this reason, phase-locked averaging analysis is implemented based on the instantaneous flow field of the propeller's rotation. In the present section, the vortices being shed by the propellers are visualised using the out-of-plane vorticity values along the XY plane, where all three propellers are located.

Figure 75 illustrates slices of the out-of-plane vorticity based on the phase-locked analysis. The generation and development of shear layers and the tip vortices are captured satisfactorily, enabling the description of their motion and the comparison between the isolated- and distributed-propeller models. Regarding the shear layers at the inboard sections of the blades, there is no remarkable change in their evolutions between the two cases. The motion of the tip vortices, though, differs in the case of the DP system. As tip vortices travel downstream, their radial location stays approximately constant at $Y/D \sim 0.5$, whereas the isolated propeller has an evident radial contraction as the tip vortices move towards $Y/D \sim 0.45$. The position of the vortex cores for both the isolated- and distributed-propeller cases proves that there is no contraction in the distributed-propeller model, as can be seen in Figure 76. The vortex location was computed based on the phase-locked data by visually tracking the vortex core motion along the XY plane at different frames. The deviation between the isolated propeller and the baseline model is pronounced at the downstream locations, as the radial displacement is equal to 6.8% of the radius compared to the isolated propeller at $X/D=0.9$.

Additionally, as presented in Figure 74a, the low axial velocity is also verified in the vorticity contour. In the far-field of the isolated propeller, vortex E1 has reached the streamwise location $X/D \sim 0.8$, while the respective vortex in the distributed-propeller case has almost reached $X/D \sim 0.75$. In parallel, the vortex cores' size is expanded along the X-axis, losing its circular shape as a result of the neighbouring vortex. This change in vortex shape is attributed to the induced effects between the adjacent vortices, discussed in the section below. Further downstream, it is noticed that the vortices dissipate faster than the isolated propeller, as the shape of the vortex F1 has entirely changed as a result of the interaction between the neighbouring structures. Similar observations are found in [9] and [10], where tip vortices in downstream locations lose their structure faster than isolated propellers.

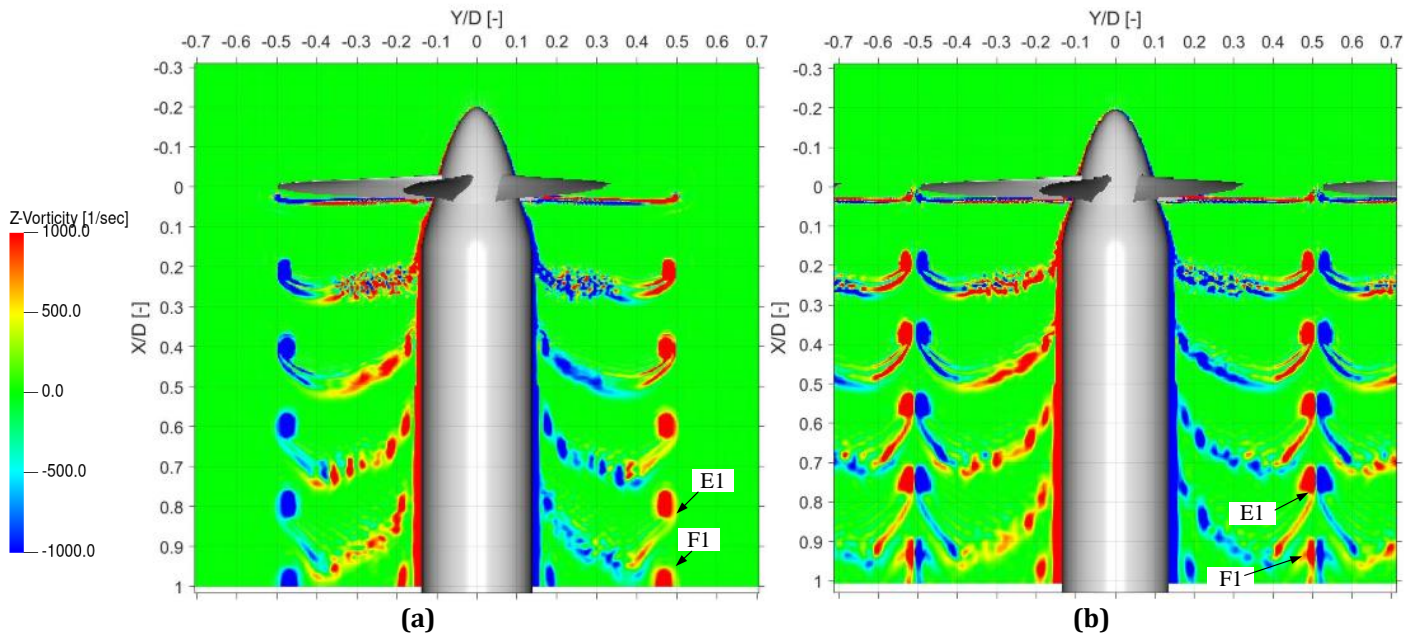


Figure 75. Out-of-plane vorticity contours for the isolated-propeller case (a) and the distributed-propeller configuration (b). Tip vortices are annotated in downstream locations.

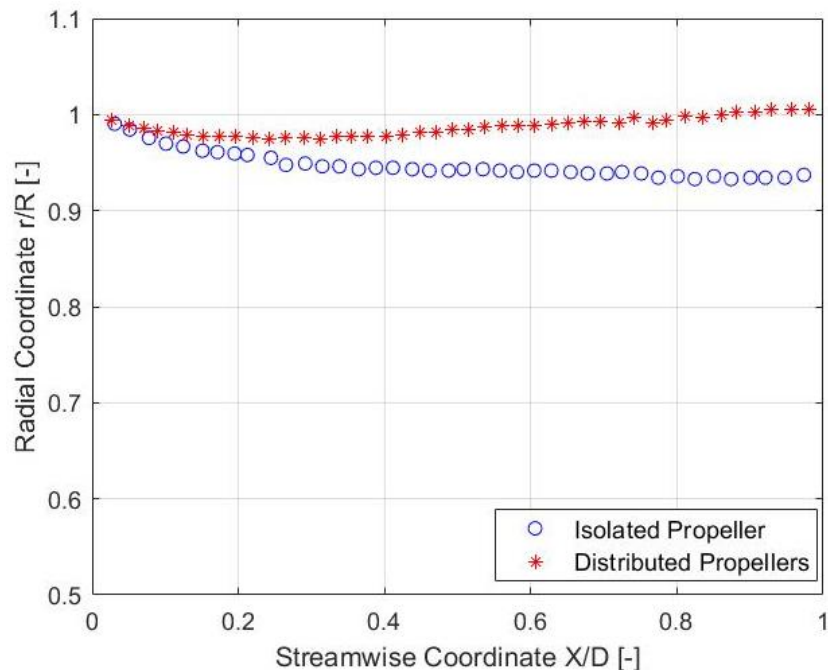


Figure 76. Vortex core trajectory comparison for the isolated propeller and distributed propellers. The vortex cores has been tracked based on their location as shown in Figure 75.

5.1.2.1 Induced effects between adjacent vortices

This section presents the analysis of the interference between adjacent vortices by examining the induced velocities between the adjacent flow structures. The 3D visualization of the vortices being produced by the propeller is achieved using the λ_2 criterion. The λ_2 criterion is based on the eigenvalues of the quadratic summation of the symmetric and antisymmetric part of the velocity gradient tensor [46]. Figure 77 depicts the phase-locked vortex core isosurface of λ_2 criterion coloured with the axial velocity values. The value of the criterion is equal to $-3.5 \cdot 10^6 \text{ 1/s}^2$.

The oblique view of Figure 77a shows the curvature of the vortex core isosurface in the near- and far-field. It is observed that as the flow travels downstream, its interference with adjacent flow structures is more evident than in the near field. This is related to the increased effects of viscous forces downstream of the propeller, which eventually results in the diffusion of the slipstream. Nevertheless, the front view of the propellers (Figure 77b) illustrates the change in the slipstream and its deformation right after one blade

passes the adjacent one. This deformation of the vorticity will induce a change in the blade's performance, i.e. in the loading distribution, contributing to the unsteady loading, as will be discussed afterwards.

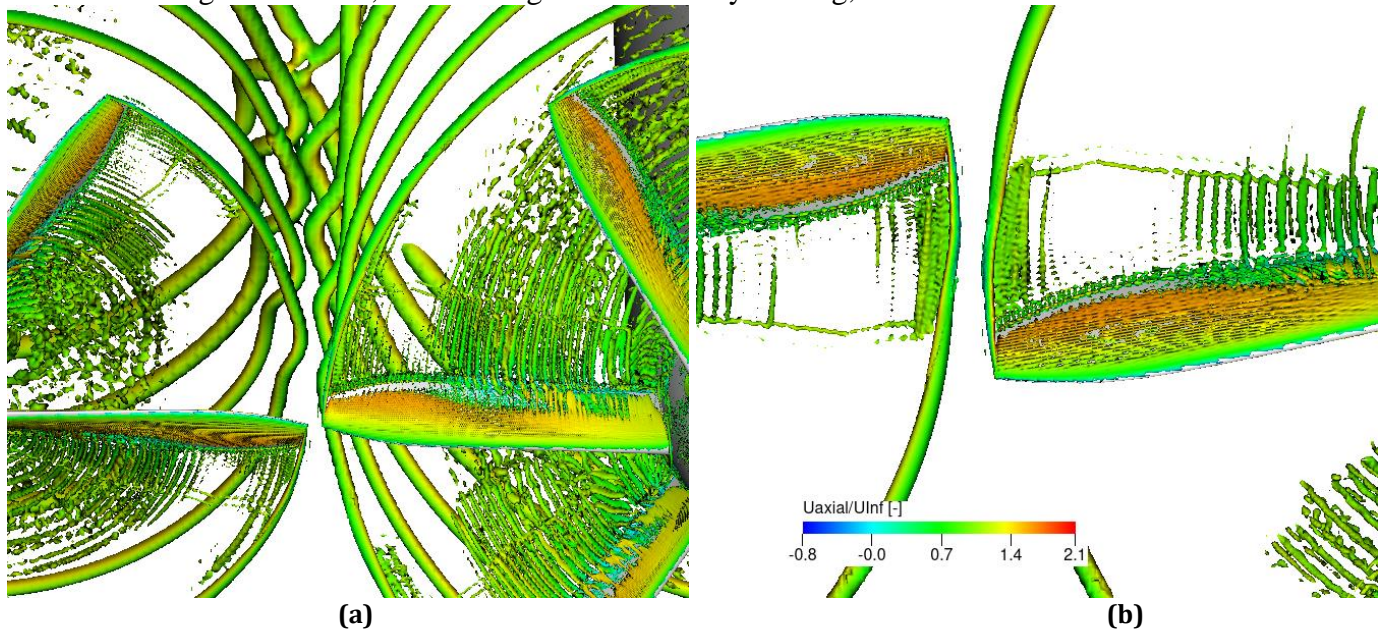


Figure 77. Isosurface views of the λ_2 criterion ($\lambda_2 = -3.5 \times 10^6 \text{ 1/s}^2$) visualising the vortex cores between the propellers (a). Zoom in view at the area between adjacent blades as they rotate in their nearest distance (b).

The induced velocity components between two adjacent vortex filaments are presented in Figure 78, where two points, P1 and P2, are located along these vortex filaments in the XY plane. Each vortex filament induces velocity components along the X-axis and the θ -axis (see vortex tube model) on the adjacent points. The induced velocities in the 3D view along the streamwise and tangential axis are shown in Figure 78 (right side). Overall, the vorticity of Propeller#1 Γ_1 induces at point P2 velocity V_{indP2,Γ_1} which is oblique to (XYZ) Cartesian system, while Propeller#2 Γ_2 induces at point P1 velocity V_{indP1,Γ_2} . Thus, it is easier to describe the induced velocities in 2D view along the Cartesian axis, as shown in Figure 79a. Since $\Gamma_{1,x}$ and $\Gamma_{2,x}$ vorticities are directed backwards in both propellers, the induced velocities are in opposite directions, as shown in Figure 79a. Propeller#1 induces $V_{indP2,\Gamma_1,z}$ in point P2 with the direction along the positive Z-axis and Propeller#2 induces $V_{indP1,\Gamma_2,z}$ in the opposite direction. This results in a deformed vortex shape resembling a “shear” deformation, as shown in the vorticity contour (Figure 79b). The resulting deformation of two adjacent vortex cores justifies the induced effects as presented using the sketched Figure 79a. In a time-averaged perspective, the direction of the induced velocity components results in the slipstream deformation observed in Figure 72. P1 tends to travel downwards towards the negative Z-axis, and combined with the opposite motion of the P2; it leads to the local deformation of the vortical structures. Therefore, the slipstream deformation depicted in both the mean flow (Figure 72) and instantaneous contour (Figure 77), is attributed to the induced effects of the neighbouring vortex filaments.

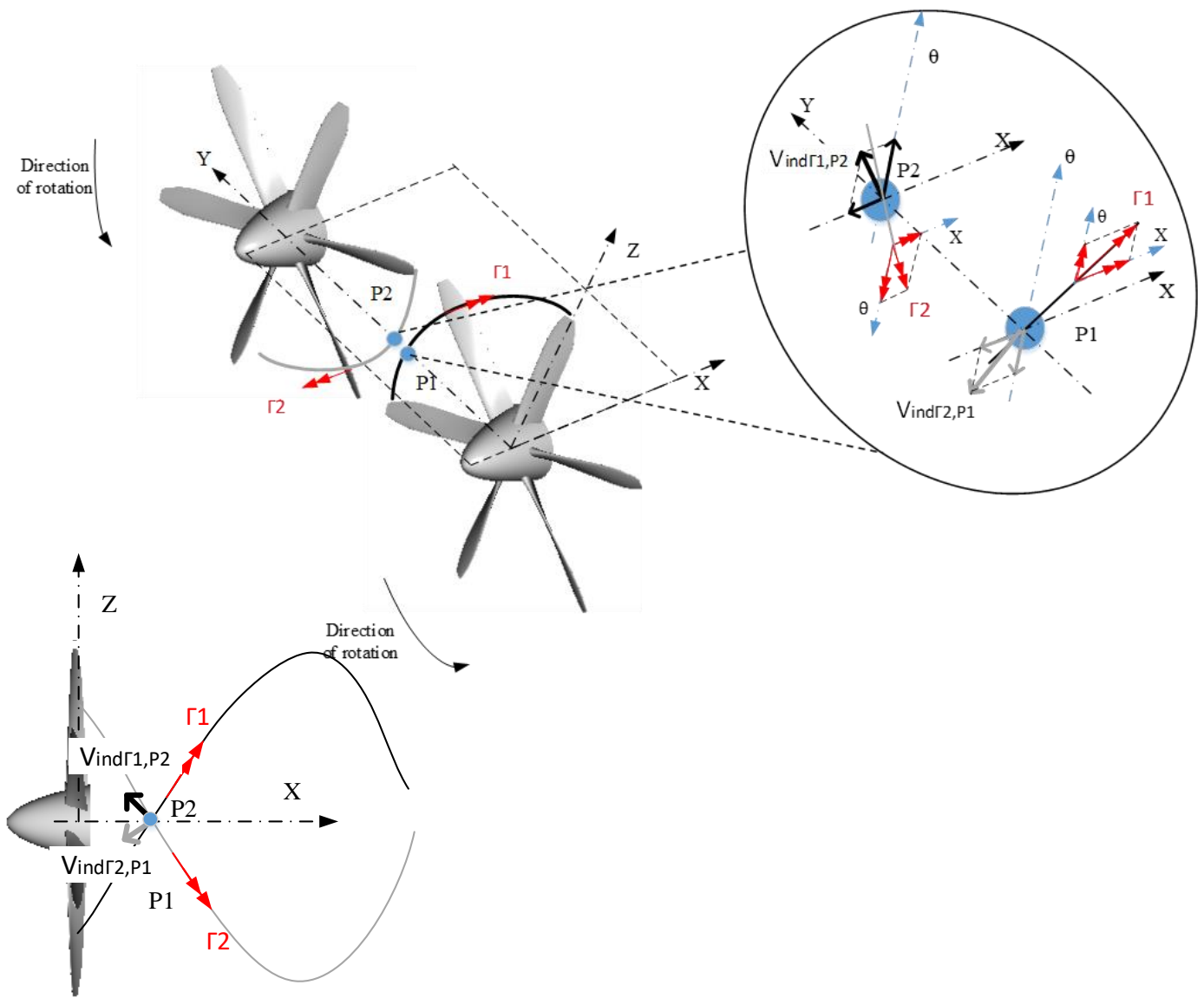


Figure 78. Sketch view of the induced velocities between adjacent vortex filaments. Zoom-in view (top right corner) shows the induced velocities between two points of adjacent vortices along the XY plane. The resulting induced velocities are in 3D space (see the sketch in the bottom left corner).

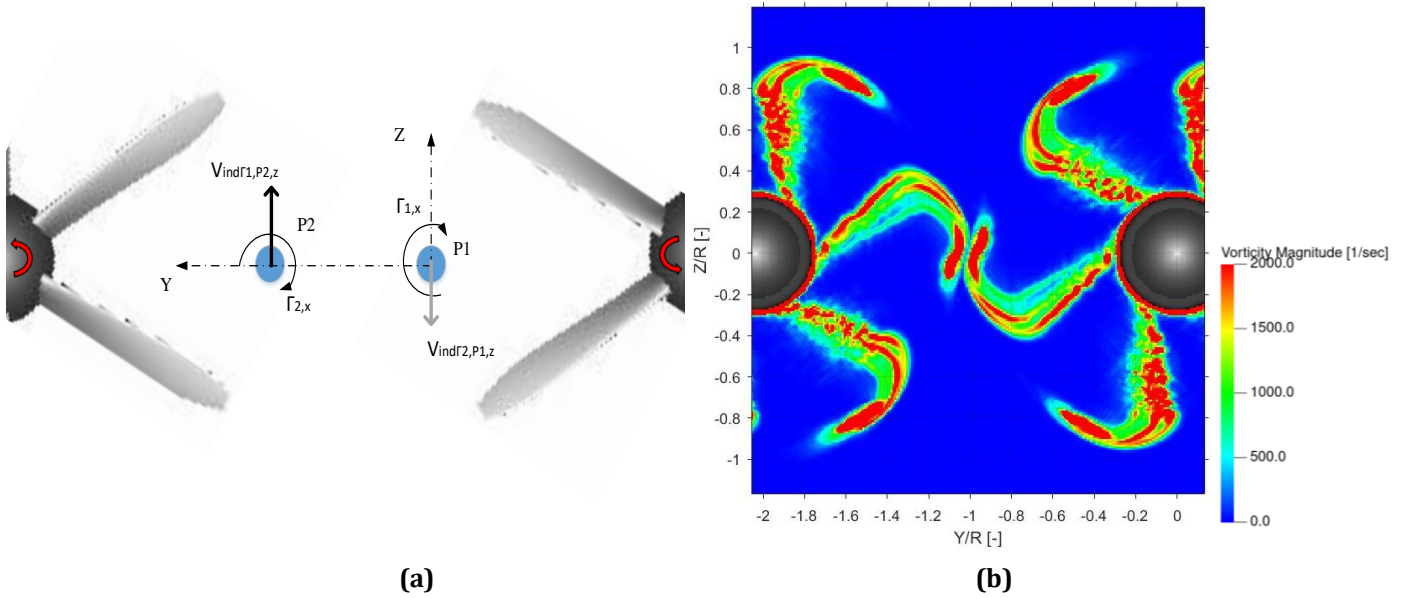


Figure 79. Front view sketch of the induced velocity along the Z-axis from the axial components of the free vorticity (a). The vorticity magnitude contour is shown in the right figure at location $X/D=0.3$ downstream.

The vorticity components of the vortex filaments along the Z-axis (Figure 80a) contribute to the extension of the vortex core along the X-axis. The induced velocities ($V_{indP2,\Gamma_{1,x}}$ and $V_{indP1,\Gamma_{2,x}}$) are opposite to the convective axial velocity downstream. The adjacent vortex cores show major deformation in a direction opposite to the downstream motion only in the region between the propeller, i.e. when the two filaments are at the nearest distance, as observed in the 3D view of Figure 80b. As a result, the induced effects are sensitive to distance with decreasing contribution at great distances. Thus, the effect is dominant when the adjacent vortices are in the nearest distance, with a partial contribution to axial velocity reduction and dominant effect to the expansion of the vortex core size, observed in the out-of-plane vorticity contour in Figure 75.

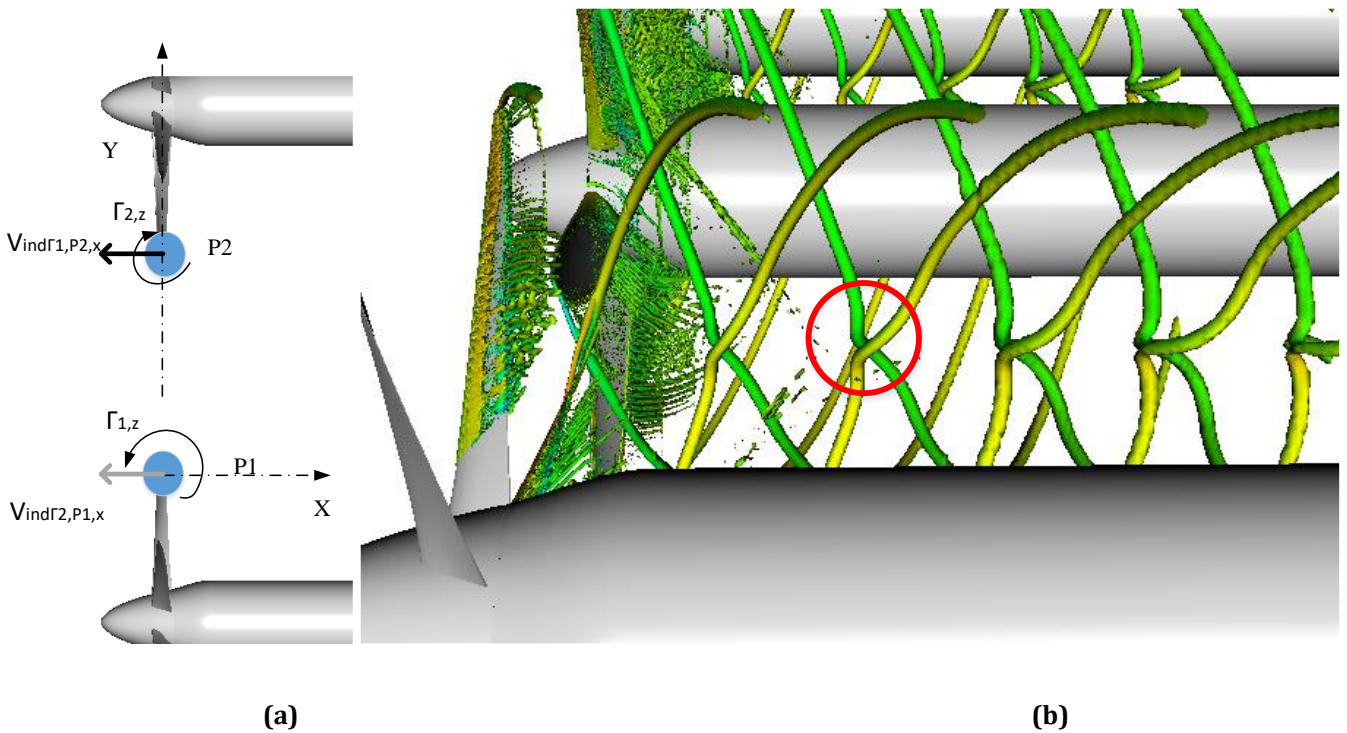


Figure 80. Top view sketch of the induced velocities along the X-axis from the Z-axis components of the free vorticity (a). Isosurface 3D view of the vortex filament deformation along the X-axis denoted inside the red circle (b).

5.1.3 Unsteady loading

Now that the interference between adjacent vortical structures has been presented, it is insightful to consider their effects on the propeller's performance. The induced velocities between the adjacent vortices do not alter the performance in a time-averaged sense, only locally, as the blades pass from this region. Thus, as two blades of a co-rotating system of propellers with zero relative phase angle approach each other, the induced effects grow and become noticeable, especially at the tip of the blades. The evolution of the thrust coefficient of Blade1 of Propeller#1 is depicted in Figure 81. Figure 81a shows the thrust coefficient difference between the DP system and the isolated propeller at different azimuthal angles during the rotation of Blade1. Blade1 in the distributed-propeller system experiences a noticeable change in thrust twice per revolution at 0° and 180° . The unsteady loading reduces as the blade approaches the intermediate area between the propellers and increases as it retreats. As a result, thrust oscillations in Blade1 of Propeller#1 has an amplitude of 5.35% of the mean thrust coefficient of Blade1 of the isolated propeller (Figure 81b). Despite the difference in time-averaged performance between blades, the amplitude of the unsteady components for all blades has the same value.

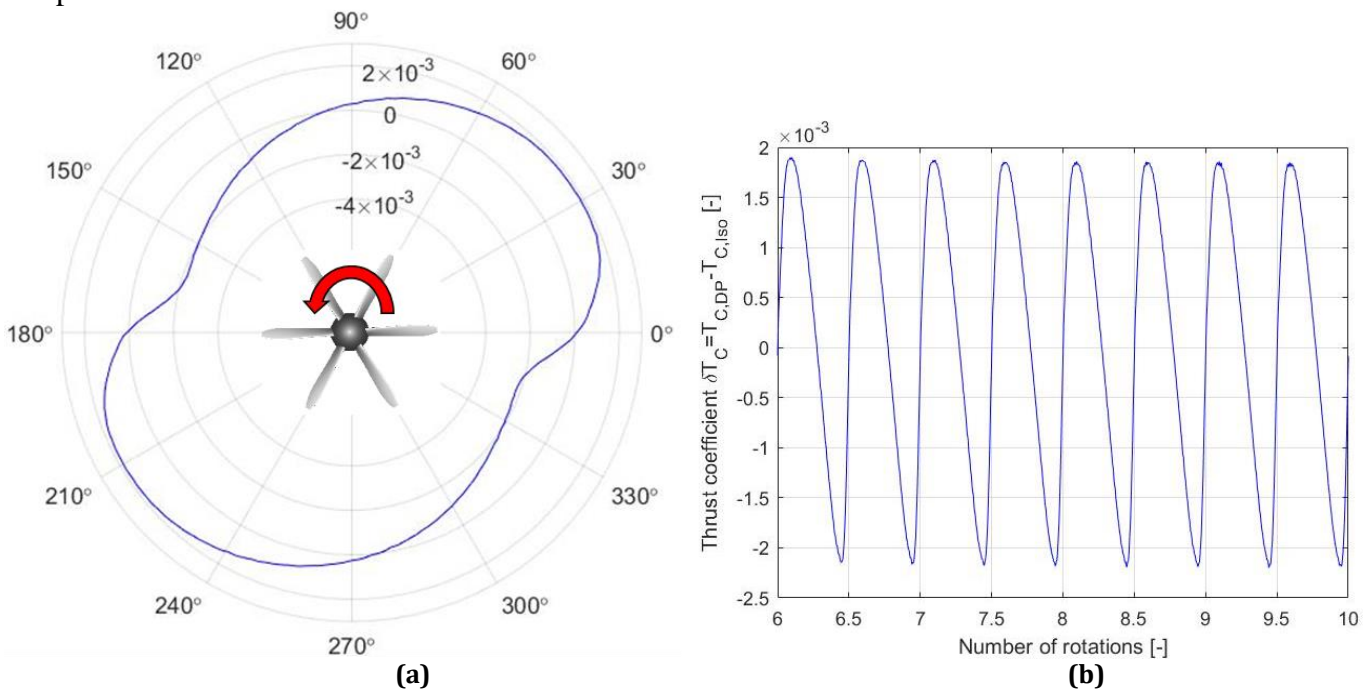


Figure 81. Variation of the thrust coefficient difference of Blade1 between the isolated propeller and Propeller#1 with respect to the azimuthal position during its rotation (a). Time variation of the same thrust coefficient difference of Blade1, indicating the unsteady thrust coefficient component (b).

The variation of thrust denotes the unsteadiness of the loading as a result of the induced effects between two neighbouring blades. Figure 82 shows how the thrust coefficient distribution of Blade1 in Propeller#1 changes as it passes through the region between the propellers. The change in thrust is noticeable at the outboard sections of the blade. Specifically, as the blade approaches the adjacent propeller, at azimuth angle $\Phi=161^\circ$ (Figure 81a), there is a thrust reduction, compared to the distribution at $\Phi=180^\circ$. On the contrary, there is an enhancement of thrust distribution as the blade retreats at $\Phi=200^\circ$. The change in thrust distribution is also depicted in the standard deviation of the thrust coefficient distribution along the blade span. This distribution denotes the unsteady thrust component per segment as the mean value has been subtracted. The evident change in thrust dominantly takes place outboard of the maximum loading location at radial position $r/R=0.85$. This result shows that the induced effects by the adjacent propeller change the loading distribution on the blades, affecting dominantly the area near the blade tip.

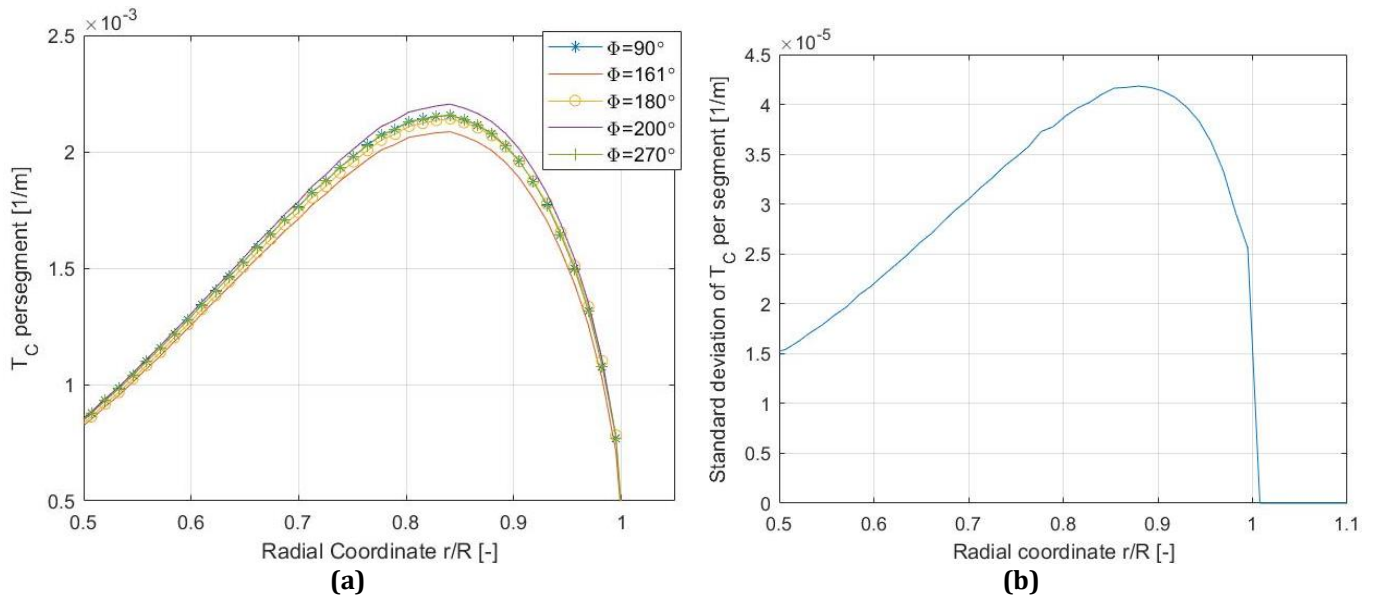
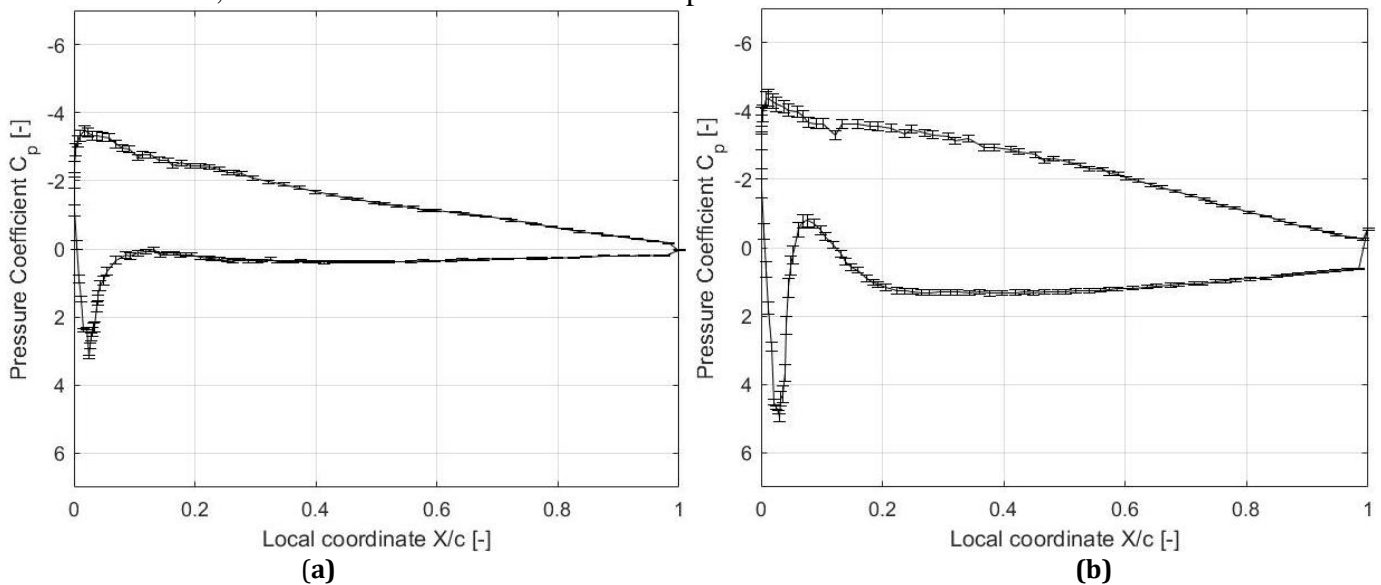


Figure 82. Thrust coefficient distribution along Blade1 at different azimuthal positions (a). The standard deviation of the thrust coefficient distribution during the blade's rotation (b).

5.1.3.1 Surface Pressure Fluctuations

The unsteady loading due to the induced effects is evident through the pressure fluctuations across the blade span. Figure 83 depicts the mean pressure coefficients across the blade span combined with the range of pressure values, denoted by the error-bar lines, during the blade rotation. The unsteady surface pressure values are depicted through the error-bars, indicating the range of pressure values, i.e. the difference between the maximum and minimum pressure on the blade throughout a revolution. Near the blade tip (Figure 83d), the pressure values present an enhanced range than the respective ones at inboard sections. The standard deviation at blade tip at $Y/R=0.975$ reaches 0.2091 while it is reduced at inboard sections, namely at $Y/R=0.7$ it is 0.0997. The increase of standard deviation values close to the blade tip implies that the unsteady effect is dominant in this region, attributed to the interference between the blades during approach and retreat. Observing the evolution of the errorbars along the C_p curves, it is noted that the range of values presents an increasing trend near the leading edges, i.e. at suction peak and up to 50% of the local chord length. The fluctuations of forces over a blade surface due to fluctuating surface pressure are dominant acoustic sources, as will be discussed in the next Chapter.



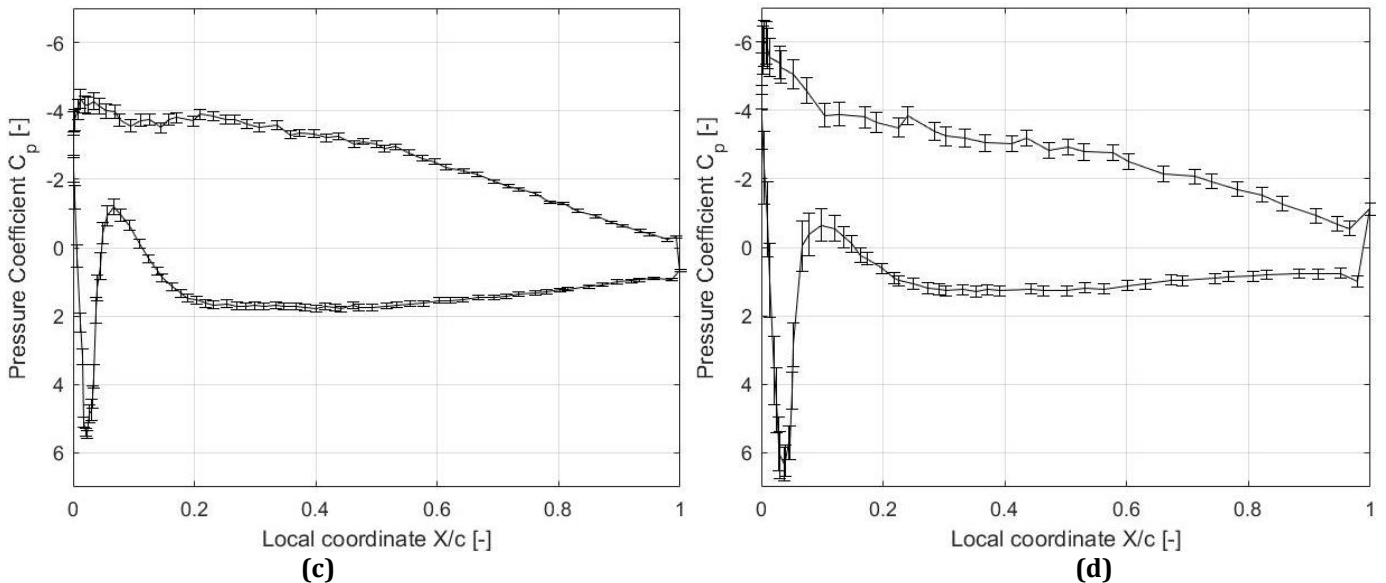


Figure 83. Pressure coefficient (C_p) plots with the error-bars indicating the pressure range associated with the unsteady loading during a revolution. The distributions corresponds to different span locations across the blade: (a) at $Y/R=0.5$, (b) at $Y/R=0.7$, (c) at $Y/R=0.8$ and (d) at $Y/R=0.975$.

5.2 Effects of relative phase angle

In the present section, the effects of the relative phase angle between the adjacent propellers are investigated by comparing the flow field between cases with different values of phase angle. Specifically, the baseline model, that has a relative phase angle of 0° ($DP(\Delta\phi=0^\circ)$) will be compared with the distributed-propeller system with 20° relative phase angle ($DP(\Delta\phi=20^\circ)$), focusing on the changes in the aerodynamic performance in both mean and instantaneous flow.

As depicted in Figure 84, the relative phase angle of Propeller#1 was selected equal to 20° (Figure 84). This value was chosen to avoid the simultaneous development of the trailing vorticity by the adjacent propellers. Although this could have been achieved with a different selection, the relative phase angle of 20° provides enough space and time for the flow structures produced by the blades to take their form and start their motion. This was also observed in [11], where a phase delay on thrust changes was attributed to the development of the trailing vorticity by adjacent propellers.

Due to the phase difference between the blades of adjacent propellers, the performance is expected to be slightly affected. In a time-averaged perspective, the performance of Propeller#1 should not be affected, as the phase angle does not alter the induced effects of the vortex systems. Thus, a behaviour similar to the baseline model is expected. The effect of the relative phase angle could play, though, a major in the unsteady loading analysis. Since the blades of the adjacent propellers will not pass from the same area simultaneously, their interference is expected to be decreased, reducing the unsteady loading. At the same time, the slipstream deformation is also expected to be reduced due to the increased distance between neighbouring vortex filaments, reducing the induced velocities that were observed in the baseline model.

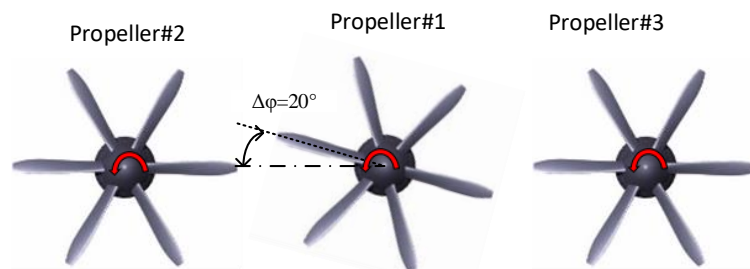


Figure 84. Front view of the distributed-propeller case with 20° relative phase angle between propellers.

The time variation of thrust coefficients for all three cases examined in the present study is presented in Figure 85. The thrust coefficient curve corresponding to Propeller#1 for the case of the relative phase angle of $\Delta\phi=20^\circ$ ($DP(\Delta\phi=20^\circ)$) shows that the time-averaged performance is the same as in the baseline

model, equal to $T_c=0.4325$. The main difference observed in Figure 85 is related to the range of thrust oscillations between the two distributed-propeller models. The standard deviation of the oscillating thrust for the baseline model is decreased from 0.00103 to $4.5e-04$ in the case of $\Delta\phi=20^\circ$, implying a reduction of the unsteady loading.

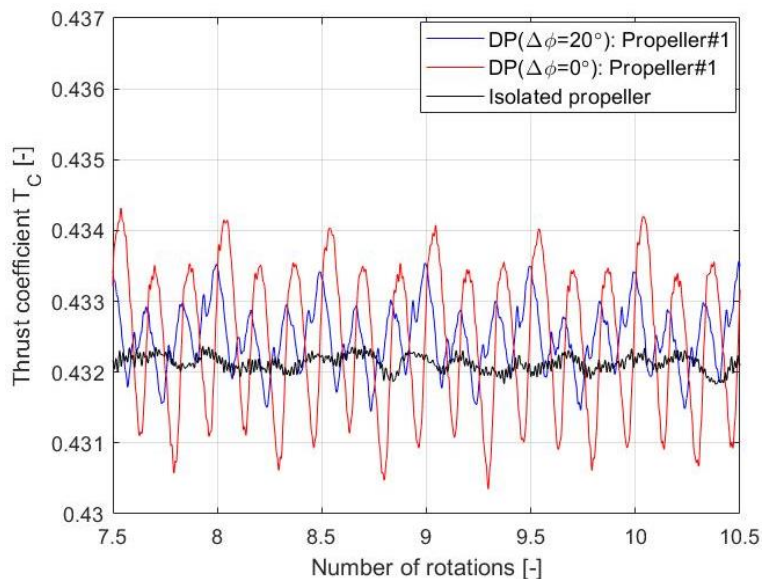


Figure 85. Time evolution of the thrust coefficient of Propeller#1 for the distributed-propeller case with 20° relative phase angle (DP($\Delta\phi=20^\circ$)). For comparison, the respective values for the isolated-propeller and distributed-propeller (DP($\Delta\phi=0^\circ$)) case with 0° relative phase angle are shown.

The change in the oscillatory behaviour is also depicted in the performance of the blades. Table 10 illustrates the time-averaged thrust coefficients comparison and the corresponding standard deviations for the two cases of the distributed-propeller models. The performance of Blades 1 and 2 are reversed, while the thrust coefficient for Blade3 is reduced. This is attributed to the blades' azimuthal location with respect to the Cartesian axis, as explained in Section 4.1. In parallel, the standard deviation of thrust coefficient in all blades decreases. This decrease is related to the reduction of the unsteady loading component.

Table 10. Time-averaged thrust coefficients and standard deviation comparison between the baseline model (DP($\Delta\phi=0^\circ$)) and the case with 20° relative phase angle (DP($\Delta\phi=20^\circ$)).

	T_c DP($\Delta\phi=0^\circ$)	T_c DP($\Delta\phi=20^\circ$)
<i>Blade1</i>	0.07654 ± 0.001395	0.07231 ± 0.001298
<i>Blade2</i>	0.06892 ± 0.001271	0.07469 ± 0.001257
<i>Blade3</i>	0.07079 ± 0.001368	0.06928 ± 0.001279
<i>Propeller</i>	0.4325 ± 0.00103	0.4325 ± 0.00045

5.2.1 Flow field comparison with the baseline model

The present section refers to the differences between the two cases with different relative phase angles as observed in the mean and phase-averaged flow field. The respective contours of the baseline model are presented in order to make the evaluation of the flow field changes easier. The differences of the mean flow field are mentioned initially by comparing the axial velocity contours and the slipstream deformation. Subsequently, the vortex field is compared through the 3D visualization of the vortex cores using λ_2 criterion, while vorticity contour slices are used to examine the evolution of tip vortices.

5.2.1.1 Mean flow field

The visual comparison of the mean axial velocity contours in Figure 86 between the baseline model and the model with the relative phase angle of 20° reveals minor differences. The conditions upstream of the propellers are identical in both cases, showing no variation in the axial and tangential velocity. In a time-averaged sense, the upstream conditions were expected to remain unaltered since the steady induced effects are independent of the relative phase angle between the propellers.

The only difference that is observed in the mean flow is downstream of the propellers, as depicted in Figure 87. The wake flows of the propellers do not approach each other as happened to the baseline model, as indicated in Figure 86 inside the red circles. In the downstream location of $X/D=0.6$, the radial distance between the adjacent flows is larger than in the baseline case, while further downstream, it increases even more. The axial velocity plot (Figure 87) reveals the increased distance between adjacent flows in this streamwise location. The velocity distributions are identical at inboard sections, while the discrepancy starts at a radial position equal to the propeller radius ($r/R=1$). The velocity curve in the case with 20° relative phase angle rises further outboard at distance $r/R=1.1$, while the rise of the velocity curve in the baseline model takes place at $r/R=1.05$, implying a reduced interference between the wakes.

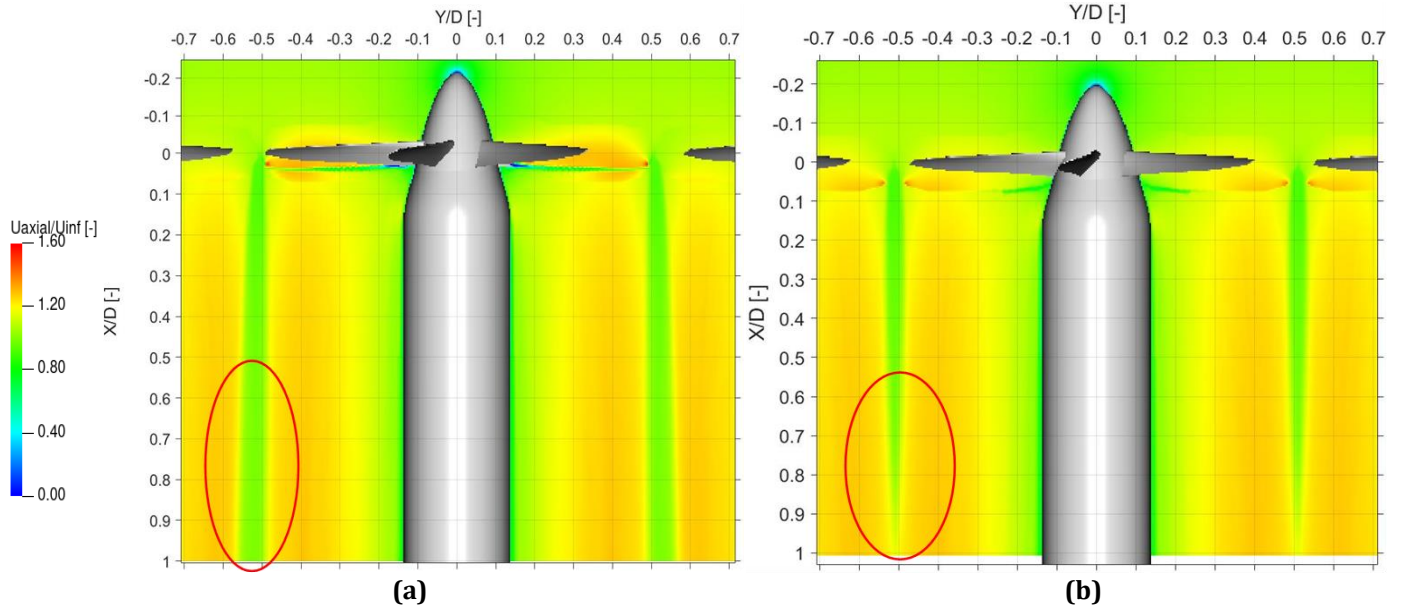


Figure 86. Axial velocity contour of the mean flow field for distributed propellers with 20° (a) and 0° (b) relative phase angle. The normalized values are relative to the free-stream velocity.

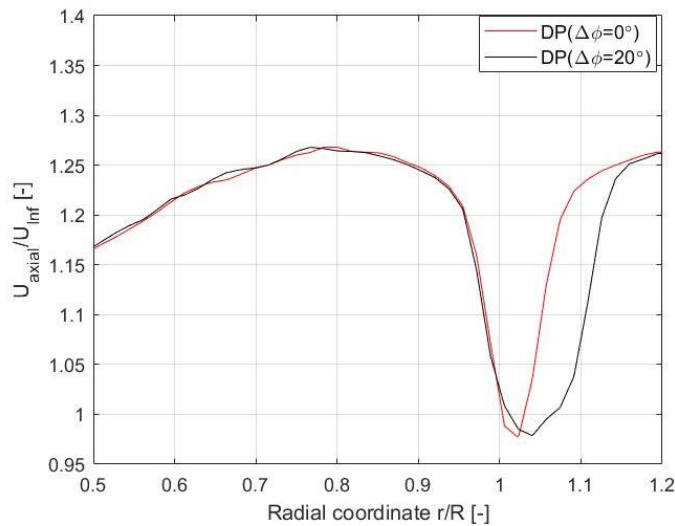


Figure 87. Comparison of the normalized axial velocity distributions between the distributed-propeller cases with 0° (DP($\Delta\phi=0^\circ$)) and 20° (DP($\Delta\phi=20^\circ$)) relative phase angle. The measurement location is downstream of the propellers at $X/D=0.6$.

The effect of relative phase angle is also evident in the slipstream deformation. As shown in Figure 88, the deformation of the slipstream at $X/D=0.1$ shows a different deformation shape. Figure 88b shows that the slipstream deformation of Propeller#1 has a more “bumpy” shape than the baseline model in Figure 88a. The pronounced deformation of the slipstream was also noticed in the experimental analysis by de Vries, et al. [11]. This is depicted in Figure 88c, corresponding to a 10° relative phase angle. The reason for this deformation lies in the orientation of the tip vortices, similar to the sketches of the induced effects between adjacent vortices in Section 5.1.2.1.

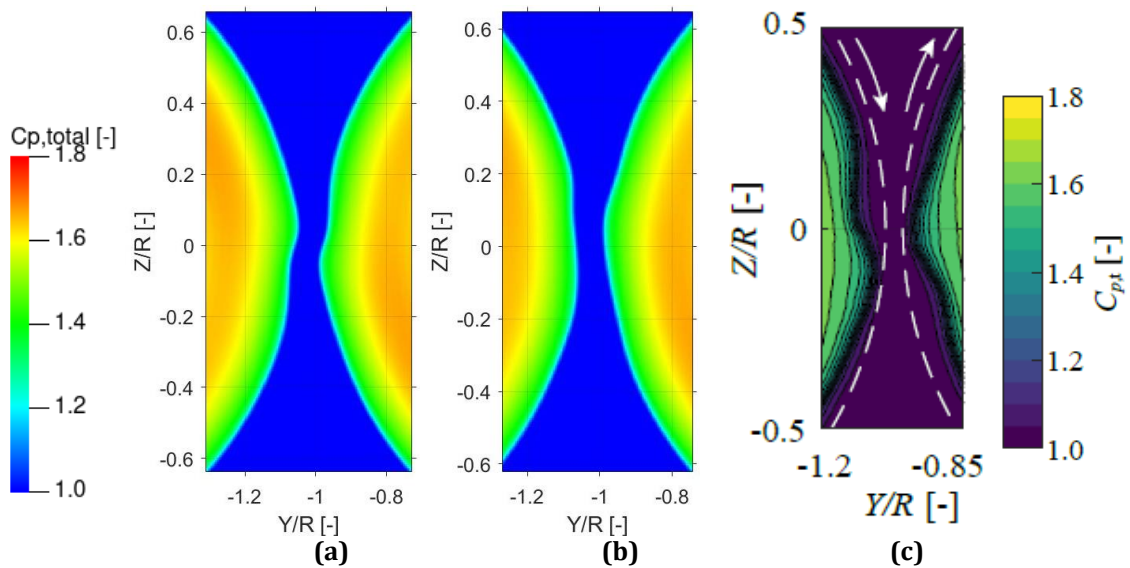
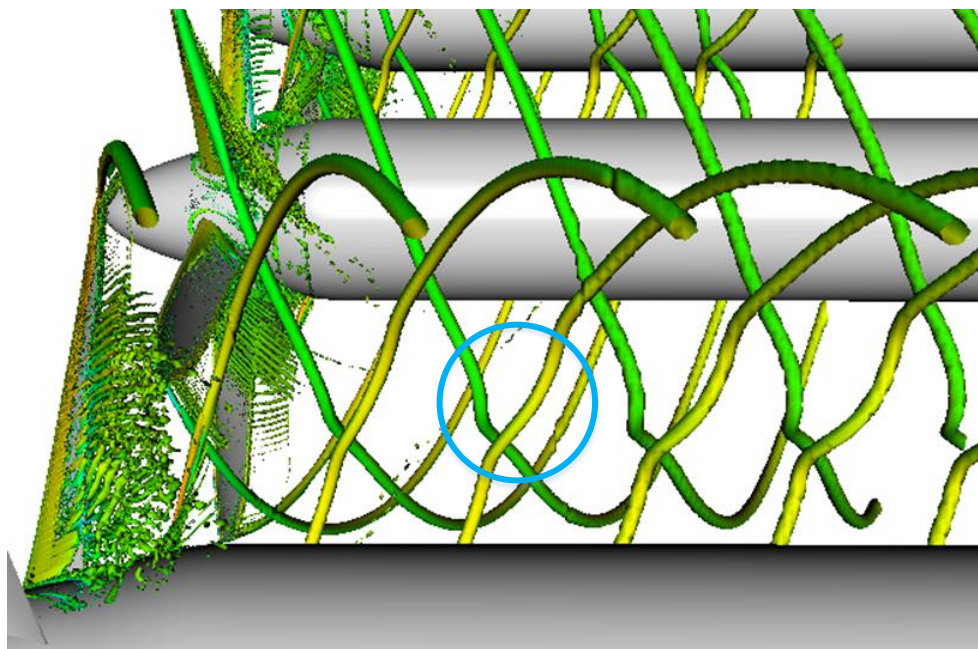


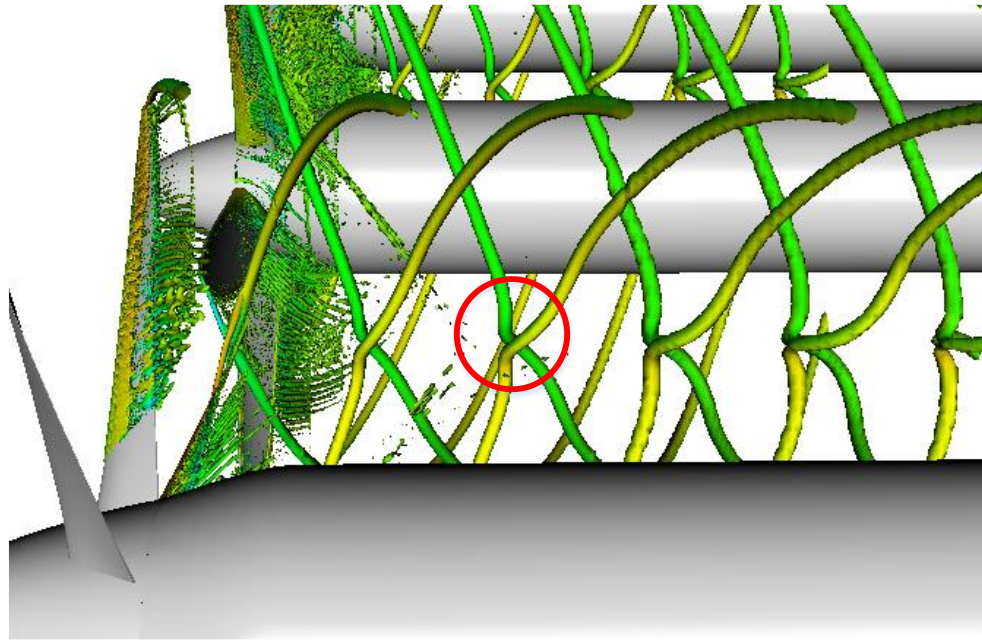
Figure 88. Comparison of the total pressure coefficient in the slipstream at $X/D=0.1$ for the distributed-propeller case with 20° (b) and 0° relative phase angle (a). Zoom in views between Propeller#1 and #2. Figure (c) shows the slipstream deformation observed experimentally with a 10° relative phase angle.

5.2.1.2 Vortex field

The 3D isosurface visualisation of the vortex cores for the case of 20° relative phase angle reveals a change in their development compared to the baseline model. Figure 89 depicts both cases, with the circled regions indicating the differences between the two cases. It is observed that the deformation of the vortex core of the 20° -relative-phase-angle case is less intense than the baseline model. Due to the phase difference, the vortex cores of adjacent propellers move at different streamwise locations, increasing the distance between them. On the contrary, the vortex cores in the baseline model are located at the same streamwise location, leading the adjacent vortices to be next to each other. Thus, the induced velocities between adjacent vortices for the baseline model are more intense than those with a 20° relative phase angle. As a result, the deformation of the vortex structure is less pronounced than in the baseline model.



(a)



(b)

Figure 89. Phase-averaged isosurface comparison based on λ_2 criterion ($\lambda_2 = -7 \times 10^6$) between the distributed-propeller model with 20° relative phase angle (a) and the baseline model (b).

Similarly, the out-of-plane vorticity contour along the XY plane in Figure 90 reveals a different pattern in the distribution of tip vortices between the two cases. The tip vortices in Figure 90a can be clearly distinguished from the neighbouring vortices due to their different streamwise location. In parallel, the shape of tip vortices remains unaffected without any noticeable change in their circular shapes, compared to the clearly deformed vortices in Figure 90b. This is evident in the shape change for vortices E1 and F1 in the far-field. Interestingly, the radial location of the tip vortex cores of the middle propeller remains at $Y/D=0.5$, as happened to the baseline case. On the contrary, the respective cores of adjacent propellers (Propeller#2 and #3) are located further outboard around $Y/D=0.6$. Thus, the phase difference between adjacent propellers results in an increased streamwise distance between neighbouring vortices that leads to reduced induced velocity components making the deformation of the vortex isosurface less pronounced than in the baseline model where the relative phase angle is 0° .

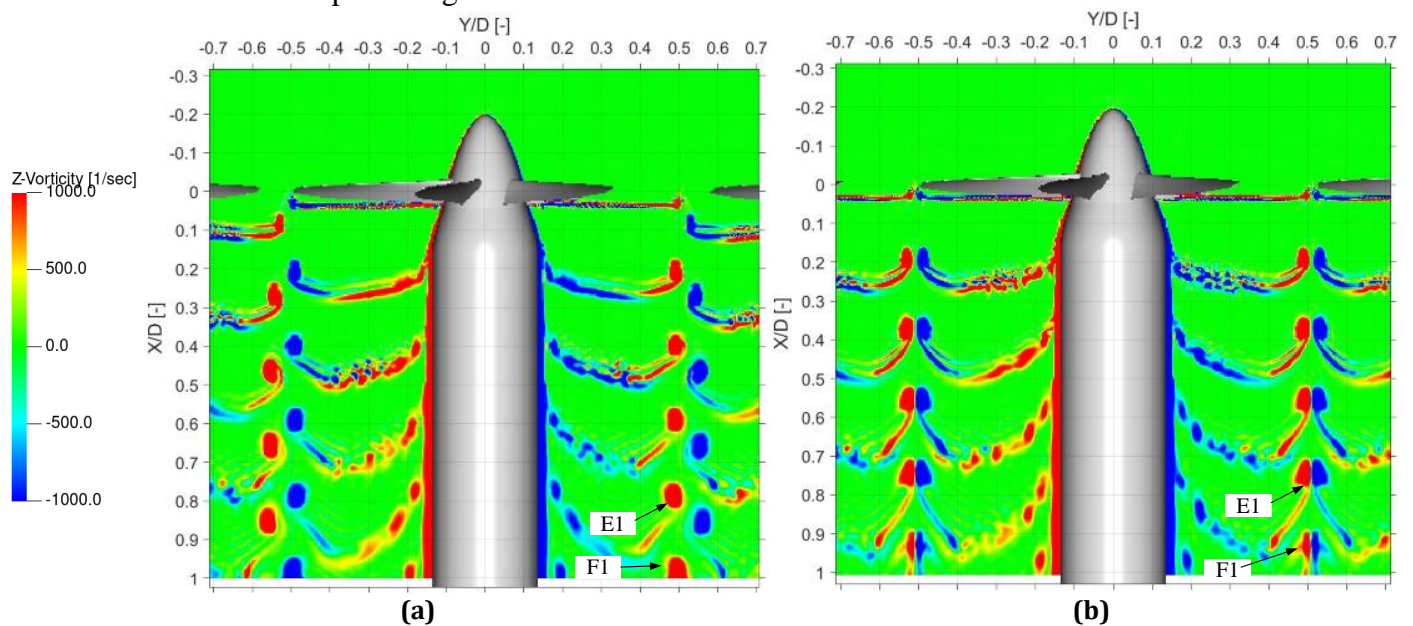


Figure 90. Out-of-plane vorticity contours for the distributed-propeller configuration with 20° (a) and 0° relative phase angle (b). The evolution of the vortices E1 and F1 shows the differences between the two cases.

5.2.2 Effect on unsteady loading

The previously presented analysis shows that the induced phenomena that a blade experiences as it passes through the area close to the adjacent propeller is reduced. This has a direct effect on the reduction of the unsteady loading on blades of Propeller#1. The reduction of the unsteady loading is evident by the reduced oscillations of the produced thrust. The time evolution of the thrust coefficient in Figure 91a shows a decline in the amplitude compared to the baseline case. The amplitude reduces from 5.35% of the mean thrust to 5.22%. In parallel, the reduction of the unsteady loading is evident in the standard deviation of the thrust coefficient distribution along the blade span in Figure 91b. There is a reduction up to 18.9% at $r/R=0.96$, denoting a reduced unsteadiness that the blades experience compared to the baseline case. Although the decrease in the unsteadiness is distributed along the blade span, it is most noticeable near the tip as can be seen by the pressure coefficient distributions below at different spanwise locations.

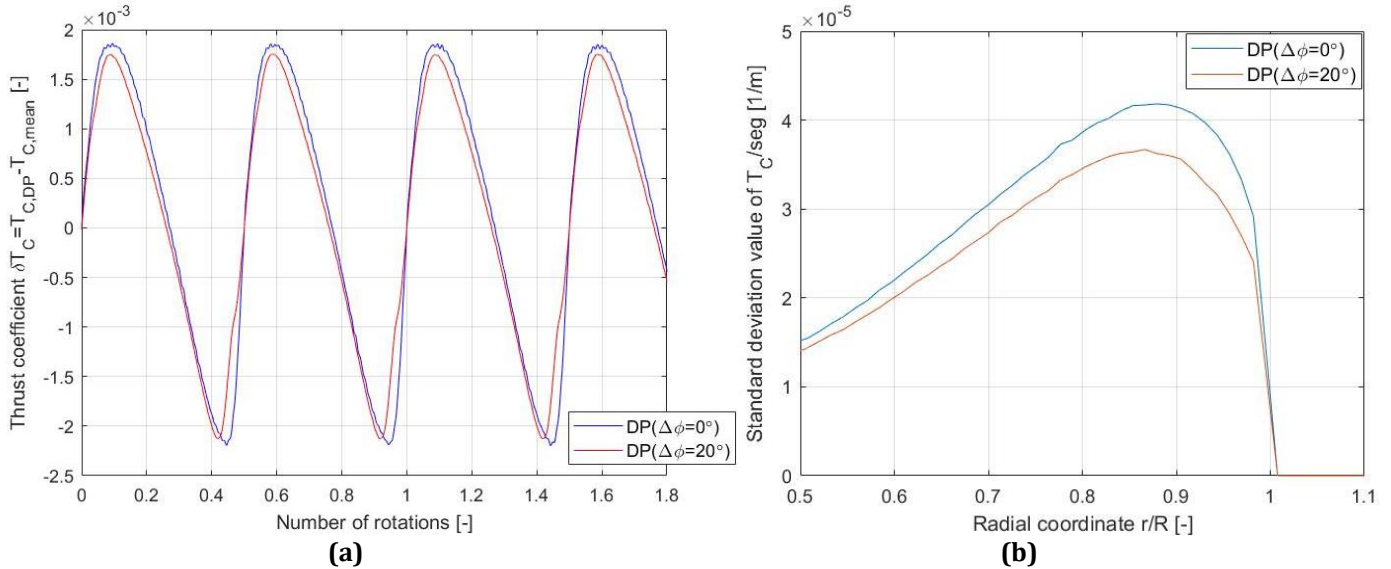


Figure 91. Comparison of the T_c evolution of Blade1 in time (a) and the standard deviation of the thrust coefficient distribution along the blade-span (b) between the distributed-propeller case with 20° ($DP(\Delta\phi=20^\circ)$) and 0° relative phase angle ($DP(\Delta\phi=0^\circ)$).

The reduced unsteady component on the blade's surface is also depicted in the pressure curves along the blade. Figure 92 illustrates the pressure coefficient curves at different spanwise locations, namely at $Y/D=0.7$ and $Y/D=0.975$. Along with the mean pressure coefficient curves, the range of the pressure fluctuations is shown, indicated by the error-bar lines. Similarly to Figure 83 for the distributed-propeller model with 0° relative phase angle, the standard deviation value implies the unsteady loading on the blade's surface. The comparison between the two cases with different relative phase angles shows a reduction in standard deviation across all blade locations. The value at radial position $r/R=0.7$ reduces from 0.0925 to 0.0892 and at $r/R=0.975$ from 0.2092 to 0.1571. The reduction of the standard deviation of the pressure values underlines the reduction of the unsteady component due to the reduced induced effects by the adjacent blades. The decreased unsteady loading will directly affect the noise generation, as will be discussed in Section 6.2.

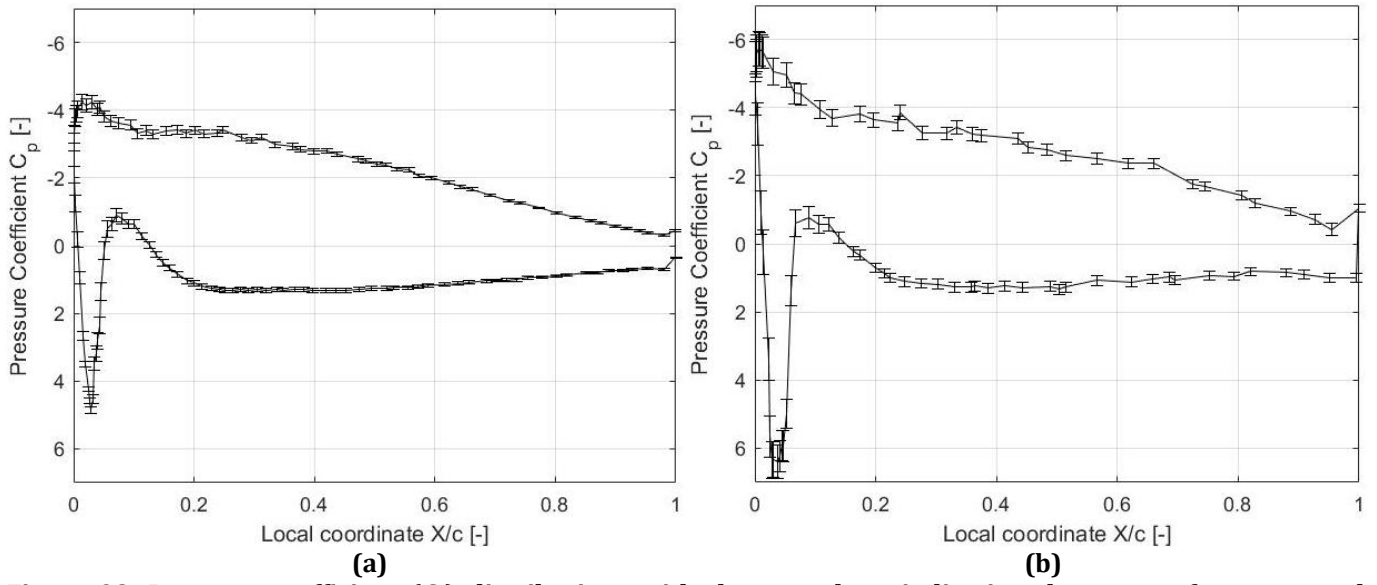


Figure 92. Pressure coefficient (C_p) distributions with the error-bars indicating the range of pressure values during a revolution for different span locations across the blade: at $Y/R=0.7$ (a) and $Y/R=0.975$ (b).

6

Aeroacoustic Analysis

This chapter presents the acoustic behaviour of the distributed-propeller configurations, considering the effect of the relative phase angle. The analysis was performed using the FWH method as described in Section 2.3.3.2 to compute the far-field noise emission of the system. Initially, the changes in noise directivity are discussed, comparing the change of the overall sound pressure level (*OSPL*) values between the isolated propeller and Propeller#1 of the distributed-propeller system. Subsequently, the behaviour in the near-field is presented in Section 6.1.1 and then the far-field spectral analysis. The final part of this analysis concludes with the effects of the relative phase angle on noise emission.

The acoustic metrics used in this analysis are *OSPL* and power spectrum (*SPL*) as defined in Eq. (1.13). The FWH analysis is based on the solid blades surfaces and the permeable surfaces, which are shown in Figure 36. The contribution of the spinner and the nacelle are relatively small and thus are omitted from the analysis.

6.1 Noise emission of the baseline model

Noise directivity plots illustrate the direction of noise emission in the far-field. Figure 93 depicts the *OSPL* emission measured in dB along the XY plane in a radial distance equal to 10 diameters from the middle propeller in the three-propeller case. The comparison of the isolated propeller with Propeller#1 in Figure 93, based on the solid surface formulation, shows an evident change of emission shape. As the azimuthal angle increases from 90° to 180° , there is a constant increase of the *OSPL* with its maximum located at 180° , i.e. in front of Propeller#1. There is an apparent noise level increase in the direction normal to the rotor plane ($\theta=180^\circ$ and 0°), as the 41.8 dB for the isolated propeller increases to 57.1 dB. In parallel, the change of the *OSPL* value at $\theta=90^\circ$ is small, only 1.2 dB, compared to the 15.1 dB increase along the propeller axis. Since the *OSPL* calculation is only based on the solid surface formulation, the increase of 12.8 dB should be associated with the unsteady loading on the blades' surface.

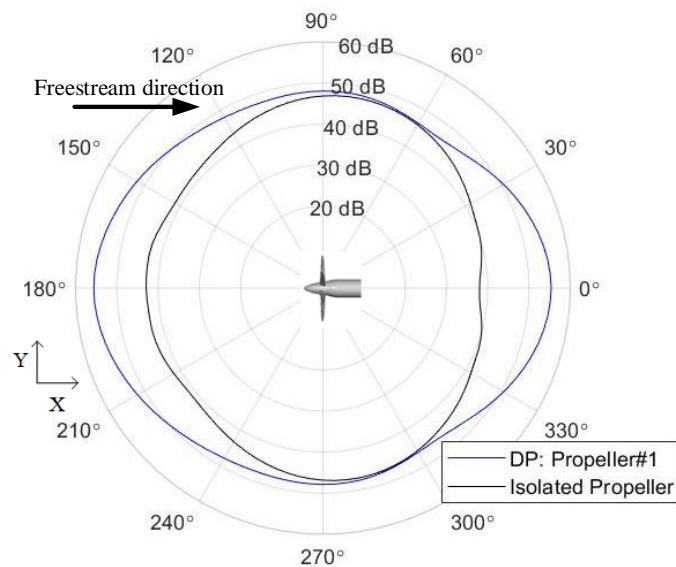


Figure 93. The OSPL emission in the far-field is compared between Propeller#1 of the baseline configuration (DP) and the isolated propeller. The OSPL values are computed based on solid surface formulation.

The increase of noise level in the direction normal to the rotor plane is attributed to the noise sources that are included in this analysis. The solid surface formulation includes only two out of three noise sources according to the FWH equation (Eq. (1.18)), namely the loading and thickness terms. Therefore, the observed changes in blade loading due to the interference between adjacent propellers results in enhanced noise emission. On the contrary, permeable surface accounts for all noise sources of the FWH equation, including the effects of the quadrupole term. The physical phenomena that are associated with this term can be examined through the Lighthill stress tensor (Eq. (1.17)). This term is determined by the unsteady perturbations relative to the uniform flow and by turbulent flow structures (e.g. shear layers and tip vortices). The pressure perturbations on the permeable surfaces would also include the radiated noise by both the solid surfaces and by the interference of the adjacent noise sources. The adjacent propellers emit sound waves, which would interfere away from the solid surfaces, implying another noise source of the distributed-propeller model. In addition, since the viscous phenomena are only considered through the quadrupole term, it is expected that this term would also include the noise production related to the interactional phenomena between the adjacent tip vortices. Therefore, the far-field analysis based on the permeable surface formulation would provide data on the effects of additional mechanisms of noise productions and on their relevance compared to the solid surface ones.

When all three propellers are considered, the noise emission pattern shows increased sound pressure levels in the direction normal to the propeller plane. Figure 94 depicts the noise emission comparison of the permeable surface formulation and the solid one for the distributed-propeller model. The resulting performance of the solid surface formulation is approximately the same as the permeable one, with the maximum discrepancy between the two curves equal to 1.5 dB at $\theta=180^\circ$. Permeable surface formulation, as discussed in section 3.1.2, considers all three terms of sound generation in the FWH equation, i.e. loading, thickness and quadrupole terms. Since the first two terms are also considered in the solid surface formulation, the effect of the quadrupole term in noise emission is minor compared to the other two components. Thus, the sound radiated by the turbulence of each wake flow and the interference between adjacent propellers does not dominate the noise emission. On the contrary, a major role in noise enhancement is attributed to the unsteady loading and the occurring thrust oscillations.

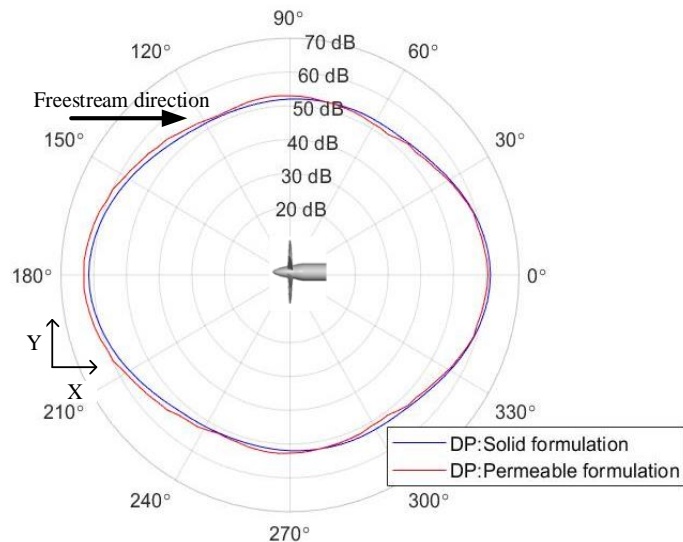


Figure 94. Comparison of the OSPL distributions of the three-propeller configuration between permeable surface formulation and solid one considering all three propellers.

In parallel, the noise emission is affected in the direction normal to the plane where all three propellers are positioned, i.e. in XZ plane. Figure 95 depicts the noise emission comparison between the isolated propeller and Propeller#1 of the baseline case for the solid surface formulation. The trend of noise level increase is the same as the XY plane, where the most remarkable increase is noticed in front and at the back of the propeller, while the increase along the plane of rotation is minor. In this plane, the increase of noise level is evident at oblique angles (30°, 150°, 210° and 330°), while in the XY plane, the noise increase is not so pronounced. This indicates that the unsteady loading affects emission angles normal to the plane of rotation and a wide range of angles oblique to the propellers axis, with a pattern similar to a dipole shape and lobe axis parallel to the propeller axis.

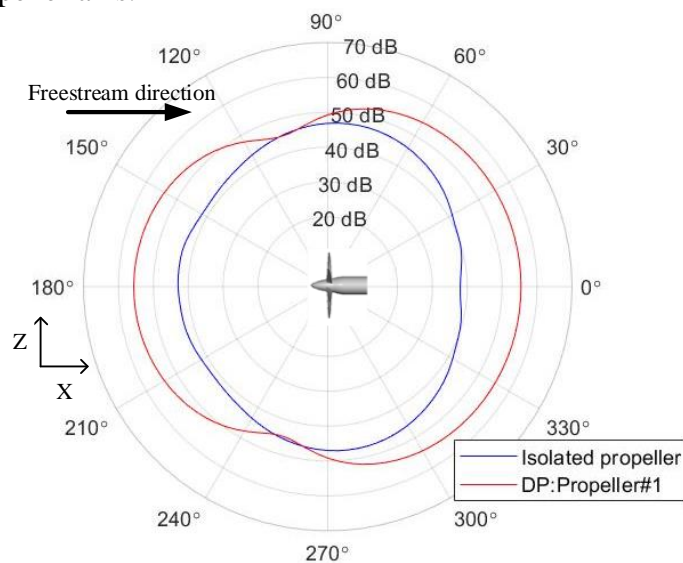


Figure 95. Noise emission values along the XZ plane. Comparison of the OSPL values between the isolated propeller and Propeller#1 of the baseline configuration (DP:Propeller#1) based on the solid surface formulation.

6.1.1 Near-field acoustics evolution

In an attempt to understand the noise interference in the distributed-propeller system, the pressure fluctuations in the near-field at the propellers plane are examined. Figure 96 illustrates snapshots of the pressure time-derivative along the propeller plane (XY plane) with the proper selection of the saturation level to visualize the pressure fluctuation field and compare the isolated propeller with the baseline model. These snapshots of pressure time-derivatives are a qualitative way to estimate the acoustic waves as well as the pressure fluctuations from hydrodynamic sources. The visualization of the acoustic waves is also related to the proper grid generation, as the number of voxels (20) per resolution area allows the acoustic waves to be visible and distinguishable, avoiding fast dissipation near the propellers.

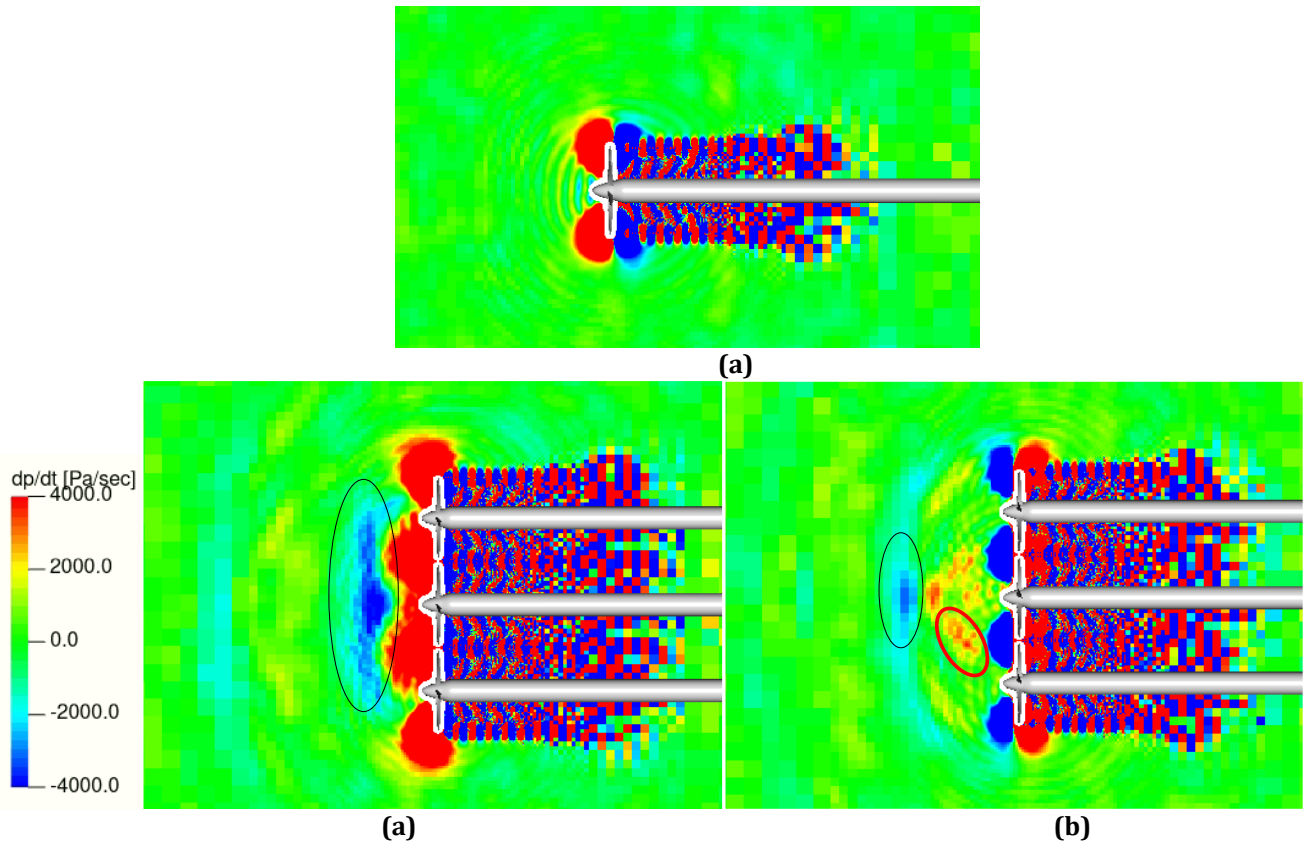


Figure 96. Snapshots of pressure time-derivatives in the near-field along the XY plane for the isolated-propeller case (a) and the baseline model with three propellers at two different time-frames(b and c).

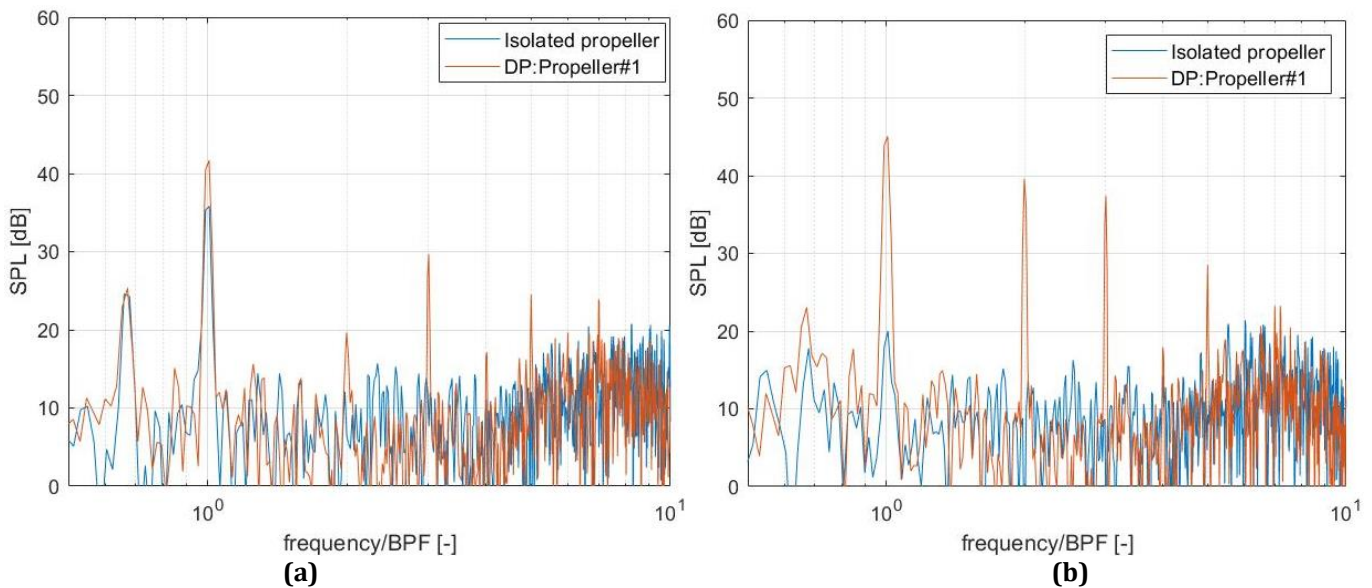
Figure 96 depicts snapshots of pressure fluctuations corresponding up to the 5th blade passing frequency (BPF) for the baseline model and the isolated propeller. Looking at the isolated propeller (Figure 96a), the major pressure fluctuations appear in front of the rotor plane with the two side lobes and in the slipstream, as indicated by the positive and negative pressure fluctuations implied by the colour change. The strongest waves are observed to be radiated by the propeller surface due to the loading noise component (see the two red side lobes in front of the propeller), while the radiation of thickness noise in the rotor plane is overshadowed by the strength of the loading noise. In the downstream direction, the pressure fluctuations, attributed to the slipstream evolution, are less intense than the lobes near the propeller.

Carefully observing the pressure fluctuations in Figure 96b and c for the distributed-propeller case, there is a clear pattern alteration compared to the isolated-propeller case. Despite the wake interference between adjacent flows, the pressure derivative pattern in the downstream direction is quite similar to the isolated propeller. However, the pressure field in front of the propellers is remarkably different. At the propeller's tip, the two side lobes of Propeller#1 appear to overlap with the respective lobes from the adjacent blades. This is attributed to the small separation distance between the propellers and implies acoustic interference. Simultaneously, intense pressure fluctuations are observed to be radiated in front of Propeller#1 and between the adjacent ones, as highlighted in Figure 96 b and c. The strong pressure fluctuation at the front of Propeller#1 is indicated with a black coloured circle at two different frames to illustrate the evolution of the pressure in the upstream direction, while the red circle between Propeller#1 and #3 (Figure 96c) indicates an interference between adjacent blades that starts propagating upstream. These waves are emitted in the upstream direction, where high-pressure-fluctuation regions are noticed far upstream of the propellers, as depicted in Figure 96c. The strong fluctuations are attributed to the unsteady interactions between the propellers, as these waves start radiating every time that two adjacent blades are approaching each other. Thus the unsteady loading on blades results in a sound wave emission upstream. This directivity of the emitted pressure fluctuations is associated with the noise emission pattern in the far-field. The upstream motion of the pressure fluctuations justifies the noise emission pattern presented above, where the increase in the *OSPL* values of the far-field was noticed in front of Propeller#1.

6.1.2 Spectral analysis

Analyzing the sound spectrum emitted in the three-propeller case will provide an overview of the effects on the tonal and broadband components in far-field noise. Based on the acoustic pressure at various points around the propeller (see Figure 35), the *SPL* values of the acoustic signal is computed to investigate the changes in the frequency domain. Both surface formulations are used to analyse the behaviour of the multiple-propeller model at different azimuthal locations,

Figure 97 illustrate the power spectrum analysis based on the solid surface formulation, comparing the isolated propeller with Propeller#1 of the baseline model. The comparison of the *SPL* distributions is examined at different azimuthal locations, namely at 180° , 130° and 90° based on Figure 93. Observing the change of tonal peaks at BPF and its integer multiples, it is evident that there is a constant increase of the *SPL* values as the emission angle approaches 180° . Starting from the 90° emission angle (Figure 97a), it is clear that the impact of the propellers interaction is relatively small. The *SPL* value at 1st BPF shows an increase of 5.9 dB compared to the isolated propeller, while higher tones are less pronounced. Tonal peaks up to 5th BPF are augmented for Propeller#1, while these tones are not identified for the isolated propeller. The enhancement of tonal components is also evident in 130° (Figure 97b), where there is a great increase of the 2nd and 3rd BPF. The respective *SPL* increase compared to the isolated propeller are: 25 dB increase at the 1st BPF, 29.5 dB at the 2nd BPF and 27.3 dB at the 3rd harmonic. The most significant increase of the tonal components is noticed at 180° (Figure 97c). The integer multiples of BPF up to the 5th BPF show a remarkable increase. The 1st BPF is the dominant tonal peak with *SPL* equal to 53.6 dB, while the 2nd harmonic reaches 45.4 dB and the 3rd one 40.9 dB. This behaviour denotes that the noise level increase observed in Figure 93 is associated with the increase of the tonal component. Since loading noise determines the tonal noise components, the augmentation of tonal components is attributed to the unsteady loading of the blades.



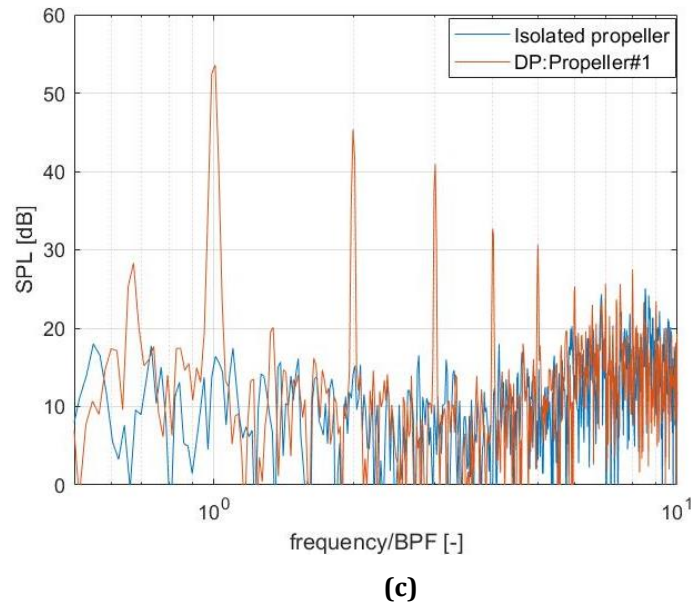
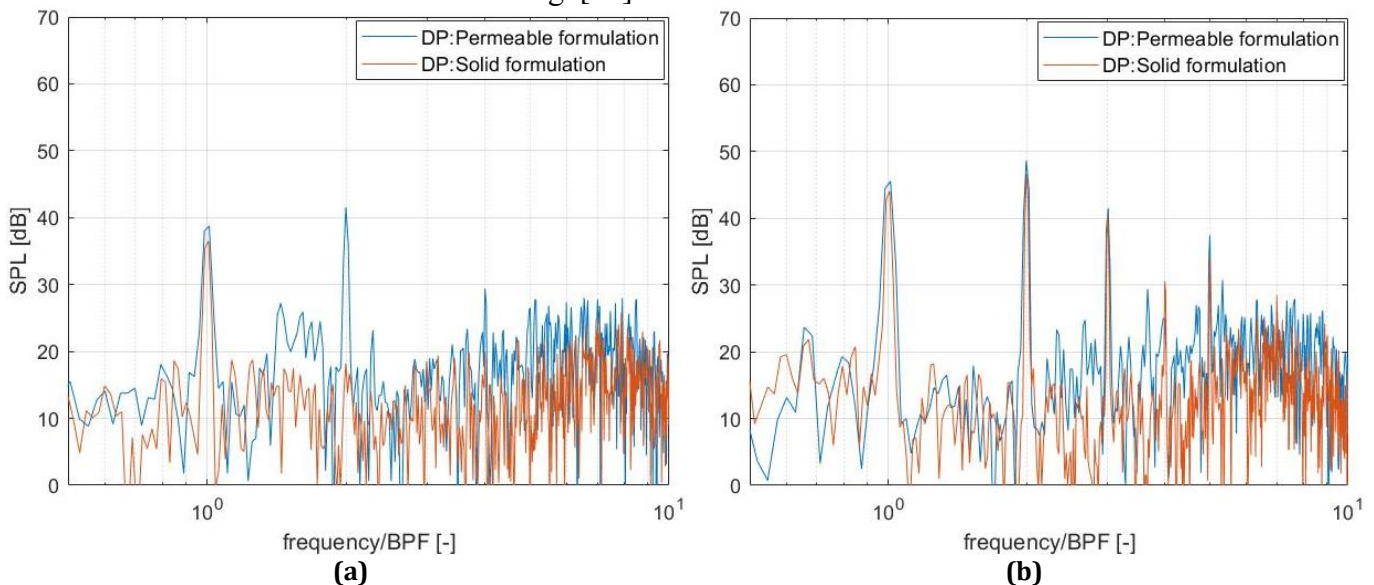


Figure 97. Spectral comparison between Propeller#1 of the distributed-propeller case (DP) and the isolated propeller. The comparison is based only on the solid surface formulation and corresponds to azimuthal positions along the XY plane: at propeller plane- $\theta=90^\circ$ (a), at $\theta=130^\circ$ (b) and normal to rotor plane- $\theta=180^\circ$ (c).

The comparison of the solid and permeable surface formulations (Figure 98) would provide the effect of the quadrupole term. Figure 98 depicts the power spectrum analysis of both permeable and solid surface formulations, including all three propellers of the system. When all three propellers are considered in the spectrum analysis, the augmentation of tonal noise components is evident at the front of the DP system (at azimuthal angles equal to 130° and 180° -Figure 98b and c), similarly to the solid formulation of Propeller#1. The *SPL* values of the tonal components for the permeable surface are slightly higher (~ 2 dB) than the respective peaks of the solid formulation at the different azimuthal angles. Another difference between the two formulations is observed at the high-frequency regime. At frequencies higher than the 5th BPF, the broadband component of the permeable surface is enhanced compared to the same values for the solid surface. This is most evident at azimuthal angles equal to 130° and 180° , with an increase of 3.5 dB and 2.1 dB, respectively. This increase should be attributed to the quadrupole effect (considered only in permeable surface formulation) associated with the wake flow interference between the adjacent propellers.

The above-presented results follow the literature findings. Zhou, et al. [9] associated the enhanced tonal noise at the direction behind the rotors to the dynamic loading of the rotor blades, while the broadband increase was associated with the flow structures behind the propellers. Similarly, Afari and Mankbadi [47] computed an increase in the fundamental tone at the first BPF, while the increased broadband component was attributed to the “increased wake mixing”[47].



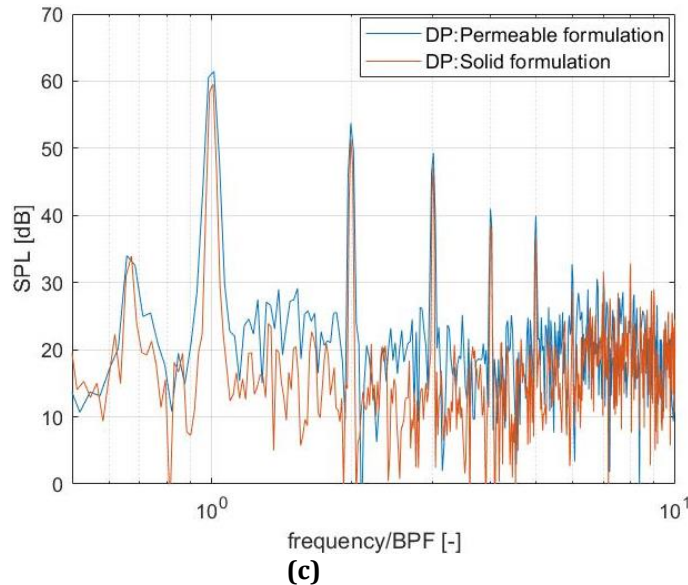


Figure 98. Spectral comparison between the distributed-propeller case (DP) and the isolated propeller along the XY plane. The comparison is based on the permeable surface formulation and corresponds to azimuthal positions: along propeller plane- $\theta=90^\circ$ (a), at $\theta=130^\circ$ (b) and normal to rotor plane- $\theta=180^\circ$ (c).

6.2 Relative phase angle effect

This section presents the effects of the relative phase angle on the acoustic signature by examining potential differences in the noise emission pattern in the far-field, the near-field pressure, and the power spectrum analysis between the distributed-propeller cases with 0° and 20° relative phase angle.

6.2.1 Noise directivity comparison

The noise emission for the distributed-propeller model with 20° relative phase angle (DP($\Delta\phi=20^\circ$)) is shown in Figure 99 at the same plot with the baseline model (DP($\Delta\phi=0^\circ$)). Figure 99a depicts the noise emission based on the permeable surface formulation where all three propellers of the configuration are included. Compared to the 0° -relative-phase-angle case, there is a noticeable noise level reduction in azimuthal angles at the front of the propellers plane. In front of Propeller#1 at 180° , the noise level is decreased from 63.0 dB to 58.0 dB. There is also an area where the noise level increases up to 1.8 dB between the emission angles 60° - 90° and 270° - 300° . In parallel, Figure 99b depicts the noise emission due to Propeller#1 based on the solid surface formulation. The reduction of *OSPL* at 180° is from 55.6 dB at 180° to 49.9 dB. It is worth mentioning that although the permeable surface formulation includes all noise sources, the *OSPL* reduction is of the same level as the corresponding reduction in the solid surface formulation. This leads to the conclusion that the reduction of unsteady loading, as a result of the implementation of the relative phase angle, is the primary source of noise emission reduction.

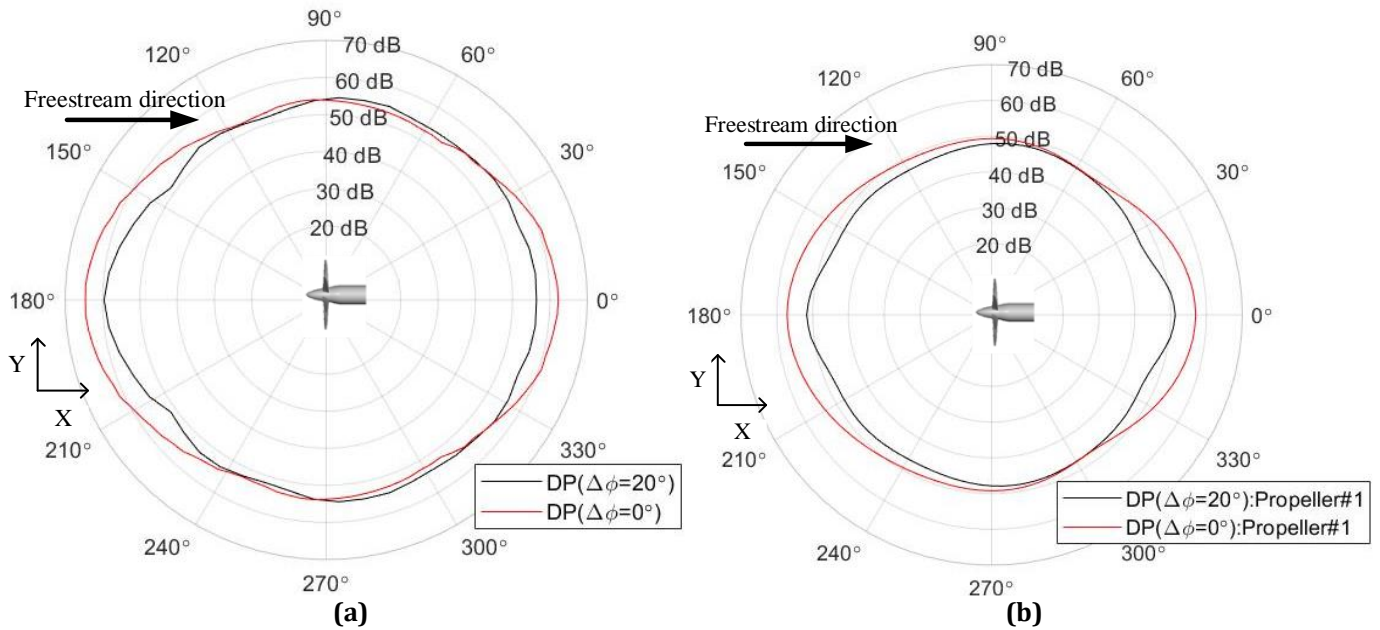


Figure 99. Comparison of the OSPL noise emission along the XY plane between the baseline configuration (DP($\Delta\phi=0^\circ$)) and the case with 20° relative phase angle (DP($\Delta\phi=20^\circ$)). The OSPL values are computed based on permeable (a) surface formulation and the solid one for Propeller#1(b).

The positive impact of the relative phase angle is also evident along the XZ plane (normal to the plane where all three propellers are located). Figure 100 depicts the noise emission comparison between the two cases with different relative phase angles (permeable and solid surface formulations). The noise level reduction is evident along the propeller axis, where the reduction reaches 5.6 dB at 180° emission angle (Figure 100b). The shape of the noise reduction resembles that of a dipole, implying that the noise reduction is associated with the reduced unsteady loading. The noise emission based on the permeable surface formulation (Figure 100a) also illustrates a noise level reduction at all emission angles up to 4.9 dB along 180° and 5.6 dB along 60° . This implies that apart from the reduced unsteady loading contribution, the contribution of the quadrupole terms is also reduced due to the reduced interference of the adjacent tip vortices.

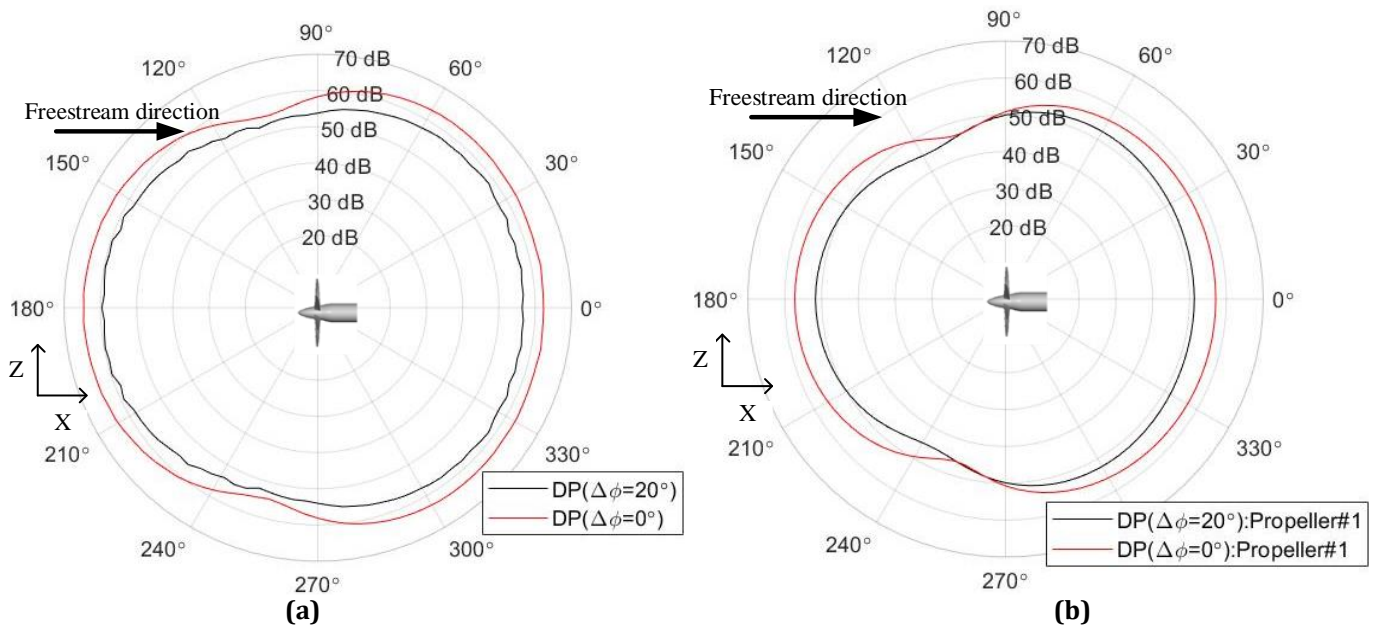


Figure 100. Comparison of the OSPL noise emission along the XZ plane between the baseline configuration (DP($\Delta\phi=0^\circ$)) and the case with 20° relative phase angle (DP($\Delta\phi=20^\circ$)). The OSPL values are computed based on permeable (a) surface formulation and the solid one for Propeller#1(b).

6.2.2 Near-field acoustics alteration

The near-field behaviour of the distributed-propeller model with a 20° relative phase angle is assessed by investigating the pressure fluctuations along the XY plane. Figure 101 illustrates different snapshots of the pressure time-derivative in saturated level to make the pressure fluctuations visible. The visual inspection of the field shows that there are fewer regions with extreme peaks and lows at the front of the propellers than in the baseline model (Figure 96). More specifically, the strong fluctuations in front of Propeller#1 are less noticeable or absent, while the interference of the propellers is rather different. The black circles indicate the high and low peak values in front of Propeller#1, which are less enhanced than the baseline model. Similarly, the red circles show weak pressure waves in the region between the propellers, implying an interference decrease compared to the case with a 0° relative phase angle. The phase angle variation between the propellers leads to the interference of pressure fluctuations with a phase delay, resulting in the cancellation of extreme pressure values in the near-field. In Figure 101b, the lobes of Propeller#1 has opposite sign from the adjacent ones of Propeller#2 and 3, resulting in the cancellation of each other. On the contrary, the same blades with 0° relative phase angle enhanced the adjacent pressure lobes because they were in the same phase, as depicted in Figure 96. Therefore, this qualitative comparison of the near-field pressure fluctuations between the two cases with 0° and 20° relative phase angles shows the beneficial impact of the relative phase angle in front of the propellers along the XY plane due to the destructive interference between the propellers compared to the constructive one observed in the baseline case.

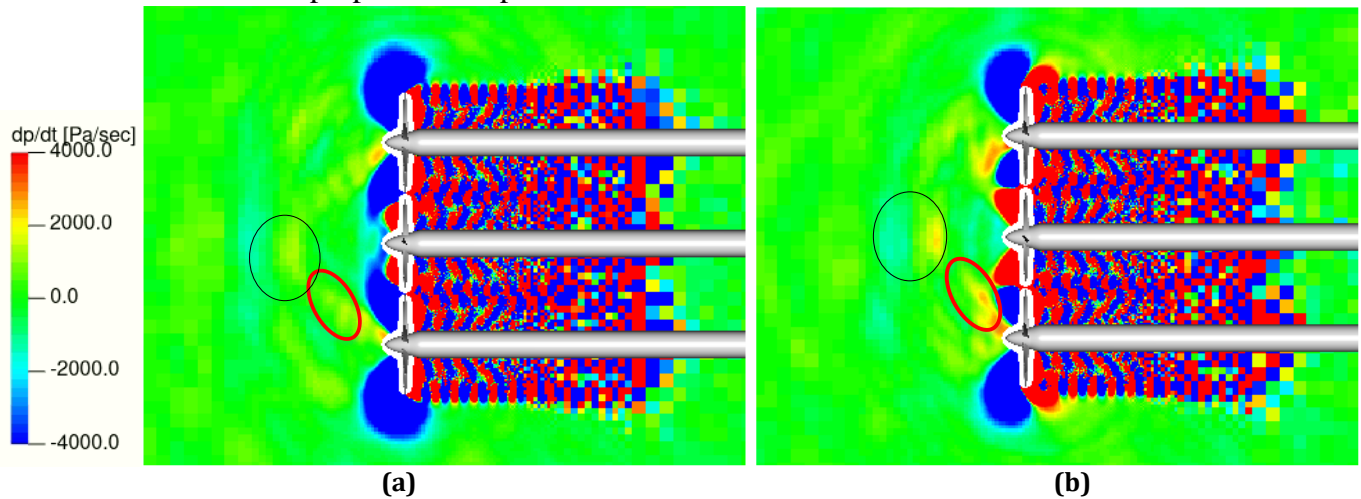


Figure 101. Snapshots of the pressure time-derivatives in the near-field along the XY plane at two frames of the distributed-propeller model with 20° relative phase angle. The region of high- and low-pressure fluctuations is indicated with black in front of Propeller#1 and between the propellers with red circles.

6.2.3 Spectral analysis comparison

The frequency-domain analysis of the acoustic signals in the far-field along the XY plane depicts the change in the noise emission. Figure 102 illustrates the power spectrum plots for Propeller#1 based on solid surfaces at two azimuthal locations: at 90° (along the propeller plane) and 180° (in front of the propeller). Comparing the two cases shows a positive impact of the relative phase angle on tonal components. At an emission angle of 180° , the enhanced tonal peaks in the baseline case show a reduction. The 1st peak at BPF shows a 7.8 dB reduction, with slight reductions in other tonal components (3.6 dB for the 2nd tonal peak). The great decrease of the dominant tonal peak is the main reason for the overall *SPL* reduction in the far-field at this location, as the rest of the tonal peaks show a slight decrease if any.

Regarding the spectrum analysis along the propeller's plane, the effect of the relative phase angle is negligible. The tonal peaks at various frequencies show little or no effect on the values of the tonal peaks. The 1st tonal harmonic shows no deviation from the 0° -relative-phase-angle case, which largely determines the behaviour at this region. A slight reduction is observed in the 2nd and 3rd tonal components up to 4 dB, whereas no large discrepancy of the two curves is noticed in high frequencies. Thus, the reduced tonal components associated with the unsteady loading reduction at these emission angles shows the positive impact of the relative phase angle.

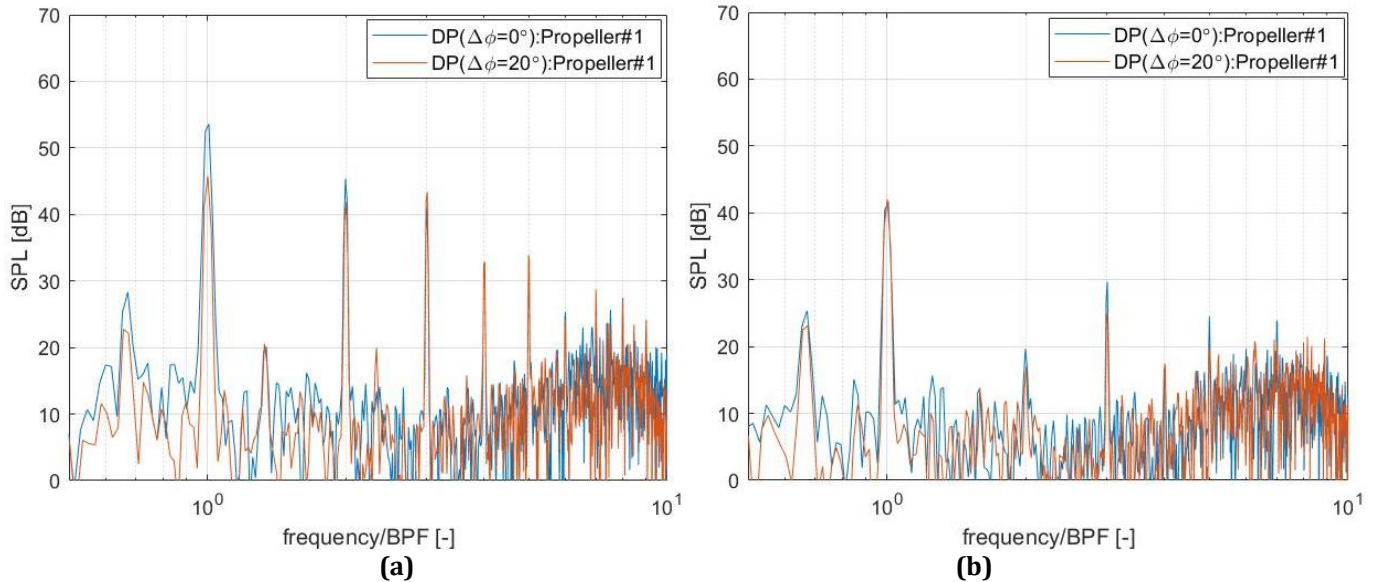


Figure 102. Spectrum comparison between Propeller#1 for the case with 20° (DP($\Delta\phi=20^\circ$)) and 0° (DP($\Delta\phi=0^\circ$)) relative phase angle. The comparison is based on the solid surface formulation and corresponds to azimuthal positions: normal to rotor plane- $\theta=180^\circ$ (a) and along propeller plane- $\theta=90^\circ$ (b) along the XY plane.

At emission angle $\theta=75^\circ$ (Figure 99a), the *OSPL* value of the case with 20° relative phase angle is 1.8 dB enhanced compared to the respective value of the baseline model, based on the permeable surface formulation. Observing the power spectrum comparison based on the permeable surface formulation in this emission angle shows that the noise level increase is primarily associated with tonal enhancement. The increase at the 1st BPF is equal to 9.9 dB, while a similar increase is observed for the 3rd BPF. This observation might be related to the effect of the relative phase angle that redistributes the tonal components at these emission angles degrading the noise level. In addition, this behaviour might be related to the different azimuthal location of blades in Propeller#1 wrt the Cartesian axis that affects the loading and consequently the acoustic signal.

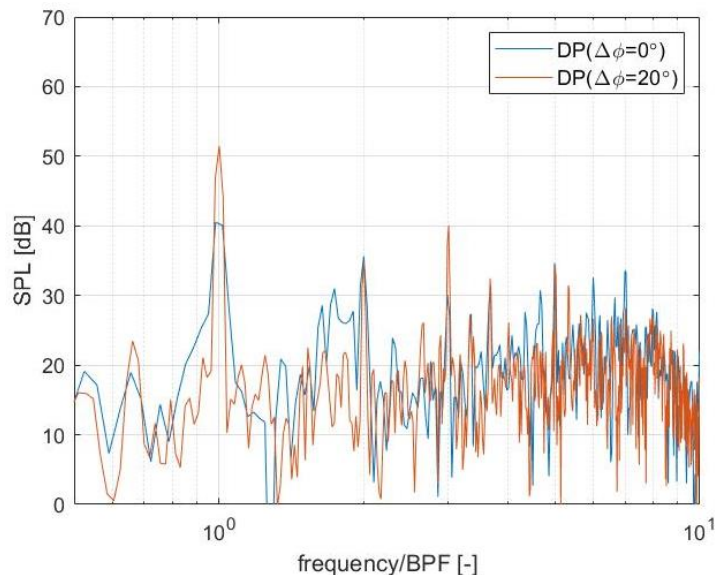


Figure 103. Spectrum comparison between the distributed-propeller models with 20° (DP($\Delta\phi=20^\circ$)) and 0° (DP($\Delta\phi=0^\circ$)) relative phase angle. The comparison is based on the permeable surface formulation and corresponds at $\theta=75^\circ$ along the XY plane.

The bar chart below summarizes the findings of the *OSPL* values at different azimuthal locations for all cases examined in the present analysis. The results are compared in seven different points whose distance from the middle propeller of the distributed-propeller systems is equal to 10 times the diameter, as shown in Figure 104. Points A, B, C, D are located along the XZ plane, with point A along the X-axis in front of the middle propeller, point C positioned below the distributed-propeller system and points B and D with oblique angles depicted in the figure. Points A, E, F and G are located along the XY plane, with point F along the Y-

axis. The *OSPL* comparison shows a significant increase in the noise emission for the distributed-propeller model compared to an isolated propeller at all angles, with the maximum *OSPL* values located in front of the middle propeller. Also, the comparison indicates the beneficial impact of the relative phase angle in the distributed-propeller model, as the *OSPL* values at the front of the system are reduced by up to 5.6 dB (points A, B and D). However, along the XY plane, where all three propellers are located, the effect of the relative phase angle results in a noise increase up to 1.8 dB in points F and G. Thus, the effect of the relative phase angle can be beneficial at specific emission angles, but it can also lead to a noise increase in some others.

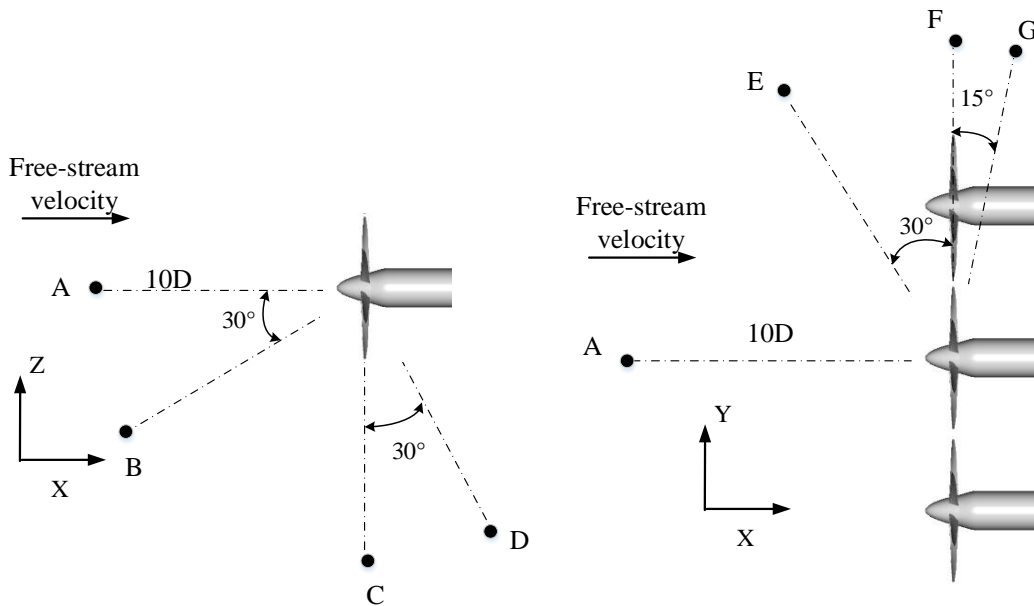


Figure 104. Points' location around the distributed-propeller system along the XY and XZ planes.

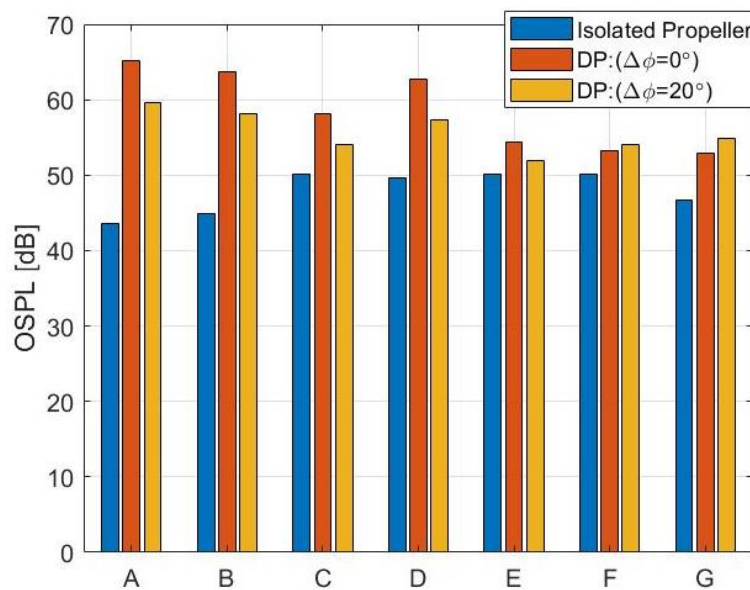


Figure 105. Comparison of the *OSPL* values between the isolated propeller and the distributed-propeller model with 0° and 20° relative phase angles at different azimuthal positions.

7

Conclusions and Recommendations

The development of the all-electric and hybrid-electric aircraft concepts has regenerated the interest in distributed propulsion systems in an attempt to meet future goals for low noise and pollutant emissions and to expand the aviation market in urban air mobility through the concepts of electrical vertical take-off and landing. Distributed-propeller systems have been incorporated in such aircraft and UAVs designs as propulsive configurations where multiple propellers are positioned along the wing or the airframe. Therefore, the motivation for this study is related to the need to delve into this system and understand the physical mechanisms associated with the interactional phenomena of these propulsive configurations that affect their performance. The present analysis's objective is to investigate the aerodynamic and aeroacoustic behaviour in a distributed-propeller system in forward flight. The investigation of the aerodynamic and aeroacoustic interferences was performed through a high-fidelity computational study, with the main conclusions being summarized below.

- What are the physical mechanisms associated with the differences in the aerodynamic and aeroacoustic performance of a distributed-propeller configuration compared with an isolated propeller?

The comparison of the distributed-propeller model with the isolated-propeller case showed minor differences in the time-averaged performance. The time-averaged thrust coefficient increases slightly by 0.0005, whereas the time evolution plot reveals thrust oscillations with a standard deviation value equal to 0.001. The increased time-averaged performance is not expected, as both experimental and numerical studies have shown the opposite. This model discrepancy might be related to the non-uniform behaviour of the propeller's blades due to the effect of the azimuthal location of the blade with respect to the Cartesian axis. The oscillatory behaviour of the thrust, indicating the unsteady loading, is attributed to the induced velocity components from the propellers vortex system. The noise emission of the distributed-propeller system shows an increase of 15.1 dB along the propellers axis compared to the isolated propeller, while the increase is only 1.2 dB along the propellers plane. The directivity pattern of noise emission resembles that of a dipole along the propeller axis, and considering the enhanced tonal components, the change in aeroacoustic behaviour is attributed to the unsteady loading.

- How are the inflow conditions affected by multiple adjacent propellers?

The induced effects by the trailing vortex system of the propellers alter the flow conditions upstream of the propellers. The vorticity of a single propeller induces axial and radial velocities components in the upstream flow. Thus, the combined effect of all propellers in close distance leads to an increased axial velocity component and a variation of the radial one. The axial velocity component upstream and between the propellers is enhanced compared to an isolated propeller. This increase originates

from the induced axial velocity components of the trailing vorticity from adjacent propellers. On the propellers plane, the increase of axial velocity is not evident as the effect of the induced axial velocity components by adjacent rotors is minor. In parallel, the induced radial velocity components upstream of the propeller creates new velocity vectors that are not radially directed. Thus, tangential components of the inflow velocity are non-zero, with changing direction. The variation of tangential velocity direction is attributed to induced radial velocity vectors, which can be parallel and oblique depending on the azimuthal location. As a result, the total velocity changes values due to the variation of the tangential velocity, which eventually leads to thrust oscillations.

- How are the slipstream velocity and pressure distribution affected by the adjacent propellers?
The mean flow field of the distributed-propeller model is deformed without radial contraction in the regions nearby to adjacent wake flows. Instead of radial contraction, the slipstream of the middle propeller in the distributed-propeller model approaches the adjacent wake flow of the neighbouring propellers in downstream locations. The axial velocity of the slipstream is reduced compared to the isolated propeller, attributed to the extension of the slipstream. The slipstream deformation is evident in the interference area between the adjacent propellers. Observing a vertical cross-sectional slice of the flow downstream of the propellers, the wake flows are curved towards each other, instead of being circularly shaped as in the isolated propeller. The curvature shape is the result of the induced effects between the neighbouring flow structures.
- What is the change in wake flow evolution of multiple adjacent propellers compared with an isolated propeller?
As the propellers blades emit the vortical structures, their shape is affected by the respective flow structures of the adjacent blade. The most evident change is noticed in the evolution of the tip vortices of blades passing simultaneously from the region between the propellers. The generated tip vortices of these blades travel downstream at nearby distances, resulting in dominant induced effects, especially at downstream streamwise areas. The induced velocities between the tip vortices lead to an alteration of the shape of their cores. Instead of a circular core, the shape is extended in the streamwise axis, enlarging the vortex's core while fast dissipation is observed. As two adjacent vortex cores are travelling downstream, their shape shows a “shear deformation” pattern, which determines the deformation of the slipstream in the time-averaged flow. On the contrary, the inboard vortical structures do not show any noticeable deviation in their motion compared to the isolated-propeller case.
- What are the reasons for the noise emission change due to multiple adjacent propellers?
The reason for the change in noise emission is associated with the enhancement of tonal components. The dipolar noise emission pattern in the far-field shows an increase at emission angles in the front of the distributed-propeller system. The tonal components present increased values in these angles compared to the isolated propeller, as proved by the tonal harmonic increase of 53.6 dB for the 1st BPF along the propeller's axis. The comparison of the noise emission based on the permeable and solid surface formulations showed minor discrepancies, implying that the dominant noise source is the unsteady loading. Thus, the augmentation of tonal components is attributed to the unsteady loading on the blades. In addition, due to the synchronizing of the propellers, the near-field acoustics reveal a constructive interference, as intense pressure fluctuations are observed upstream of the middle propeller of the distributed-propeller model, absent in the isolated propeller. These fluctuations are attributed to the interference between the propellers, as these pressure fluctuations are emitted every time two blades approach each other. This results in sound waves from the adjacent propellers that propagate upstream and interfere so that an intense

pressure fluctuation appears. Although the broadband noise component is less dominant compared to the tonal one, a slight increase of 3.5 dB at 130° was noticed. This increase should be associated with the viscous phenomena that take place in the slipstream, including the interference between adjacent tip vortices.

- To what extent does the propeller's relative phase angle influence the aerodynamic and aeroacoustic performance of a distributed-propeller model?

The effect of relative phase angle is most noticeable to the unsteady loading rather than the steady one. The time-averaged performance remains unaffected, as the thrust coefficient is the same as the baseline case. On the contrary, the oscillatory behaviour of the thrust is reduced as the standard deviation of the thrust coefficient drops from 0.001 to 4.5e-04. This reduction results in noise emission decrease, as proved by the 5 dB reduction of the distributed-propeller system in the upstream direction. In addition, an increase of 1.8 dB is noticed at oblique emission angles (60°-90°).

- What are the reasons for the change in aerodynamic and aeroacoustic performance of a model with relative phase angle compared with a model without phase angle variation?

The time-averaged aerodynamic performance remains unaltered, as can be observed by the unaffected thrust coefficient and inflow velocity conditions. This is attributed to the steady induced effects by the vortex systems, which are not affected by the phase angle. The phase difference between blades that are passing through the region between the propellers results in reduced interference compared to the case with 0° relative phase angle. The reduction of thrust oscillations, as denoted by the drop in their amplitudes, is a consequence of the decreased interference, which also affects the unsteady loading on the blades, as proved by the decrease in pressure fluctuations on blades surfaces. The reduction of the unsteady loading results in a noise emission reduction in the direction of thrust force.

- What is the change in wake flow evolution of a model with relative phase angle variation compared with a model without it?

The wake flow deformation is affected by the relative phase angle. The approach of the adjacent wake structures is less evident than in the model without a relative phase angle. In the region between the propeller, the “shear deformation” of the wake is less prominent and is turned into a “bumpy” shape. The change is related to the local deformation of the tip vortices. The distance of the nearby vortical structures is increased due to the phase angle difference. Thus, the induced velocities between the tip vortices are less dominant than those in the 0°-relative-phase-angle case, resulting in small vortex deformation. In a time-averaged sense, the slipstream velocity remains unaltered compared to the distributed-propeller case with a 0° relative phase angle due to the unaffected time-averaged performance.

- How is the noise emission affected by the phase angle?

The reduction of the unsteady loading component due to the relative phase angle results in noise emission reduction at specific emission angles. The noise reduction is evident in front of the distributed-propeller system due to the reduction of tonal components. Along the propeller axis, there is a 7.8 dB reduction at the 1st BPF compared to the baseline model. Due to the reduced unsteady loading, the tonal component augmentation is less pronounced than the 0°-relative-phase-angle case. The near-field visualisation of the pressure fluctuations reveals a change in the pressure waves pattern. The phase difference between the blades results in the reduction of constructive interference observed in the previous model. The phase angle difference between adjacent blades leads to the reduction and cancellation of the acoustic waves emitted by the adjacent propellers. Although the effect of the relative phase angle is beneficial in front of the propellers, its impact is negative at oblique

angles near the propeller plane, where there is a 1.8 dB noise increase. This is associated with the increased tonal components due to a different distribution of the tonal noise as a result of the phase angle variation between the propellers.

7.1 Recommendation

In this section, various recommendations are presented below to investigate further the behaviour of the distributed-propeller systems as well as the analysis of the numerical model.

Isolated propeller

- Trip placement: In-depth investigation of the behaviour of the “XPROP-S” propeller. The implementation of trips on the blades’ suction side is proposed to avoid potential flow separations, observed in the current study. Trip placement will alter the behaviour of the boundary layer around the blades affecting the aerodynamic behaviour as well as the aeroacoustic one. Thus, it should be examined combined with the tonal component at $1/3^{\text{rd}}$ of the BPF.

Distributed propellers

- Low-fidelity tool development: A low-fidelity tool can be implemented to describe the behaviour of distributed-propeller systems at the initial stages of the design process. Therefore, it would be of great interest to develop a low-fidelity model for the aeroacoustic signature and aerodynamic behaviour. The steady-state effects can be approximated with a vortex tube wake model, as presented in this analysis. However, the unsteady interactions need an in-depth investigation based on the Theodorsen model on unsteady aerodynamics of airfoil.
- Distributed propellers-wing configuration: An expansion of the current model would be to analyse the combined system of a wing with distributed-propeller system mounted on it. This will show the steady and unsteady interactions between the bodies and how the behaviour of the wing is affected by the unsteady interactions.
- The angle of attack effect: The effect of various non-uniform inflow conditions would give insight into systems that could have tilted propellers. Also, it could be used to analyse the dominant effect between the angle of attack and the impact of the interference between adjacent propellers, as presented in this study. An aeroacoustic study can also be performed to determine the noise emission alteration.

Bibliography

- [1] ACARE, "Flightpath 2050 Europe's Vision for Aviation," European Commission 2011, Available: https://www.acare4europe.org/sites/acare4europe.org/files/document/Flightpath2050_Final.pdf, Accessed on: 8/9/2020.
- [2] A. S. Gohardani, G. Doulgeris, and R. Singh, "Challenges of future aircraft propulsion: A review of distributed propulsion technology and its potential application for the all electric commercial aircraft," *Progress in Aerospace Sciences*, Review vol. 47, no. 5, pp. 369-391, 2011.
- [3] C. Silva, W. Johnson, K. R. Antcliff, and M. D. Patterson, "VTOL urban air mobility concept vehicles for technology development," in *2018 Aviation Technology, Integration, and Operations Conference*, Atlanta, Georgia, 2018.
- [4] H. D. Kim, A. T. Perry, and P. J. Ansell, "A Review of Distributed Electric Propulsion Concepts for Air Vehicle Technology," in *2018 AIAA/IEEE Electric Aircraft Technologies Symposium, EATS 2018*, Cincinnati, Ohio, 2018.
- [5] H. D. Kim, "Distributed propulsion vehicles," in *27th Congress of the International Council of the Aeronautical Sciences 2010, ICAS 2010*, Nice, France, 2010, vol. 1, pp. 55-65.
- [6] N. K. Borer *et al.*, "Design and performance of the NASA SCEPTOR distributed electric propulsion flight demonstrator," in *16th AIAA Aviation Technology, Integration, and Operations Conference*, Washington, D.C., 2016, pp. 1-20.
- [7] A. M. Stoll, J. B. Bevirt, P. P. Pei, and E. V. Stilson, "Conceptual design of the joby S2 electric VTOL PAV," in *AIAA AVIATION 2014 -14th AIAA Aviation Technology, Integration, and Operations Conference*, Atlanta, GA, 2014.
- [8] E. Alvarez and A. Ning, *Modeling Multirotor Aerodynamic Interactions Through the Vortex Particle Method*. 2019.
- [9] W. Zhou, Z. Ning, H. Li, and H. Hu, "An experimental investigation on rotor-to-rotor interactions of small UAV," in *35th AIAA Applied Aerodynamics Conference, 2017*, Denver, Colorado, 2017.
- [10] H. Lee and D. J. Lee, "Rotor interactional effects on aerodynamic and noise characteristics of a small multirotor unmanned aerial vehicle," *Physics of Fluids*, Article vol. 32, no. 4, 2020, Art. no. 047107.
- [11] R. de Vries, N. van Arnhem, T. Sinnige, R. Vos, and L. L. M. Veldhuis, "Aerodynamic interaction between propellers of a distributed-propulsion system in forward flight," *Aerospace Science and Technology*, Article vol. 118, 2021, Art. no. 107009.
- [12] N. Intaratep, W. Nathan Alexander, W. J. Deveport, S. M. Grace, and A. Dropkin, "Experimental study of quadcopter acoustics and performance at static thrust conditions," in *22nd AIAA/CEAS Aeroacoustics Conference, 2016*, 2016.
- [13] K. A. Pascioni and S. A. Rizzi, "Tonal noise prediction of a distributed propulsion unmanned aerial vehicle," in *2018 AIAA/CEAS Aeroacoustics Conference*, Atlanta, Georgia, 2018.
- [14] Q. R. Wald, "The aerodynamics of propellers," *Progress in Aerospace Sciences*, Review vol. 42, no. 2, pp. 85-128, 2006.
- [15] L. L. M. Veldhuis, "Propeller wing aerodynamic interference," PhD thesis, Delft University of Technology, 2005.
- [16] L. R. Miranda and J. E. Brennan, "AERODYNAMIC EFFECTS OF WINGTIP-MOUNTED PROPELLERS AND TURBINES," in *AIAA Paper*, 1986, pp. 221-228.
- [17] B. W. McCormick, *Aerodynamic, Aeronautics and Flight Mechanics*. New York: J. Wiley, 1979.
- [18] S. Yoon, H. C. Lee, and T. H. Pulliam, "Computational analysis of multi-rotor flows," in *54th AIAA Aerospace Sciences Meeting*, San Diego, California, USA, 2016.
- [19] D. Shukla and N. Komerath, "Rotor-duct aerodynamic and acoustic interactions at low Reynolds number," *Experiments in Fluids*, Article vol. 60, no. 1, 2019, Art. no. 20.

- [20] S. Glegg and W. Devenport, S. Glegg and W. Devenport, Eds. *Aeroacoustics of Low Mach Number Flows*. Academic Press, 2017.
- [21] D. G. Simmons, "Introduction to Aircraft Noise," 2018.
- [22] H. D. B. Magliozzi B., Amiet R. K., "Propeller and Propfan Noise," in "Aeroacoustics of Flight Vehicles: Theory and Practice," National Aeronautics and Space Administration 1991, vol. 1.
- [23] K. D. Marte Jack, "A Review of Aerodynamic Noise From Propellers, Rotors and Lift Fans," National Aeronautics and Space Administration 1970.
- [24] M. J. Lighthill, "On sound generated aerodynamically I. General theory," (in eng), *Proceedings of the Royal Society of London - Series A: Containing Papers of a Mathematical and Physical Character*, vol. 211, no. 1107, p. 564, 1952.
- [25] J. E. J. J. E. Ffowcs Williams, "Sound generation by turbulence and surfaces in arbitrary motion," (in eng), *Philosophical Transactions of the Royal Society of London A*, no. 1151, pp. 321-342, 1969.
- [26] F. Farassat, "Derivation of Formulations 1 and 1A of Farassat," NASA Langley Research Center Hampton, Technical Report 2007, Available: <https://ntrs.nasa.gov/citations/20070010579>, Accessed on: 17/9/2020.
- [27] K. A. Pascioni, S. A. Rizzi, and N. H. Schiller, "Noise reduction potential of phase control for distributed propulsion vehicles," in *AIAA Scitech 2019 Forum*, 2019.
- [28] T. Krüger, H. Kusumaatmaja, A. Kuzmin, O. Shardt, G. Silva, and E. M. Viggien, *The Lattice Boltzmann Method - Principles and Practice*. 2016.
- [29] D. Herrmann, "A Study of the Suitability of PowerFLOW as an Educational Engineering Design Tool for Undergraduate Students.," Institute for Aerodynamik und Gasdynamik, University of Stuttgart, University of Colorado /Center for Aerospace - Structures.
- [30] F. Avallone, W. C. P. Van Der Velden, D. Ragni, and D. Casalino, "Noise reduction mechanisms of sawtooth and combed-sawtooth trailing-edge serrations," *Journal of Fluid Mechanics*, Article vol. 848, pp. 560-591, 2018.
- [31] D. Casalino, A. Hazir, and A. Mann, "Turbofan broadband noise prediction using the lattice boltzmann method," *AIAA Journal*, Article vol. 56, no. 2, pp. 609-628, 2018.
- [32] F. Avallone *et al.*, "Aerodynamic and aeroacoustic effects of swirl recovery vanes length," *Journal of Aircraft*, Article vol. 56, no. 6, pp. 2223-2235, 2019.
- [33] S. B. Pope, *Turbulent Flows*. Cambridge: Cambridge University Press, 2000.
- [34] S. Chen and G. D. Doolen, "Lattice Boltzmann Method for Fluid Flows," *Annual Review of Fluid Mechanics*, vol. 30, pp. 329-364, 1998.
- [35] S. Hickel and S. Hulshoff, "Lecture notes: CFD 3 – Large Eddy Simulation."
- [36] V. Yakhot and S. A. Orszag, "Renormalization group analysis of turbulence. I. Basic theory," *Journal of Scientific Computing*, Article vol. 1, no. 1, pp. 3-51, 1986.
- [37] B. E. Launder and D. B. Spalding, "The numerical computation of turbulent flows," *Computer Methods in Applied Mechanics and Engineering*, Article vol. 3, no. 2, pp. 269-289, 1974.
- [38] D. Systèmes, "SIMULIA PowerFLOW User's Guide," Exa Corporation Release 6, 2019.
- [39] G. A. Brès, F. Pérot, and D. Freed, "A fflowcs williams-hawkings solver for lattice-boltzmann based computational aeroacoustics," in *16th AIAA/CEAS Aeroacoustics Conference (31st AIAA Aeroacoustics Conference)*, 2010.
- [40] D. Casalino, "An advanced time approach for acoustic analogy predictions," *Journal of Sound and Vibration*, Article vol. 261, no. 4, pp. 583-612, 2003.
- [41] P. R. Spalart, K. V. Belyaev, M. L. Shur, M. Kh Strelets, and A. K. Travin, "On the differences in noise predictions based on solid and permeable surface Ffowcs Williams–Hawkings integral solutions," *International Journal of Aeroacoustics*, Article vol. 18, no. 6-7, pp. 621-646, 2019.
- [42] A. P. Pandey, "Investigation of propeller characteristics at low Reynolds number with an angle of attack: A computational aeroacoustic study," Master Thesis, Aerospace Engineering, Delft University of Technology, 2021.
- [43] J. Winslow, H. Otsuka, B. Govindarajan, and I. Chopra, "Basic understanding of airfoil characteristics at low Reynolds numbers (104–105)," *Journal of Aircraft*, Article vol. 55, no. 3, pp. 1050-1061, 2018.

- [44] C. A. Lyon, M. S. Selig, and A. P. Broeren, "Boundary layer trips on airfoils at low reynolds numbers," in *35th Aerospace Sciences Meeting and Exhibit*, 1997.
- [45] S. Glegg and W. Devenport, "Chapter 4 - Lighthill's acoustic analogy," in *Aeroacoustics of Low Mach Number Flows*, S. Glegg and W. Devenport, Eds.: Academic Press, 2017, pp. 73-93.
- [46] J. Jeong and F. Hussain, "On the identification of a vortex," *Journal of Fluid Mechanics*, Article vol. 285, pp. 69-94, 1995.
- [47] S. O. Afari and R. R. Mankbadi, "Simulations of noise generated by rotor-rotor interactions at static conditions," in *AIAA Scitech 2021 Forum*, 2021, pp. 1-15.